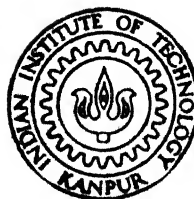


**MÖSSBAUER SPECTROSCOPIC STUDIES OF SOME GLASSES,
COBALTATES AND SUPER SENDUST ALLOY**

by

UMESH CHANDRA JOHRI

PHY
1988
D
JOH
MOS



DEPARTMENT OF PHYSICS

INDIAN INSTITUTE OF TECHNOLOGY, KANPUR

AUGUST, 1988

MÖSSBAUER SPECTROSCOPIC STUDIES OF SOME GLASSES, COBALTATES AND SUPER SENDUST ALLOY

**A Thesis Submitted
In Partial Fulfilment of the Requirements
for the Degree of**

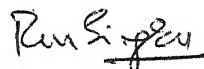
DOCTOR OF PHILOSOPHY

by
UMESH CHANDRA JOHRI

to the
**DEPARTMENT OF PHYSICS
INDIAN INSTITUTE OF TECHNOLOGY, KANPUR
AUGUST, 1988**

CERTIFICATE

This is to certify that the work presented in this thesis entitled 'Mössbauer Spectroscopic Studies of Some Glasses, Cobaltates and Super Sendust Alloy' by Umesh Chandra Johri has been done under my supervision and it has not been submitted elsewhere for a degree or diploma.



R. M. Singru
Department of Physics
Indian Institute of Technology
Kanpur, India.

August 1988.

TH
543.08586
J663m

- 3 JUL 1989

95171-1

106279

PHY - 1988 - D - JOH - MOS

ACKNOWLEDGEMENTS

I express my deep sense of gratitude towards Professor R.M Singru for his help and guidance throughout the course of my Ph.D. work. His continued encouragement has enabled me to complete this work.

I am thankful to Dr. D. Bahadur and Dr. S. Ram for providing me samples and communicating their results on related work and for useful discussion. I am also thankful to Prof. K.N. Rai and Mr. G.C. Uniyal for providing samples of Super Sendust alloy and for discussion.

I thank Prof. D.C. Khan and Prof. T.R. Ramachandran for taking interest in the progress of my work and giving me suggestions from time to time.

I take this opportunity to express my sincere thanks to Dr. V.N. Kulkarni for his help and suggestions in carrying out the experiments. Thanks are also due to Mr. Vishal Saxena on this count.

It is a pleasure to thank the staff of the Central Nuclear Laboratory Sarva Shree K.M.L. Jha, K. Masood, M.M. Gupta, A.R. Korde, B.K. Sharma, R.S. Rajput and Shiv Prakash.

The acknowledgements could not be complete without mentioning the names of Mr. R.R. Mishra, Dr. V. Kumar, Dr. H.K. Patel, Dr. G.S. Raghu-vanshi, Dr. A.K. Nayak, Dr. S.J. Mali, Mr. S. Chaudhary, Mr. Naveen Suyal, who have always come forward to help me in times of need. My special thanks are due to Mr. C.B. Srivastava for his timely help and Mr. Nobin Banerji for his considerable help in the final preparation of this thesis.

Finally I thank Mr. B.K. Jain for the fine tracing of the diagrams Mr. L.S. Bajpai for the neat typing, Mr. H.K. Panda and Mr. Lallu Singh for the good cyclostyling.

UMESH CHANDRA JOHRI

CONTENTSPage

LIST OF TABLES

LIST OF FIGURES

SYNOPSIS

CHAPTER 1 :	<u>INTRODUCTION</u>	1
1.1	INTRODUCTION	1
1.2	HYPERFINE INTERACTIONS	9
1.2.1	Electric Monopole Interaction	12
1.2.2	Electric Quadrupole Interaction (EQI)	21
1.2.3	Magnetic Dipole Interaction	26
1.2.4	Mixed Magnetic Dipole and Electric Quadrupole Interaction	30
1.3	SUPERPARAMAGNETISM	32
	<u>REFERENCES</u>	34
CHAPTER 2 :	<u>EXPERIMENTAL METHODS</u>	36
2.1	INTRODUCTION	36
2.2	MÖSSBAUER SPECTROMETER	36
2.2.1	Gamma-ray Photon Source	37
2.2.2	Mössbauer Drive	39
2.2.3	Absorbers	42
2.2.4	Gamma-ray Photon Detection System	43
2.2.5	Data Acquisition, Storage and Handling System	44
2.2.6	Cryostat and Furnace	45

2.3	EXPERIMENTAL PROCEDURE	48
2.4	OPTIMIZATION OF THE ABSORBER THICKNESS	51
2.5	GEOMETRICAL EFFECTS	54
2.5.1	Source-Detector Distance Variation Effect	54
2.5.2	Cosine Effect	55
2.6	DATA ANALYSIS	56
2.6.1	Hyperfine Field Distribution	57
	<u>REFERENCES</u>	62
CHAPTER 3 :	MÖSSBAUER AND OTHER STUDIES OF SOME GLASS-CERAMIC SYSTEMS CONTAINING MAGNETIC PHASES	64
3.1	INTRODUCTION	64
3.2	STUDY OF YTTRIUM IRON GARNET (YIG) SYSTEMS	69
3.2.1	Introduction	69
3.2.2	Experimental Method	70
3.2.2.1	Sample preparation	70
3.2.2.2	Mössbauer spectroscopic studies	73
3.2.2.3	Measurement of X-ray, EPR and optical spectra and magnetization curves	73
3.2.3	Results and Discussion	
3.3	STUDY OF THE PRECIPITATION OF HEXA- GONAL FERRITES ($\text{BaFe}_{12}\text{O}_{19}$, $\text{SrFe}_{12}\text{O}_{19}$, $\text{PbFe}_{12}\text{O}_{19}$) IN BORATE GLASSES	103

	<u>Page</u>
3.3.1 Introduction	103
3.3.2 Experimental	106
3.3.3 Results and Discussion	108
3.4 SUMMARY AND CONCLUSION	127
<u>REFERENCES</u>	134
CHAPTER 4 <u>MÖSSBAUER AND OTHER STUDIES OF</u>	
<u>$\text{LaCo}_{1-x}\text{Zr}_x\text{O}_3$</u>	139
4.1 INTRODUCTION	139
4.2 EXPERIMENTAL	146
4.2.1 Preparation of Cobaltate	146
4.2.2 Measurement of X-ray and Magnetic Susceptibility	147
4.2.3 Mössbauer Spectroscopic Measurements	147
4.3 RESULTS AND DISCUSSION	149
4.4 SUMMARY AND CONCLUSION	170
<u>REFERENCES</u>	172
CHAPTER 5 <u>MÖSSBAUER SPECTROSCOPIC STUDIES OF</u>	
<u>OF THE SUPER SENDUST ALLOY</u>	174
5.1 INTRODUCTION	174
5.2 EXPERIMENTAL METHOD	178
5.2.1 Sample Preparation	178
5.2.2 Mössbauer Spectroscopic Studies	180

	<u>Page</u>
5.2.3 Measurement of X-ray Diffraction Spectra	180
5.3 RESULTS AND DISCUSSION	181
5.4 SUMMARY AND CONCLUSION	202
<u>REFERENCES</u>	204

LIST OF TABLES

<u>Number</u>	<u>Caption</u>	<u>Page</u>
1.1	Relationship between variables measured using Mössbauer spectroscopy and various research fields.	2
1.2	A typical example of atomic and nuclear transitions.	7
1.3	Parameters for the 14.4 keV Mössbauer transition in ^{57}Fe .	10
1.4	Approximate ranges of isomer shift observed at room temperature (293 K) w.r.t. 310SS.	18
3.1	Composition of the glasses investigated with different nucleating agents.	71
3.2	Sample labels and details of the heat treatment given to different glass compositions (heat-treatment is described in terms of temperature/period) with X-rays and magnetization data.	72
3.3	Mössbauer parameters (measured at room temperature 293 K) for samples C10, C11, C12, C20, C21, C22, C30, C31, C32, C33, C40, C41.	78

<u>Number</u>	<u>Caption</u>	<u>Page</u>
3.4	Different parameters related to the P(V) distribution obtained for the four sample C30, C31, C32 and C33.	83
3.5	Different parameters related to the P(V) distribution obtained for the sample C11, C12.	83
3.6	Parameters obtained from Mössbauer spectra for samples C11, C21 and C33 at 80 K.	95
3.7	Absorption bands of Fe^{3+} corresponding to the different sites in YIG observed for sample C33.	102
3.8	Sample labels and details of heat-treatment given to different glass compositions (heat-treatment is described in terms of temperature/period) with X-rays and magnetization data.	107
3.9	Different Mössbauer parameters of sample S20 at 293 K.	109
3.10	Mössbauer parameters of samples B11, B12, B13, B14, B15 and B16 at 293 K.	114
3.11	Mössbauer parameters of samples S11, S12 and S21 at 293 K.	120
3.12	Mössbauer parameters of samples P11 and P12 at 293 K and 80 K.	124

<u>Number</u>	<u>Caption</u>	<u>Page</u>
4.1	Lattice parameters (measured at 293 K) for $\text{LaCo}_{1-x}\text{Zr}_x\text{O}_3$.	148
4.2	Mössbauer parameters (measured at 80 K) for $\text{LaCo}_{1-x}\text{Zr}_x\text{O}_3$.	157
4.3	Mössbauer parameters (measured at 293 K) for $\text{LaCo}_{1-x}\text{Zr}_x\text{O}_3$.	161
4.4	Mössbauer parameters (measured at 500 K) for $\text{LaCo}_{1-x}\text{Zr}_x\text{O}_3$.	163
4.5	Mössbauer parameters (measured at 700 K) for $\text{LaCo}_{1-x}\text{Zr}_x\text{O}_3$.	166
4.6	The ratio y giving the relative population of Co^{3+} with respect to the other state of Co in $\text{LaCo}_{1-x}\text{Zr}_x\text{O}_3$.	168
5.1	Mössbauer parameters (measured at 293 K) for sample SD1, SD2, SD3.	189
5.2	Magnetic field (H_{int}) observed for different Fe sites in Fe-Al alloys found in literature and configuration obtained in the present Fe-Si (Ni, Al) alloy.	190
5.3	Mössbauer parameters (measured at 80 K) for sample SD1, SD2 and SD3.	194
5.4	Mössbauer parameters (measured in the temperature range 380-926 K) for sample SD1.	196

<u>Number</u>	<u>Caption</u>	<u>Page</u>
5.5	Various parameters related to the $P(H)$ distribution obtained for SD1 in the temperature range 80-900 K.	201

LIST OF FIGURES

<u>Number</u>	<u>Caption</u>	<u>Page</u>
1.1 (a)	Intensity $I(E)$ of spectral line as a function of transmission energy E_0 .	4
(b)	Atom at rest when emitting a photon receiving recoil energy E_R .	4
(c)	The schematic energy level diagram of free atom or nucleus. The source photon may excite absorber atom if $E_R \ll \Gamma$.	4
1.2	Overlap of the emission and absorption lines showing the relation between E_0 , E_r^s , E_r^a and for two cases : (a) optical case $E_R \ll \Gamma$ and (b) nuclear case $E_R \gg \Gamma$.	6
1.3 (a)	Effect of monopole interaction on the energy levels of source and absorber.	14
(b)	Mössbauer spectrum showing monopole interaction.	14
1.4	Data for the ^{57}Fe isomer shift with respect to natural iron ($\alpha\text{-Fe}$) at room temperature. Units of the IS values are in mm s^{-1} and the signs of the velocity for the source are to be read from the bottom row while the signs of the velocity for the absorber are to be read from the top row.	16

<u>Number</u>	<u>Caption</u>	<u>Page</u>
1.5	Review of ^{57}Fe isomer shift data of iron in various ionization states [8].	17
1.6	Review of ^{57}Fe Mössbauer parameters (a) IS (isomer shift) and (b) DE (quadrupole splitting) for iron plotted against the coordination number for ''ionic'' high spin and low spin compounds and minerals. Arrows indicate that the values outside the range of boxes have been observed.	19
1.7	Effect of quadrupole interaction on the nuclear energy levels of source/absorber and the resulting Mössbauer spectrum showing the quadrupole splitting and isomer shift.	25
1.8	Effect of magnetic hyperfine interaction on energy levels of ^{57}Fe . Peak positions of the six-finger pattern are shown at the bottom (c = centroid).	29
1.9	Effect of weak quadrupole interaction and a strong magnetic interaction on the energy levels of ^{57}Fe . The numbers 1 to 6 refer to those in Fig. 1.8.	
2.1	Schematic block diagram of Mössbauer spectrometer.	38

<u>Number</u>	<u>Caption</u>	<u>Page</u>
2.2	Electromechanical transducer.	41
2.3	Schematic block diagram of the electro-mechanical transducer used in the Mössbauer spectrometer.	41
2.4	Design of the cryostat used in the Mössbauer experiments carried out in temperature range 80-300 K.	46
2.5	Design of the furnace with resistance heating assembly.	46
2.6	Decay scheme of ^{57}Co .	49
2.7	Pulse height spectrum of ^{57}Co in Rh matrix (Mössbauer source) measured using proportional counter.	49
2.8	Hyperfine field distribution for $\alpha\text{-Fe}$ (absorber) at room temperature. The top Fig. shows the $P(H)$ distribution while the bottom Fig. shows the corresponding Mössbauer spectrum of $\alpha\text{-Fe}$.	60
2.9	EFG distribution in sodium nitroprusside (absorber) at room temperature. The top Fig. shows the $(P V)$ distribution while the bottom Fig. shows the fitted Mössbauer spectrum.	61

<u>Number</u>	<u>Caption</u>	<u>Page</u>
3.1 (a)	Mössbauer spectra of C10, C11, C12 at 293K.	75
(b)	Mössbauer spectra of C21, C22, C41 at 293K.	76
(c)	Mössbauer spectra of C30, C31, C32, C33 at 293 K.	77
3.2	Distribution of the electric field gradient, P(V), at ^{57}Fe nuclei in C30, C31, C32 and C33.	82
3.3	Distribution of the electric field gradient, P(V), at ^{57}Fe nuclei in C11 and C12.	85
3.4	Mössbauer spectra of C11, C12 and C33 at 80 K.	97
3.5	EPR spectra of C10, C21, C11, C12 and C33.	100
3.6	The electronic absorption spectra of C10, C22 and C33. Bands marked by arrows refer Fe^{2+} absorption * refer vibronic bands. Absorption scale is given for sample C33.	100
3.7 (a)	Mössbauer spectrum of S20 at 293 K.	110
(b)	S20 spectrum resolved in two doublet.	110
(c)	Distribution of the electric field gradient, P(V), at ^{57}Fe nuclei in S20.	110
3.8 (a)	Mössbauer spectra of B11, B12 and B13 at 293 K.	112
(b)	Mössbauer spectra of B14, B15 and B16 at 293 K.	113
3.9	Mössbauer spectra of S11, S12, S21 at 293 K.	
3.10	Mössbauer spectra of P11, P12 at 80 and 293 K.	125

<u>Number</u>	<u>Caption</u>	<u>Page</u>
4.1 (a)	Inverse magnetic susceptibility per gram against temperature for $\text{LaCo}_{1-x}\text{Zr}_x\text{O}_3$.	151
4.1 (b)	Plot of $\chi_g T$ against temperature for $\text{LaCo}_{1-x}\text{Zr}_x\text{O}_3$.	151
4.2	Spin states of cobalt and consequent iron.	155
4.3	Mössbauer spectra of $\text{LaCo}_{1-x}\text{Zr}_x\text{O}_3$ at 80 K.	156
4.4	Mössbauer spectra of $\text{LaCo}_{1-x}\text{Zr}_x\text{O}_3$ at 293 K.	159
4.5	Mössbauer spectra of $\text{LaCo}_{1-x}\text{Zr}_x\text{O}_3$ at 500 K.	162
4.6	Mössbauer spectra of $\text{LaCo}_{1-x}\text{Zr}_x\text{O}_3$ at 700 K.	165
4.7	Variation of y as a function of temperature.	167
5.1	Mössbauer spectra of SD1, SD2 and SD3 at 80 K.	182
5.2	Mössbauer spectra of SD1, SD2 and SD3 at 293 K.	183
5.3	Mössbauer spectra of SD1 in the temperature range 380-800 K.	184
5.4	Mössbauer spectra of SD1 in the temperature range 900-926 K.	185
5.5	X-ray diffraction spectrum of SD1 at 293 K.	187

<u>Number</u>	<u>Caption</u>	<u>Page</u>
5.6	Unit cell of the ordered Fe_3Si or Fe_3Al structure.	187
5.7	Magnetic field (H_{int}) at ^{57}Fe as a function of temperature for sites I, II, III and IV.	197
5.8	The IS as a function of temperature for sites I, II and III.	197
5.9	Hyperfine field (H_{int}) distribution for SD1 in the temperature range 80-900 K.	200

SYNOPSISMÖSSBAUER SPECTROSCOPIC STUDIES OF SOME GLASSES, COBALTATES
AND SUPER SENDUST ALLOY

UMESH CHANDRA JOHRI
Department of Physics
Indian Institute of Technology, Kanpur, India.

August, 1988

Mössbauer effect is the name given to the phenomenon of recoilless absorption or emission of nuclear gamma-rays and it has proved to be a valuable method for studying the interactions of atomic nucleus with its surrounding atoms. During the last two decades, Mössbauer spectroscopy is being used as a sensitive technique to study structural, electric and magnetic properties of different materials having interesting technological interest. In particular Mössbauer spectroscopic studies of glass systems, ferrites, cobaltates and other materials have supplemented our knowledge about these materials. The hyperfine interaction in these materials gives rise to Mössbauer parameters like isomer shift, quadrupole splitting and magnetic hyperfine field which can be determined from the measured Mössbauer spectra. A systematic analysis of these Mössbauer parameters gives valuable information, which when combined with the data obtained from other

characterization studies, lead us to a better understanding of the electronic structure of these systems. Although Mössbauer spectroscopy can be carried out with different 'Mössbauer' nuclei, measurements using ^{57}Co --- ^{57}Fe decay has been found most convenient. In the present thesis we have described our ^{57}Fe Mössbauer spectroscopic studies of glass ceramic systems containing magnetic phases (viz. yttrium-iron-garnet systems, hexagonal ferrites in borate glasses), substituted perovskite systems $\text{LaCo}_{1-x}\text{Zr}_x\text{O}_3$ (with $x = 0.1, 0.3$ and 0.5) and high permeability material Super Sendust - a Fe-Si-Al-Ni alloy system. Whereever possible the results of Mössbauer spectroscopic studies are combined with other results of other techniques like X-ray diffraction, EPR, optical absorption spectra, magnetization studies etc. to obtain a clearer picture of the properties of materials studied.

The present thesis is divided into five Chapters. The first Chapter provides an introduction to the phenomenon of Mössbauer effect. The origin of hyperfine interaction is discussed to bring out the role of electric monopole interaction, electric quadrupole interaction and magnetic dipole interaction in Mössbauer spectroscopy. This is followed by a discussion of how the Mössbauer parameters like isomer shift, electric quadrupole splitting and magnetic hyperfine field are related to

these interactions. The phenomenon of super-paramagnetism is also discussed briefly.

The experimental methods used in the present work are described in the second Chapter. Different parts of the Mössbauer spectrometer used by us are described in detail. The details of data acquisition, storage and data handling systems are explained and the cryostat and furnace used in the measurements are also described. Other aspects of the methodology used like the optimization of the absorber thickness and the consideration of geometrical effects are discussed. The method used by us in deriving the hyperfine field distribution from the measured Mössbauer spectra is also explained. The procedure followed by us to prepare any particular sample is described separately for each specimen in the following chapter at an appropriate place.

In Chapter 3 we have presented the results of our Mössbauer and other studies of some glass-ceramic systems containing magnetic phases. The silica-based substituted yttrium-iron-garnet (YIG) system in which external nucleating agents (viz. Bi_2O_3 , $\text{Ag}_2\text{O}_3 + \text{As}_2\text{O}_3$ and Pd) were added in the base glass and magnetic phases were precipitated during a controlled heat treatment. These specimens have been studied with Mössbauer spectroscopy. Results obtained by the measurements involving X-rays, EPR, optical spectra and magnetization curves are also used to interpret the data. Mössbauer parameters of the

as-prepared and the heat treated samples were obtained and analyzed to examine the effects of different composition, nucleating agents and heat treatments. It is observed that each of these factors affects the process of precipitation of the magnetic phase with accompanying changes which can be measured by Mössbauer spectroscopy. The behaviour of isomer shift, electric quadrupole splitting and magnetic hyperfine field is examined closely for all the samples studied by us to understand the effects of atomic structure and hyperfine interaction in these materials. Thus, for example, our results give us some idea about the site where Si^{4+} ions get substituted in the garnet lattice. Our studies have also indicated which heat treatment is more helpful for the precipitation of the YIG phase. Auxiliary measurements made by using the EPR and optical spectroscopy have helped to understand other aspects of the process of precipitation in these systems.

Second category of glass systems studied by us included borate glass systems in which hexagonal ferrites (BaM , SrM and PbM) were precipitated. These involved the systems $35\text{BaO}-40\text{B}_2\text{O}_3-25\text{Fe}_2\text{O}_3$, $35\text{SrO}-40\text{B}_2\text{O}_3-25\text{Fe}_2\text{O}_3$, $47\text{SrO}-28\text{B}_2\text{O}_3-25\text{Fe}_2\text{O}_3$, and $50\text{PbO}-30\text{B}_2\text{O}_3-20\text{Fe}_2\text{O}_3$. The heat treatment schedule involving temperature and period of the nucleation and crystallization for these samples was varied and Mössbauer spectra of such heat-treated samples were recorded. The magnetic phase, after precipitation

gave rise to Mössbauer spectra due to different sublattices. For each sample a comparison of spectra from differently heat-treated samples was made to determine the optimum composition and heat-treatment required for good growth of the magnetic phases of BaM, SrM and PbM. It was thus found that in $35\text{BaO}-40\text{B}_2\text{O}_3-25\text{Fe}_2\text{O}_3$ systems the choice of nucleation temperature $850\text{K}/2\text{h}$ and crystallization temperature $1065\text{K}/2\text{h}$ is optimum for the precipitation of BaM. In the case of the composition $35\text{SrO}-40\text{B}_2\text{O}_3-25\text{Fe}_2\text{O}_3$ the nucleation temperature 885 K (for 5 h) and crystallization temperature 1035 K (for 10 h) was found to be most appropriate for a clear-cut growth of SrM phase. A change of the composition to $47\text{SrO}-28\text{B}_2\text{O}_3-25\text{Fe}_2\text{O}_3$ did not show any improvement. The two heat-treatments given by us to the system $50\text{PbO}-30\text{B}_2\text{O}_3-20\text{Fe}_2\text{O}_3$ did not result in any substantial growth of the crystalline PbM phase.

Chapter 4 describes our Mössbauer spectroscopic studies of the substituted perovskite system $\text{LaCo}_{1-x}\text{Zr}_x\text{O}_3$ with $x = 0.1, 0.3$ and 0.5 . These studies have helped to understand the spin- and valence state equilibria in these compounds. Mössbauer spectroscopic studies were supplemented by X-ray diffraction and magnetic susceptibility measurements. Novel feature of the Mössbauer studies of these samples was the deposition of radioactive ^{57}Co into the samples so that $\text{La}^{57}\text{Co}_{1-x}\text{Zr}_x\text{O}_3$ was used as a Mössbauer source. Using 310 stainless steel and ^{57}Fe enriched potassium ferrocyanide as

absorbers, Mössbauer spectra were recorded at 80, 295, 500 and 700 K while magnetic susceptibility was measured in the temperature range 300-800 K. The system with $x = 0.1$ was observed to show results different from those for $x = 0.3$ and 0.5 and this behaviour could be due to the effects of the substitution of Zr ions. The Mössbauer data have enabled us to identify various spin states for different x at each temperature. Similarly the area under various lines in the Mössbauer spectra has helped us to estimate the relative population of the Co^{3+} state with respect to other states of cobalt. The temperature variation of this population for different x -values and temperatures shows a general agreement with the results observed in the magnetic susceptibility measurements. Some suggestions are made about the likely mechanisms involved in the changes between different spin states of cobalt in the $\text{LaCo}_{1-x}\text{Zr}_x\text{O}_3$ system.

In the last Chapter the Mössbauer spectroscopic and X-ray diffraction studies of the so-called 'Super Sendust' alloy of the Fe-Si-Al-Ni system are described. Super Sendust is a new high permeability magnetic alloy having several interesting technical applications. The alloy studied by us had the composition 2.96 wt % Ni, 5.0 wt% Si, 3.87 wt% Al and 88.17 wt% Fe. Mössbauer spectra of these samples were measured at 80, 293, 380, 486, 600, 700, 800, 900, 913, 918 and 926 K. Around

918-926 K the spectrum reduced to a single line indicating that the magnetic ordering temperature for this sample is $T_c = 926 \pm 1$ K. Below this temperature ($T < T_c$) the Mössbauer spectra could be analyzed into 4 sextets for which the Mössbauer parameters, hyperfine field distributions $P(H)$ and average value of H_{int} at the ^{57}Fe nucleus were determined.

It is hoped that the measurements carried out in these glass ceramics, $\text{LaCo}_{1-x}\text{Zr}_x\text{O}_3$ compounds and Super Sendust alloy have helped to extend our present understanding of these systems.

CHAPTER 1

INTRODUCTION

1.1 INTRODUCTION

In 1958 Rudolf Mössbauer [1] reported that nuclei bound in solids may emit or absorb gamma-ray photons without any recoil energy transferred to lattice vibrations. This phenomenon of recoilless emission and absorption of nuclear gamma rays is known as Mössbauer effect (ME). Soon after this discovery it was realized that ME provides a simple but precise technique for measuring relative changes in nuclear energy levels which are typically of the order of 1 part in 10^{13} when ^{57}Fe are used as Mössbauer atoms (nuclei). Here the term "Mössbauer atom" refers to the atom whose nucleus is involved in emission or absorption of gamma ray photons. This high resolution (10^{-13}) allows the observation of the hyperfine interactions of the nucleus with its surroundings which, in turn, provides information about the electronic structure of the relevant atom and its environment. These features have rendered Mössbauer spectroscopy (MS) as an attractive and powerful tool in studying different kinds of problems in diverse disciplines like solid state physics, chemistry, metallurgy, biology, geology, theory of relativity etc. The parameters measured from MS and the relevant information obtained from them are outlined in Table 1.1.

TABLE 1.1

Relationship between variables measured using Mössbauer spectroscopy and various research fields.

Measured Variables	Nuclear Physics	Solid State Physics	Chemistry	Metallurgy	Biology	Analytical
Isomer shift	Nuclear radius	Electronic structure	Valence state and covalency	Electronic structure	Valence change	-
Magnetic hyperfine structure		Magnetic structure, Electronic configuration of magnetic ions	Electronic configuration of magnetic ions			Chemical or phase identification by comparison with spectra of known materials
	Nuclear moment			Order disorder precipitate identification	Ligand conformation	
Electric quadrupole hyperfine structure		Electronic configuration	Ligand symmetry, bonding orbitals			Particle size information via superparamagnetism
Recoil free fraction		Phonon spectrum, anisotropic binding	Anisotropic binding	Force constants and anharmonic	Free or bound complex	-

In the present chapter we shall describe briefly the basic principles of MS and hyperfine interactions (HI). A detailed discussion of these topics will be found in several excellent reviews and books [2-8].

In 1905 Wood discovered that when sodium vapour is irradiated with sodium light it starts glowing. This phenomenon known as atomic resonance fluorescence occurs when photons in the incident sodium light have the precise energy required to raise the atom in the sodium vapour to their excited state as shown in Fig. 1.1. The excited atoms deexcite via reemission of photons which cause the glowing of the vapour. In 1929 Kuhn performed a similar experiment in which he irradiated a piece of lead with gamma ray photons from a thorium-C source. The aim of this experiment was to excite the lead nuclei so that nuclear resonance fluorescence could be observed. The fact that Kuhn did not observe any such effect was attributed to the recoil-energy loss, E_R , which is given by

$$E_R = E_{Ph}^2 / 2Mc^2 \quad (1.1)$$

and which denotes the energy transferred to a free atom of mass M when a photon of energy E_{Ph} is either emitted or absorbed. As a result of this process of recoil, the actual energy of the emitted photon is changed from the transition energy E_0 to a value $E_{Ph} = E_0 - E_R$. Thus E_{Ph}

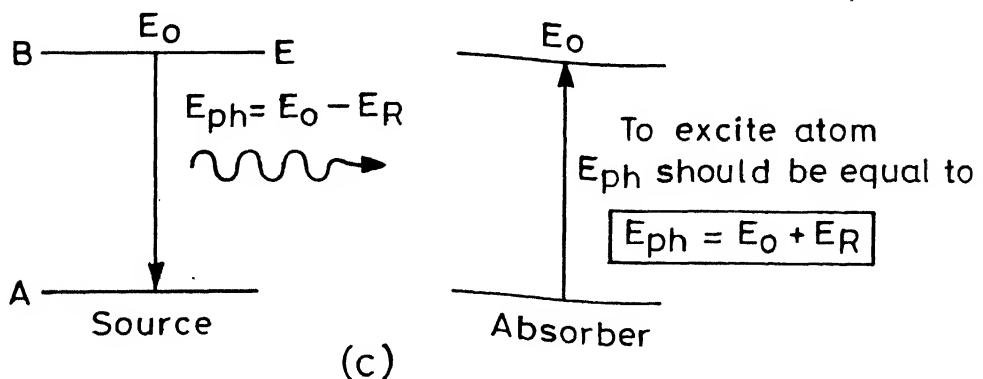
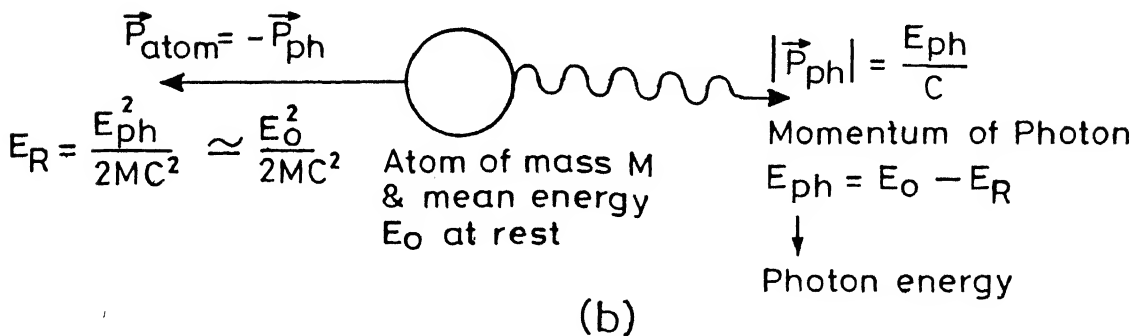
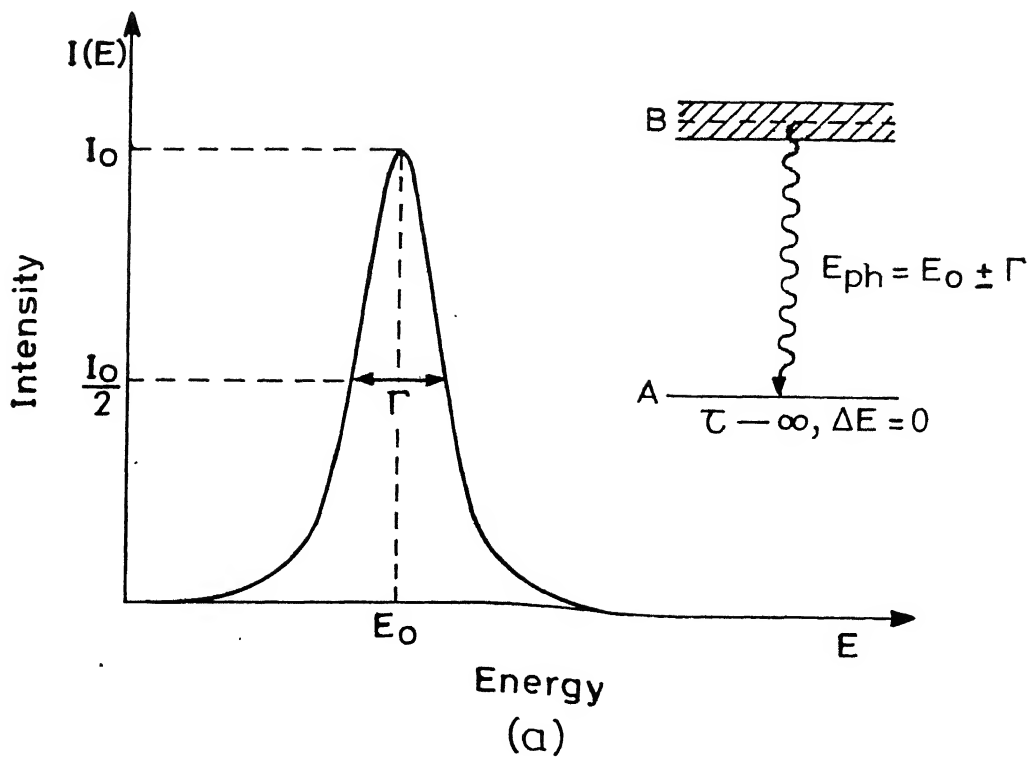


Fig.1.1(a) Intensity $I(E)$ of spectral line as a function of transition energy E_0

(b) Atom at rest when emitting a photon receiving recoil energy E_R

(c) The schematic energy level diagram of free atom or nucleus. The source photon may excite absorber atom if $E_R \ll \Gamma$

is less than the energy ($E_0 + E_R$) which is required to excite an atom in the absorber.

In case of atomic transitions involving electrons $E_R \ll \Gamma$ where Γ is the natural linewidth (which is a measure of the uncertainty in transition energy). One can, therefore, write $E_{Ph} \approx E_0$ for atomic transitions and can observe atomic resonance fluorescence in gases easily. In the case of nuclear transitions, however, $E_R \gg \Gamma$ and one can write $E_{Ph} < E_0$ and it is not possible to observe nuclear resonance fluorescence. These facts are illustrated in Fig. 1.2 and Table 1.2.

Mössbauer found out that when the recoil energy E_R is large compared to the binding energy of the atom in a solid, the atom will be displaced from its lattice site and the free-atom analysis given above will be correct. On the other hand, if the free atom recoil energy E_R is smaller than the atomic binding energy, the atom will remain at its site. In such a case the crystal as a whole receives the recoil momentum. The recoil energy will then be dissipated by exciting lattice vibrations (i.e. creation of phonons). However, a situation is possible when no phonon is created when the momentum $\hbar k$ of the gamma-ray photon is smaller than the uncertainty (Δp) in the momentum, $\Delta p \approx \hbar / \Delta x$, of the atom along the direction of gamma ray propagation. Here Δx is the uncertainty in the position of the atom along the gamma

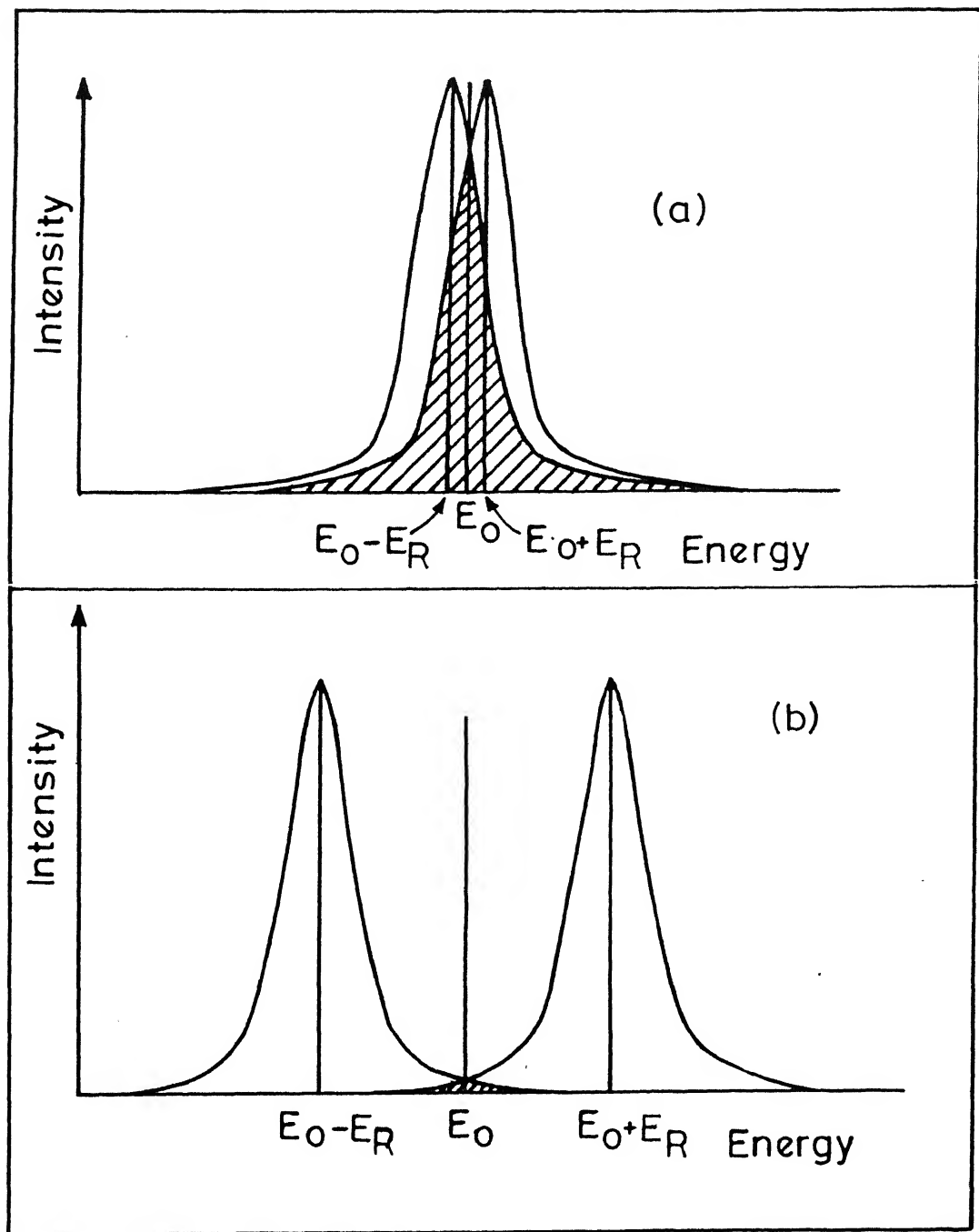


Fig. 1.2 Overlap of the emission and absorption lines showing the relation between E_0 , E_γ^s , E_γ^a and for two cases: (a) optical case $E_R \ll \Gamma$ and (b) nuclear case $E_R \gg \Gamma$.

TABLE 1.2

A typical example of atomic and nuclear transitions

Physical quantity	Symbol	Na D lines	⁵⁷ Fe, 14.4 keV -transition	Units
Transition energy	E_0	2	14.41×10^3	eV
Mean life	τ	1.6×10^{-8}	1.4×10^{-7}	s
Recoil energy	E_R	1.0×10^{-10}	1.9×10^{-3}	eV
Natural line width	Γ	3.9×10^{-8}	4.7×10^{-9}	eV
Conclusion		$E_R < \Gamma$	$E_R \gg \Gamma$	

ray propagation direction. Thus the probability for a "zero-phonon" process is expected to be appreciable when $\hbar k < \Delta p$ [9].

A more detailed analysis [3-8] shows that the probability for the lattice remaining in the same vibrational state (i.e. zero-phonon process) after the emission of the gamma ray photon at temperature T is given by $f(T)$

$$f(T) = \exp(-k^2 \langle x^2 \rangle_T) \quad (1.2)$$

where $\langle x^2 \rangle_T$ is the expectation value of the squared vibrational amplitude in the direction of propagation of the gamma-ray photon at a temperature T . The Debye model for solid leads to the following expression for the recoilless fraction $f(T)$

$$f(T) = \exp\left[-\frac{6E_R}{k_B \Theta_D} \left\{ \frac{1}{4} + \left(\frac{T}{\Theta_D}\right)^2 \int_0^{\Theta_D/T} \frac{x}{e^x - 1} dx \right\} \right] \quad (1.3)$$

where k_B is the Boltzman constant and $\Theta_D = \hbar \omega_0 / k_B$ is the Debye temperature. Above eq. (1.3) reduces to the following approximate expressions

$$f = \exp\left[-\frac{E_R}{k_B \Theta_D} \left(\frac{3}{2} + \frac{\pi^2 T^2}{\Theta_D^2}\right)\right] \quad \text{for } T \ll \Theta_D \quad (1.4a)$$

$$= \exp\left[-\frac{6E_R T}{k_B \Theta_D^2}\right] \quad \text{for } T \gg \Theta_D \quad (1.4b)$$

Following conclusions about the recoilless fraction f can be drawn from the above formula

- (i) f increases with decreasing recoil energy E_R (i.e. decreasing transition energy E_0),
- (ii) f increases with decreasing temperature,
- (iii) f increases with increasing Debye temperature Θ_D .

One may consider Θ_D to be a measure of the strength of the bonds between the Mössbauer atom and the lattice. The factor $f(T)$ is generally called the Debye-Waller factor or Lamb-Mössbauer factor.

In the spirit of above discussion it is obvious that the main requirements of suitable Mössbauer nuclide are low transition energy E_0 (generally in the range 10-150 keV) and high Debye temperature Θ_D . Taking into account other experimental difficulties, ^{57}Fe has been found to be the most suitable nuclide. To date, about 75% of the Mössbauer spectroscopic studies have been carried out using ^{57}Fe Mössbauer nuclides alone, while the Mössbauer effect has been observed for 100 nuclear transitions in about 80 nuclides distributed over 43 elements in the periodic table. In the present study we have used ^{57}Fe as Mössbauer nuclide. The important parameters of ^{57}Fe which make it the most suitable and popular Mössbauer nuclide are listed in Table 1.3 [5,10].

1.2 HYPERFINE INTERACTIONS

The hyperfine interactions (HI) are the result of interaction between nuclear moments and electromagnetic

TABLE 1.3

Parameters for the 14.4 keV Mössbauer transition in ^{57}Fe

- 1) Isotopic abundance = 2.14 %
- 2) Energy $E = 14.41303$ (8) keV
- 3) Half-life, $t_{1/2} = 97.81$ (14) ns
- 4) Ratio of the excited and ground state nuclear magnetic moment, $R_\mu = -1.7145$ (5)
- 5) Nuclear magnetic dipole moment of the excited state = $\mu = -0.15534$ (5) nm
- 6) Nuclear electric quadrupole moment of the excited state = $Q = +0.209$ (15) barns
- 7) Total internal conversion coefficient, $\alpha_T = 8.21$ (12)
- 8) Debye temperature, $\Theta_D = 440$ K
- 9) Mössbauer cross section = 256 (3) $\times 10^{-20} \text{ cm}^{-2}$
- 10) Mössbauer linewidth (theoretical full width at half maximum) $\Gamma = 0.1940 \text{ mm sec}^{-1}$
- 11) Recoil energy, $E_R = 1.957 \times 10^{-3} \text{ eV}$
- 12) Conversion factor $1 \text{ mm sec}^{-1} = 11.6248$ (1) MHz.

field at the nucleus which is produced by the surrounding electrons and ligands when a nucleus is bound in solids. The interaction energy is small ($10^{-6} - 10^{-9}$ eV) and hence the name 'hyperfine' interaction.

In MS one measures the interaction energy which is the product of two terms. One term arises due to the nuclear moment (a nuclear property) and the other arises due to the extranuclear charges and currents (an electronic property of the compound). The total Hamiltonian for nucleus with HI may be written as

$$H = H_0 + E_0 + E_2 + M_1 + \text{higher order terms} \quad (1.5)$$

where

H_0 = the nuclear Hamiltonian (this part has no relevance to MS and this excludes HI).

E_0 = electric monopole interaction (this part gives rise to isomer shift (IS)).

E_2 = electric quadrupole interaction (this part gives rise to quadrupole splitting (QS))

M_1 = magnetic dipole interaction (this part gives rise to nuclear Zeeman effect).

The three interactions arising out of the parts E_0 , E_2 and M_1 are the only interactions studied so far (singly or jointly) with MS. The electric dipole (E_1) interaction is ruled out on symmetry considerations. The interactions of higher order (M_3 , E_4 etc.) are negligible

because their interaction energies are too small to be resolved by MS.

1.2.1 Electric Monopole Interaction

The electric monopole interaction (EMI) affects the position (or the centroid) of the resonance line on the energy (or velocity) scale thus giving rise to the so-called isomer shift (also known as chemical shift). The EMI results from the electrostatic interaction between the charge distribution of the finite-sized nucleus and those atomic electrons which have a finite probability of being found in the nuclear region. The electric monopole interaction energy should, therefore, be proportional to the product of parameters describing the nuclear size and the electronic charge distribution.

In general, in MS, the Mössbauer nuclei in the source and absorber are the same (i.e. the nuclear property does not change) but the environment of the Mössbauer nuclei in the source and absorber differ. This leads to a difference in the transition energy for the source and absorber and no resonance will occur between them. In order to observe the resonance between the source and absorber the transition energy in the Mössbauer nuclei should be modulated either in the source or in the absorber. Such a modulation of transition energy is accomplished by providing a velocity (which can lead to a Doppler energy shift) to either the source or the absorber. The resonance

will take place at a certain velocity v if the modulation in the transition energy is equal to the hyperfine interaction energy such that

$$[E_{\gamma}^s \pm \frac{v}{c} E_{\gamma}] = E^a, \quad (1.6)$$

where the superscripts s and a refer to the source and absorber respectively, E_{γ} is the transition energy of the Mössbauer nucleus and v is the velocity given to the source. This is illustrated in Fig. (1.3).

The isomer shift (IS) is the energy difference of electric monopole interaction energy between source and absorber (or between an absorber and some standard sample like α -Fe, sodium nitroprusside etc. depending on the choice of the reference of IS scale) and it is given by the formula

$$IS_{wrs} = \delta_{wrs} = \frac{4\pi}{5} Ze^2 [R_e^2 - R_g^2] [|\Psi(0)|_a^2 - |\Psi(0)|_s^2] \dots\dots (1.7)$$

where

Z = atomic number of the Mössbauer nucleus

e = electronic charge

R_e, R_g = radius of the excited and ground state of the Mössbauer nucleus respectively

wrs = with respect to the source

$|\Psi(0)|_a^2, |\Psi(0)|_s^2$: the density of atomic s -electrons at the nucleus in the absorber and source respectively.

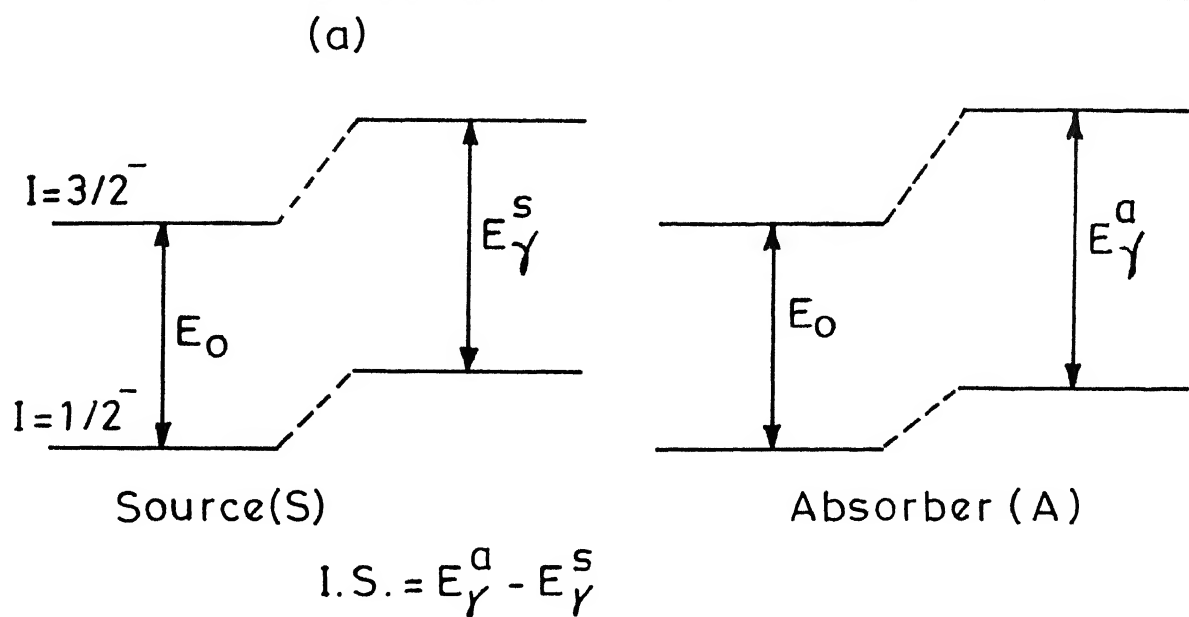


Fig. 1.3 a Effect of monopole interaction on the energy levels of source and absorber.

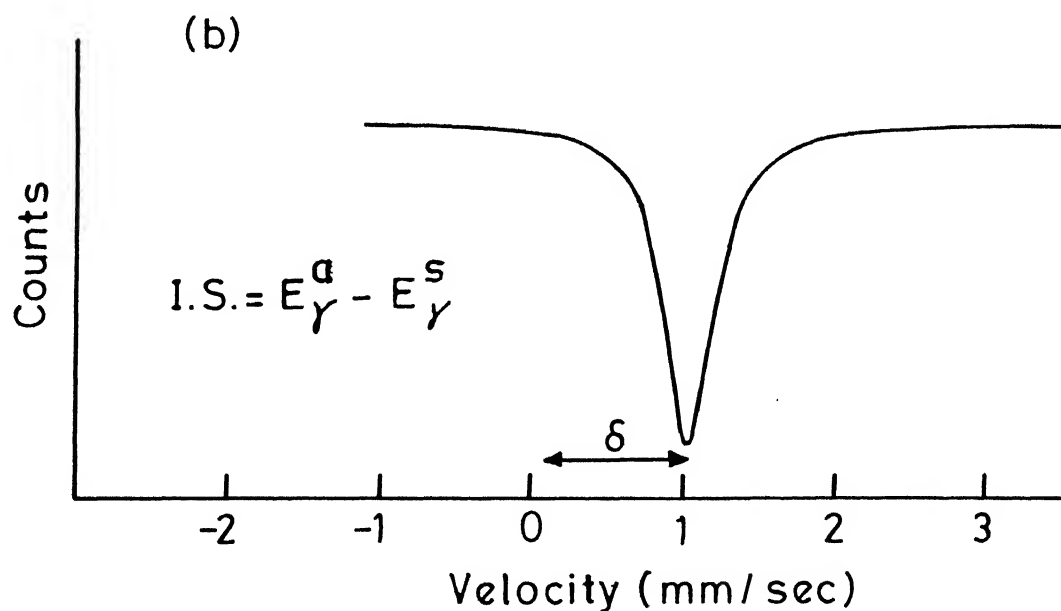


Fig. 1.3 Mössbauer spectrum showing monopole interaction.

In general the IS is measured with respect to some standard absorber, say α -Fe, using the units mm s^{-1} and it is given by the formula

$$\begin{aligned} \text{IS}_{\omega.r.\alpha\text{-Fe}} = & \left(\frac{4\pi c}{5E_\gamma} \right) Z e^2 [R_e^2 - R_g^2] \\ & \times [|\Psi(0)|_a^2 - |\Psi(0)|_{\alpha\text{-Fe}}^2] \text{ mm s}^{-1} \quad (1.8) \end{aligned}$$

where c = velocity of light in mm s^{-1}

E_γ = transition energy E_0

$|\Psi(0)|_{\alpha\text{-Fe}}^2$ = s-electron density at the Mössbauer nucleus in the standard absorber α -Fe.

In the literature, the results for the IS data are quoted with respect to different source or different absorber. Information given in Fig. 1.4 [11] facilitates the conversion from one standard absorber to another.

It is clear from the above discussion of EMI that different oxidation or valence states of Mössbauer atom will lead to different values of $|\Psi(0)|_a^2$ at the nucleus and hence will result in different IS. This is illustrated in Fig. 1.5 [8] and Table 1.4 [12] for ^{57}Fe Mössbauer atom. Not only the valence state, but the different coordination number for the Mössbauer atom will also lead to different $|\Psi(0)|^2$ at the Mössbauer nucleus. We have shown in Fig. 1.6 [9] the plot of the IS for ^{57}Fe Mössbauer atom against the ^{57}Fe coordination number for high and low spin compounds and minerals. The arrow marks on the boxes indicate the possibility that values outside the boxes

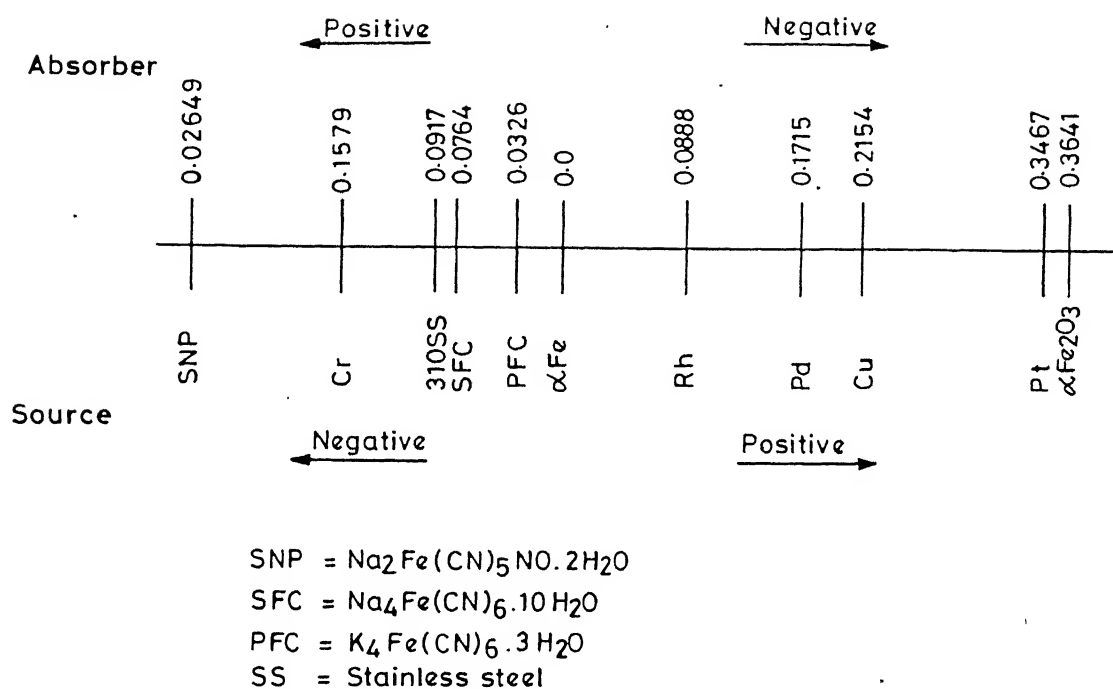


Fig.1.4 Data for the ⁵⁷Fe isomer shift with respect to natural iron (α -Fe) at room temperature. Units of the IS values are mm sec⁻¹ and the signs of the velocity for the source are to be read from the bottom row while the signs of the velocity for the absorber are to be read from the top row.

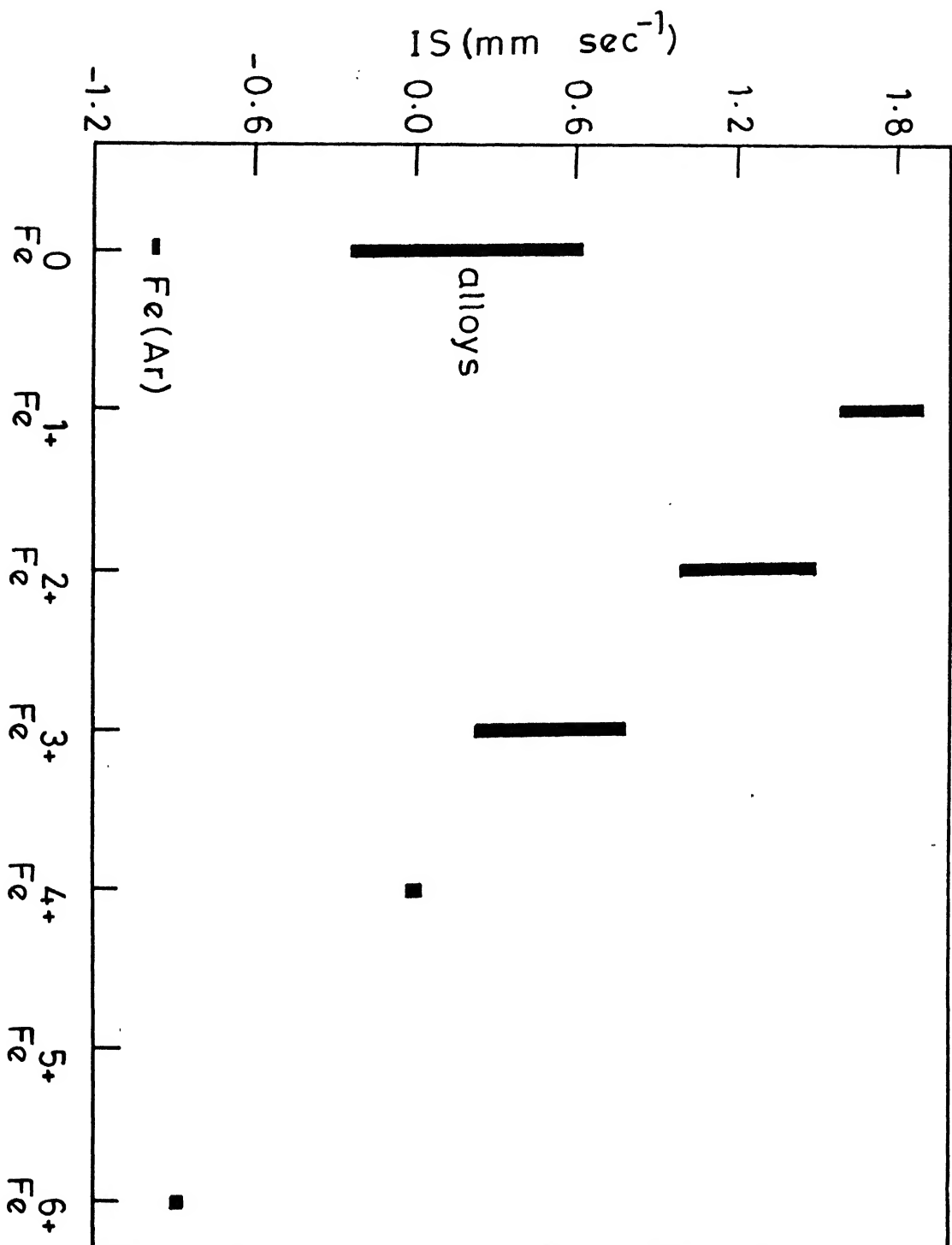


Fig. 1.5 Review of ⁵⁷Fe isomer shift data of iron in various ionization states [8].

Table 1.4 Approximate ranges of isomer shift observed in iron compounds at room temperature (300 K) with respect to ^{57}Fe [12].

Iron state	Spin S	Isomer shift (mm/sec)
Fe^{1+}	$3/2$	1.90 - 2.02
Fe^{2+}	2	0.65 - 1.45
Fe^{3+}	$5/2$	0.10 - 0.51
Fe^{4+}	2	-0.23 - 0.07
Fe^{I}	$1/2$	0.04 - 0.27
Fe^{II}	1	0.21 - 0.43
Fe^{II}	0	-0.34 - 0.31
Fe^{III}	$1/2$	-0.26 - 0.27
Fe^{III}	$3/2$	0.12 - 0.26
Fe^{IV}	1	0.01 - 0.27
Fe^{VI}	1	-0.98 - -0.88

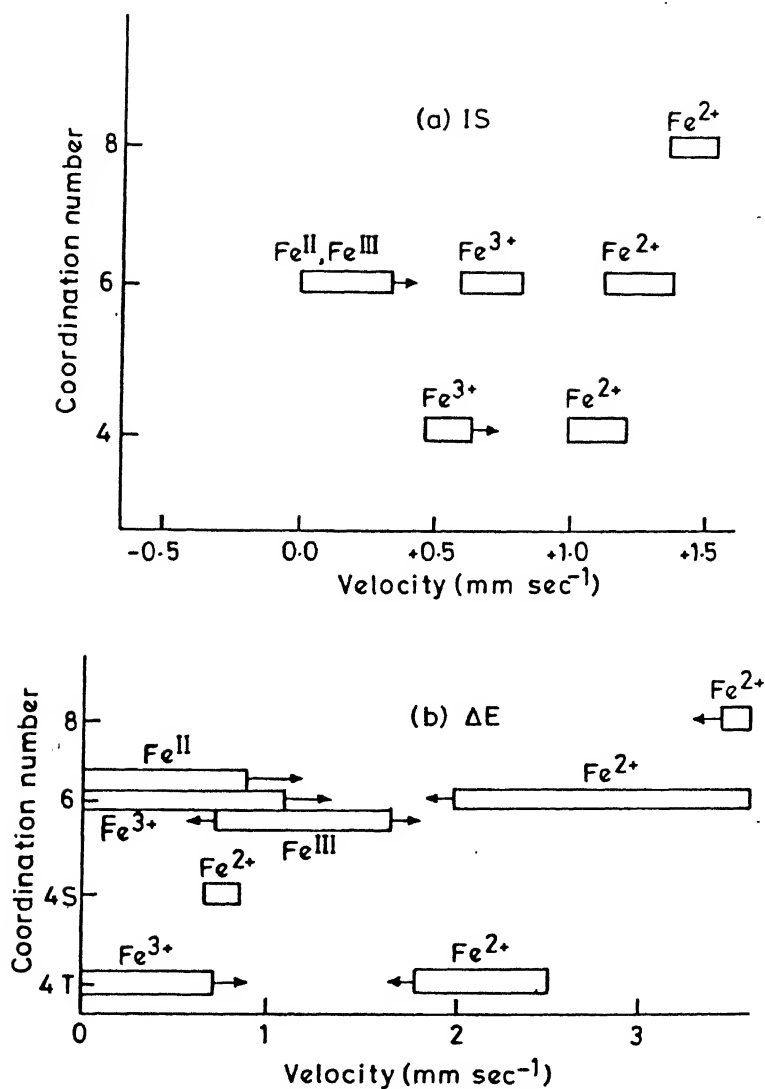


Fig. 1.6 Review of ^{57}Fe Mössbauer parameters (a) IS (isomer shift) and (b) ΔE (quadrupole splitting) for iron plotted against the coordination number for 'ionic' high spin and low spin compounds and minerals. Arrows indicate that the values outside the range of boxes have been observed

may also be found.

In addition to the IS, Mössbauer spectral lines also exhibit a temperature shift, if the source and absorber are kept at different temperatures. This shift arises from the fact that at its lattice site the Mössbauer atom has sufficient mean square velocity depending on the temperature of the solid (arising out of the thermal vibrations of atoms in solids) and hence it is a function of mean square velocity of the Mössbauer atom in solid. This phenomenon is known as second order Doppler effect and the temperature shift is called the second order Doppler shift (SODS). The total shift in energy of the Mössbauer spectral lines can be written as

$$\delta_{\text{total}} = \delta_{\text{IS}} + \delta_{\text{SODS}} \quad (1.9)$$

At a finite temperature T , the Debye Model of the solids leads to the following expression for δ_{SODS} :

$$\delta_{\text{SODS}} = - \frac{3kT}{2Mc}^2 \left[1 + \frac{1}{20} \left(\frac{\Theta_D}{T} \right)^2 \right] \text{ for } T > \Theta_D \quad (1.10a)$$

$$= - \frac{9}{16} \frac{k\Theta_D}{Mc}^2 \left[1 + \frac{8\pi^4}{15} \left(\frac{T}{\Theta_D} \right)^4 \right] \text{ for } T \ll \Theta_D \quad (1.10b)$$

At a temperature which is much lower than the Debye temperature of the lattice the SODS becomes vanishingly small and depends on the relation between T and Θ_D . In view of the above discussion, it is clear that contributions from SODS should be taken into account while interpreting the temperature dependence of IS.

1.2.2 Electric Quadrupole Interaction (EQI)

In the previous discussion of the EMI it was assumed that the nuclear charge distribution is uniform and spherically symmetric. However, in reality, the nuclear charge distribution deviates from spherical symmetry if the spin quantum number of the nucleus $I > 1/2$ and therefore possesses electric multipole moments (2^l , where l is an even number). Let us consider only the electric quadrupole moment which is given by

$$Q_{ij} = \int \rho_n(r) [x_i x_j - \delta_{ij} r^2] d\tau \quad ; d\tau = dx dy dz \quad (1.11)$$

where ρ_n is the nuclear charge density at the point r , (x_i, x_j) are the cartesian coordinates of position vector r and δ_{ij} is the Kronecker symbol. The quadrupole moment Q_{ij} given by (1.11) is described in an arbitrary coordinate system. If one rotates the coordinate system such that all off-diagonal terms of Q_{ij} are zero, then eq. (1.11) reduces to the following expression

$$\begin{aligned} Q &= \frac{1}{e} \int \rho_n(r) (3z^2 - r^2) d\tau \quad ; d\tau = r^2 dr \sin\theta d\theta d\phi \\ &\equiv \frac{1}{e} \int \rho_n(r) r^2 (3 \cos^2\theta - 1) d\tau \end{aligned} \quad (1.12)$$

The coordinate system in which the quadrupole moment tensor has the above form is known as principal coordinate system.

Electric field gradient (EFG) : When Mössbauer nucleus occupies a non cubic site in the lattice, it may experience an electric field gradient (EFG) which is produced by the

extranuclear charges (electrons and lattice charges arranged in non-cubic symmetry) and given by the formula

$$V_{ij} = \frac{\partial^2 V}{\partial_i \partial_j} = q(3\delta_{ij} - r^2 \delta_{ij}) r^{-5} \quad (i, j = x, y, z) \quad \dots \quad (1.13)$$

where V is the potential at the nucleus due to charge q outside the nucleus. In the system of principal axes only the diagonal terms of V_{ij} will exist and if one chooses $|V_{zz}| \geq |V_{yy}| \geq |V_{xx}|$, the EFG can be described by only two independent parameters

i) V_{zz} : electric field gradient in the z -direction of the system of principal axes.

ii) η : Asymmetry parameter defined as follows

$$\eta = \frac{V_{yy} - V_{xx}}{V_{zz}}, \quad 0 \leq \eta \leq 1 \quad (1.14)$$

The total expression for EFG can be written as [3-7]

$$V_{zz} = (1 - \gamma_\infty) (V_{zz})_{\text{lat}} + (1 - R)(V_{zz})_{\text{val}} \quad (1.15)$$

where γ_∞ and R are known as Sternheimer factors arising from the fact that $(V_{zz})_{\text{lat}}$ (the contribution to EFG from external charges of Mössbauer atom) and $(V_{zz})_{\text{val}}$ (the contribution to EFG from the valence electrons and partially filled inner electron shells of Mössbauer atom) polarize the spherically symmetric inner electron shells and alter the total EFG respectively.

Quadrupole splitting : The quadrupole moment eQ of the nucleus interacts with EFG at the nucleus. The interaction energy which is proportional to the product of a nuclear

parameter (eQ) and an atomic parameter (EFG), is measured in the Mössbauer spectrum and is known as quadrupole splitting (QS). The interaction Hamiltonian of electric quadrupole moment and EFG can be written as [3-7]

$$E_2 = \frac{eQ V_{zz}}{4I(2I-1)} [3 I_z^2 - I^2 + \eta (I_+^2 - I_-^2)/2] \quad (1.16)$$

where I = nuclear spin operator

$$I_{\pm} = I_x \pm iI_y = \text{shift operators}$$

I_x, I_y, I_z : nuclear spin component operators.

The energy eigenvalues of operator E_2 corresponding to the eigenvector $|I m_I\rangle$ is given by

$$E_Q = \frac{eQ V_{zz}}{4I(2I-1)} [3m_I^2 - I(I+1)] [1+\eta^2/3]^{1/2} \quad (1.17)$$

where $m_I = I, I-1, \dots, -I$, is the magnetic spin quantum number. For a four fold or three fold axis of symmetry passing through the Mössbauer nucleus as the center of symmetry, $V_{xx} = V_{yy}$ and $\eta = 0$, the EFG in this case will be axially symmetric and the electric quadrupole interaction energy is given as

$$E_Q = \frac{eQ V_{zz}}{4I(2I-1)} [3m_I^2 - I(I+1)] \quad (1.18)$$

Let us consider the case of ^{57}Fe for the transition

$$I = 3/2 \rightarrow I = 1/2$$

i) For $I = 1/2$, $Q = 0$ and this leads to No change in the ground state

ii) For $I = 3/2$ eq. (1.18) leads to the splitting of the level into a doublet with the energy shifts given by

$$E_Q(m_I = \pm 3/2) = \frac{1}{4} eQ V_{zz} \text{ for } I = 3/2, m_I = \pm 3/2$$

$$E_Q(m_I = \pm 1/2) = -\frac{1}{4} eQ V_{zz} \text{ for } I = 1/2, m_I = \pm 1/2$$

..... (1.19)

and the energies of the two substates become $(E_o + \frac{1}{4} eQ V_{zz})$ and $(E_o - \frac{1}{4} eQ V_{zz})$ as shown in Fig. 1.7. In MS studies one normally uses a so-called single line (or unsplit) source of $^{57}\text{Co} \rightarrow ^{57}\text{Fe}$ which gives photons of energies $(E_o \pm \Gamma + \delta_{\text{source}})$. In order to observe the QS (if it exists) in the absorber, one should modulate the energy of the source (absorber) by providing it Doppler velocity equal to $(\pm eQ V_{zz}/4)$ and EMI energy δ . With ^{57}Fe ($I = 3/2, 1/2$) therefore the Mössbauer spectrum will show two absorption lines at velocities $v_{1(2)}$ such that

$$v_{1(2)} = \begin{pmatrix} + \\ - \end{pmatrix} \frac{eQ V_{zz}}{4} (C/E_o) \quad (1.20)$$

The QS energy (ΔE) for the absorber is given as

$$\Delta E = \frac{1}{4} eQ V_{zz} - (-\frac{1}{4} eQ V_{zz}) = \frac{1}{2} eQ V_{zz} \quad (1.21)$$

Measurement of quadrupole splitting energy (ΔE) in the Mössbauer spectrum provides valuable information about the sample under investigation. One can determine the valence state of the Mössbauer atom, its coordination number etc. (Fig. 1.6b) by measuring the ΔE values from the Mössbauer spectrum. A study of the temperature

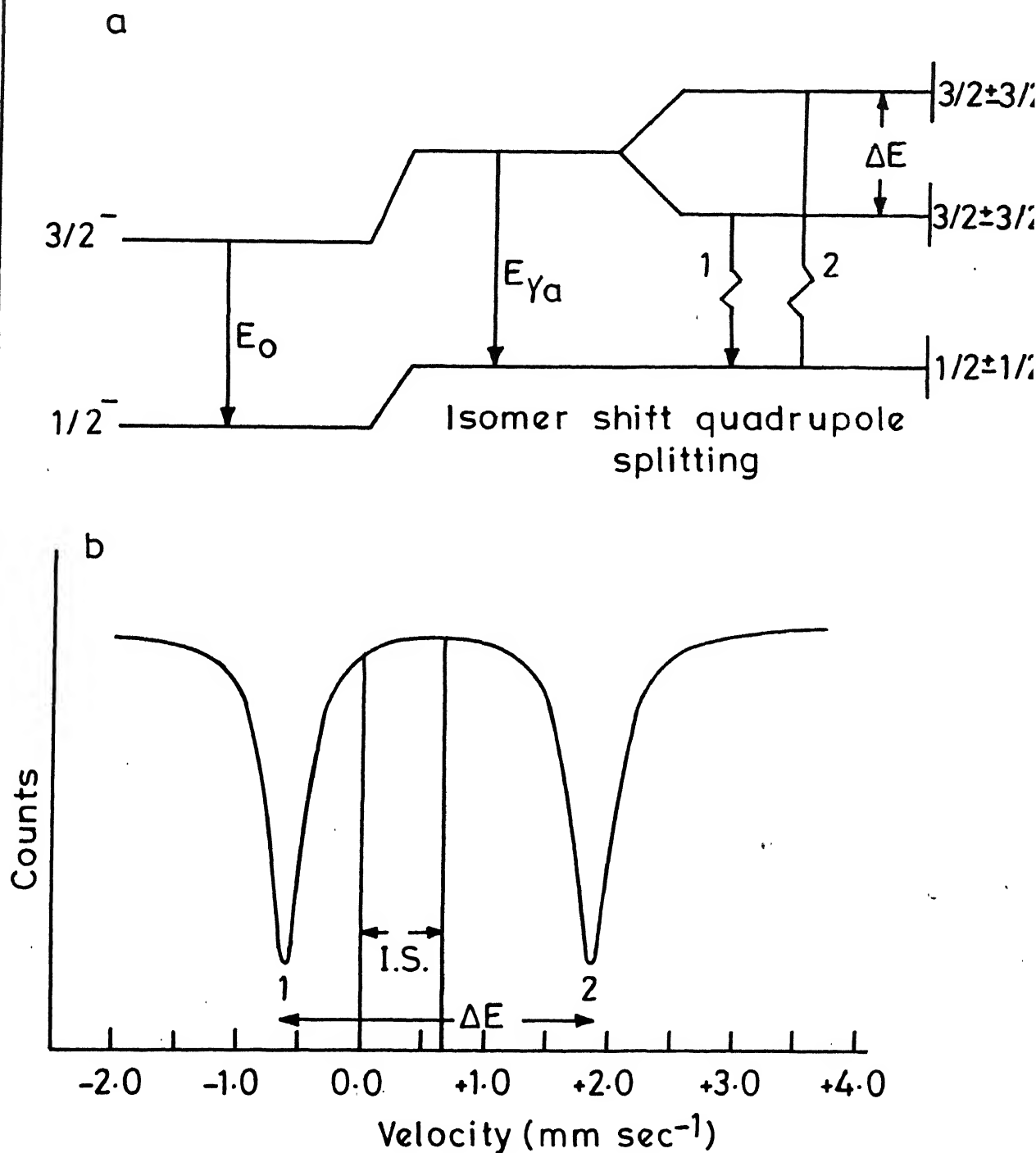


fig.1.7 Effect of the quadrupole interaction on the nuclear energy levels of source / absorber and the resulting Mössbauer spectrum showing the quadrupole splitting and isomer shift.

variation of ΔE can be used to investigate temperature induced structural or chemical phase changes. When a single crystal is used as a sample under investigation (or by applying external magnetic field to the powdered sample) the direction of $eQ V_{zz}$ can be determined by measuring the position intensity of the resonance lines.

1.2.3 Magnetic Dipole Interaction

Nuclei with spin $I > 0$ possess magnetic multipole moments (2^l , $l = \text{odd number}$). Here one can consider only the magnetic dipole moment μ which is given by

$$\mu = g_N \beta_N I \quad (1.22)$$

where g_N is the nuclear Lande splitting, g factor and $\beta_N = eh/2M = \text{nuclear magneton}$.

The effective magnetic field, H_{eff} , at the Mössbauer nucleus is

$$H_{\text{eff}} = H_{\text{ext}} + H_{\text{int}} \quad (1.23)$$

where H_{ext} is the externally applied magnetic field and H_{int} is the internal magnetic field having contributions from three terms as given below

$$H_{\text{int}} = H_c + H_L + H_d \quad (1.24)$$

where H_c = Fermi contact field which arises from a net s electron spin density at the nucleus as a consequence of spin polarization of inner filled s-shell by spin polarized partially filled outer shells.

H_L = contribution from the orbital motion of valence and partially filled inner shell electrons

H_d = spin dipolar term arising from the spin of the electrons outside the Mössbauer atom.

Magnetic splitting : The magnetic dipole moment μ can interact with an effective magnetic field H_{eff} at the nucleus. The Hamiltonian M_1 for this interaction (which is also called magnetic dipole interaction or nuclear Zeeman effect) is given by

$$M_1 = -\mu H_{\text{eff}} = -g_N \beta_N I H_{\text{eff}} \quad (1.25)$$

The energy eigenvalue of M_1 corresponding to the eigenvector $|I m_I\rangle$ is given by

$$E_M(m_I) = -\mu H m_I / I = -g_N \beta_N H m_I \quad (1.26)$$

It is obvious from eq. (1.26) that this interaction causes a nuclear state $|I m_I\rangle$ to split into $(2I+1)$ substates ($|I m_I\rangle$, $|I m_I-1\rangle$, ..., $|I -m_I\rangle$).

Let us consider the case of ^{57}Fe in which there is a transition between the states $|I = 3/2 m_I\rangle$ and $|I = 1/2 m_I\rangle$. The state $I = 3/2$ will be split into four substates with an energy splitting which is $\mu_e H m_{I_e} / I_e$ with respect to the energy of the unperturbed (or unsplit) state. Similarly the state $I = 1/2$ will be split into two substates with an energy splitting of $(\mu_g H m_{I_g} / I_g)$. In the above discussion the suffixes e and g refer to the excited state $I = 3/2$

and the ground state $I = 1/2$ respectively. This is shown in Fig. 1.8. Taking into account the selection rule $\Delta m_I = 0, \pm 1$ the transitions for $I_e = 3/2$ to $I_g = 1/2$ give rise to six symmetric lines with respect to the centroid. The centroid in the spectrum is the position of spectral lines if the $I_e = 3/2$ and $I_g = 1/2$ were not split.

The relative intensities of all six resonance lines depend on the m_I values involved in the transitions and the relative angle Θ between the quantisation axis and the gamma propagation direction. In the case of ^{57}Fe , the relative intensities of the six lines are in the ratio [7]

$$\begin{aligned} & \left(\frac{3}{2} \frac{3}{2} \rightarrow \frac{1}{2} \frac{1}{2}\right) : \left(\frac{3}{2} \frac{1}{2} \rightarrow \frac{1}{2} \frac{1}{2}\right) : \left(\frac{3}{2} \frac{1}{2} \rightarrow \frac{1}{2} \frac{1}{2}\right) \\ & : : \left(\frac{3}{2} + \frac{1}{2} \rightarrow \frac{1}{2} - \frac{1}{2}\right) : \left(\frac{3}{2} - \frac{1}{2} \rightarrow \frac{1}{2} - \frac{1}{2}\right) : \left(\frac{3}{2} - \frac{3}{2} \rightarrow \frac{1}{2} - \frac{1}{2}\right) \\ & = 3:Z:1 :: 1:Z:3 \end{aligned} \quad (1.27)$$

where $Z = 4/(1 + \cos^2 \Theta)$.

For polycrystalline (powdered) samples all orientations are equally probable and the averaging over Θ gives $Z = 2$.

In order to observe the Zeeman splitting in the absorber (if it exists), a source (^{57}Co) which emits photons of energy $(E_0 \pm \Gamma + \delta)$ is used and the energy of the photon is modulated by providing the source (absorber) with a Doppler velocity v given by

$$v(m_{I_e}, m_{I_g}) = \delta + \mu_g H \left(\frac{c}{E_0} \right) \left[-\frac{m_{I_g}}{I_g} - \frac{m_{I_e}}{I_e} \left(\frac{\mu_e}{\mu_g} \right) \right] \quad (1.28)$$

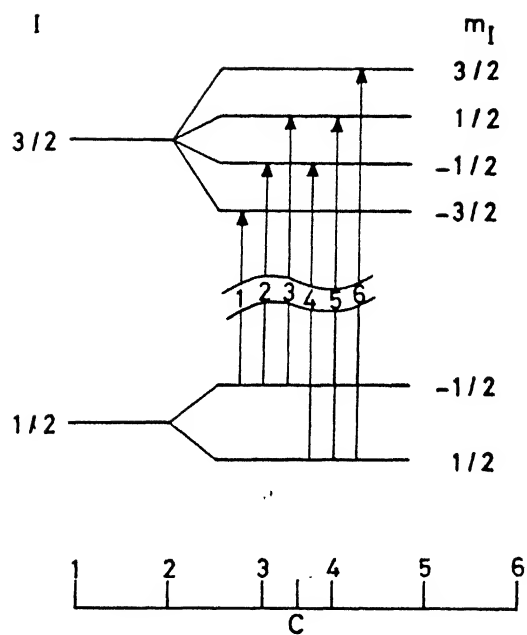


Fig.1-8 Effect of magnetic hyperfine interaction on energy levels of ^{57}Fe . Peak positions of the six-finger pattern are shown at the bottom. (C = Centroid)

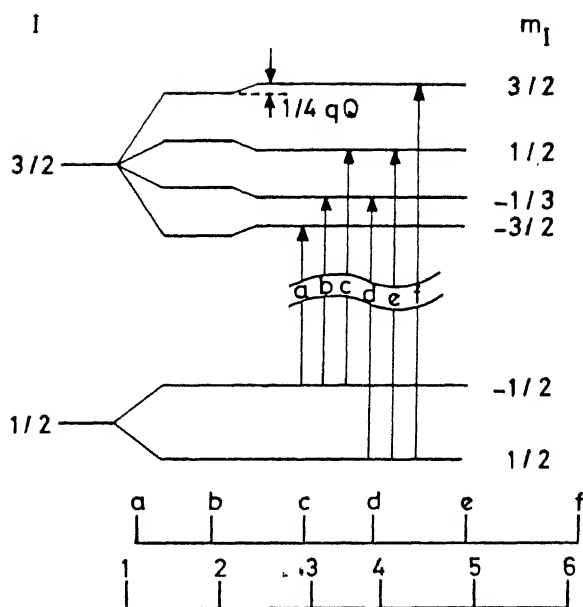


Fig.1-9 Effect of weak quadrupole interaction and a strong magnetic interaction on the energy levels of ^{57}Fe . The numbers 1 to 6 refer to those in Fig.1-8.

By measuring the positions of the resonance lines in the Mössbauer spectrum we can find out $H_{\text{eff}} = H$ at the ^{57}Fe nucleus as follows

$$E\left(\frac{3}{2} \frac{1}{2} \rightarrow \frac{1}{2} \frac{1}{2}\right) - E\left(\frac{3}{2} \frac{1}{2} \rightarrow \frac{1}{2} - \frac{1}{2}\right) = \frac{E_0}{c} \left(\nu\left(\frac{3}{2} \frac{1}{2} \rightarrow \frac{1}{2} \frac{1}{2}\right) - \nu\left(\frac{3}{2} \frac{1}{2} \rightarrow \frac{1}{2} - \frac{1}{2}\right) \right) \\ = \mu_g H / (1/2) \quad (1.29)$$

$$E\left(\frac{3}{2} \frac{3}{2} \rightarrow \frac{1}{2} \frac{1}{2}\right) - E\left(\frac{3}{2} \frac{1}{2} \rightarrow \frac{1}{2} \frac{1}{2}\right) = \frac{E_0}{c} \left(\nu\left(\frac{3}{2} \frac{3}{2} \rightarrow \frac{1}{2} \frac{1}{2}\right) - \nu\left(\frac{3}{2} \frac{1}{2} \rightarrow \frac{1}{2} \frac{1}{2}\right) \right) \\ = \mu_e H (3/2) \quad (1.30)$$

The value of $\mu_g = 0.0903 \pm 0.0007$ has been determined [13] with the help of other techniques. Using the values of μ_g , E_0 , c etc. in eq. (1.29) one gets the value of H as

$$H = 0.843 \times 10^5 \left[\nu\left(\frac{3}{2} \frac{1}{2} \rightarrow \frac{1}{2} \frac{1}{2}\right) - \nu\left(\frac{3}{2} \frac{1}{2} \rightarrow \frac{1}{2} - \frac{1}{2}\right) \right] \text{ Oersted}$$

$$H = 0.843 \times 10^5 [L_5 - L_3] \times \text{calibration} \\ \text{constant (mm s}^{-1} \text{ channel}^{-1}) \text{ Oersted}$$

where L_3 and L_5 are the positions of the third and fifth lines.

The study of effective magnetic fields at the nuclear sites has been very useful for understanding the magnetic properties of solids at atomic scale. The value of the magnetic moment of the excited state can also be determined (eq. 1.30) with the help of Mössbauer spectroscopy.

1.2.4 Mixed Magnetic Dipole and Electric Quadrupole Interaction

In magnetic materials, if the Mössbauer atoms (^{57}Fe) occupy the site of non-cubic symmetry, the Mössbauer nuclei

experience EFG as well as H_{int} . The general theory of combined magnetic dipole and electric quadrupole has been discussed in several books [5-7] and papers [14-16]. Here we shall consider the special case, the $3/2 \rightarrow 1/2$ transition in the limit when electric quadrupole interaction E_2 is very much smaller than the magnetic dipole interaction M_1 ($E_2 \ll M_1$). In general the axis of the principal component V_{zz} of the EFG forms an angle β with the axis of the magnetic field. Assuming the EFG tensor to be axially symmetric, i.e. $\eta = 0$, a first order perturbation treatment yields the general expression for the eigenvalues of the nuclear sublevels.

$$E_{M_1, E_2}(I, m_I) = -g_N \beta_N H m_I + (-1)^{|m_I|} + \frac{1}{2} \left(\frac{eQ V_{zz}}{8} \right) (3 \cos^2 \beta - 1) \dots \quad (1.31)$$

It is obvious from eqn. (1.31) that the sublevels $|3/2 \pm 3/2\rangle$ are shifted by an amount $\left(\frac{eQ V_{zz}}{8} \right) (3 \cos^2 \beta - 1)$ to the higher energy and sublevels $|3/2 \pm 1/2\rangle$ are shifted to the lower energy as shown in Fig. 1.9. As a result the six-line spectrum will not be symmetric with respect to the centroid. The sublevels spacing and thus the asymmetry of the spectrum are directly correlated to the sign and strength of the V_{zz} . Hence by measuring the spacing and asymmetry, one can find out the sign of the EFG of a polycrystalline sample from a magnetically split Mössbauer spectrum.

1.3 SUPERPARAMAGNETISM

So far, it is assumed that the HI are time independent. However, the electron spin may flip from $|+\frac{1}{2}\rangle$ to $|-\frac{1}{2}\rangle$ state and as a result the magnetic hf field at the nucleus turns over an angle of 180° . The Larmor frequency of the nucleus ω_L is a measure of the time required by the nucleus for recognizing the direction of the hyperfine field. In most situations one of the extreme cases is encountered.

- (a) $\omega_R \ll \omega_L$, where ω_R is the frequency of the electron spin flip. The electron spin will not flip during one Larmor precession of the nucleus. Therefore, the nucleus experiences a stationary hyperfine field.
- (b) $\omega_R \gg \omega_L$, during one nuclear Larmor precession, many electron spin flips take place and the nucleus experiences an average zero field.

In ultrafine particles of ferri, ferro and antiferro magnetically ordered substances the magnetization and therefore H_{int} may fluctuate very fast by thermal excitation. Due to anisotropies each magnetic single domain particle may possess more than one easy direction for the magnetization vector. In all small isotropic particles all easy directions are equally probable for magnetization. The magnitude of relaxation time τ [17] depends on the balance of energies KV (anisotropy energy) and $k_B T$ (thermal energy) given as follows

$$\tau = \frac{1}{f_0} \exp\left(\frac{KV}{k_B T}\right) \quad (1.32)$$

f_0 - Debye Waller factor.

where

K : a constant describing the lattice anisotropy

V : volume of the particle.

For $KV/k_B T < 25$, the thermal fluctuations of the magnetization vectors take place without showing hysteresis effect [18] and the nucleus experiences zero hyperfine field. This phenomenon is called superparamagnetism.

REFERENCES

1. R.L. Mössbauer, Z. Physik 151, 124 (1958); Z. Naturforsch. 149, 211 (1959).
2. R.L. Cohen (Ed), 'Application of Mössbauer Spectroscopy' Vol. 1, Academic Press, New York (1976).
3. L. May (Ed), 'An Introduction to Mössbauer Spectroscopy' Plenum Press, New York and London (1971).
4. G.K. Wertheim, 'Mössbauer effect : Principles and Applications' Academic Press, New York and London (1964).
5. U. Gonser (Ed), 'Mössbauer Spectroscopy', Springer-Verlag, Berlin (1975).
6. V.G. Bhide, 'Mössbauer effect and its Applications' Tata McGraw Hill Publishing Co. Ltd., New Delhi (1973).
7. V.I. Goldanskii and R.H. Herber (Eds), 'Chemical Applications of Mössbauer Spectroscopy', Academic Press, New York and London (1968).
8. G.K. Shenoy and F.E. Wagner (Eds), 'Mössbauer Isomer Shifts' North-Holland, Amsterdam (1978).
9. H.J. Lipkin, 'AIP Conference Proceeding', 38, 63 (1977).
10. J.G. Stevens and L.H. Bowen, Anal. Chemistry 48, 232R (1976). Page 178
11. J.G. Stevens and W.L. Gettys, 'Int. Conf. on the Appl. of the Mössbauer effect' Jaipur, India Dec. 14-18 (1981).
12. N.N. Greenwood and T.C. Gibb, 'Mössbauer Spectroscopy' Plenum Press, New York and London (1971).
13. G.W. Ludwig and H.H. Woodbury, Phys. Rev. 117, 1286 (1960).

14. Van Dongen Torman, J.R. Jagannathan and J.M. Trooster, Hyperfine interaction 1, 135 (1975).
15. S.V. Karyagin, Soviet Phys. Solid State 8, 391 (1966); Soviet Phys. Solid State 8, 1387 (1966) .
16. W. Kundig, Nucl. Instr. and Meth. 48, 215 (1967).
17. L. Neel, Ann. Geo. Phys. 5, 59 (1949).
18. K. Muller, F. Thurley, Int. J. Magnetism, 5, 203 (1973).

CHAPTER 2

EXPERIMENTAL METHODS

2.1 INTRODUCTION

In this chapter we shall describe the experimental set up (Mössbauer spectrometer etc.) used in the present work. We shall provide brief outline of our apparatus and shall underline those important aspects of the experimental technique (e.g. efficient functioning of the Mössbauer spectrometer, thickness of absorber, geometrical effects etc.) which are necessary to obtain a good Mössbauer spectrum. The procedure followed for the analysis of data is also described.

2.2 MÖSSBAUER SPECTROMETER

Mössbauer spectrometers have been standardised during the last two decades. Essentially a Mössbauer spectrometer consists of the following units :

- (i) Source of gamma-ray photons which can emit recoil-free gamma-ray photons that are capable of exciting the nuclei in the absorber under study.
- (ii) Mössbauer drive which can provide relative velocities between the source and absorber, usually with a constant acceleration.
- (iii) Absorber.

- (iv) Gamma-ray detection system.
- (v) Data acquisition, storage and handling system.
- (vi) Cryostat and/or furnace system which can maintain the absorber and/or the source at different temperatures.

An appropriate and optimum combination of the above parts forms a good Mössbauer spectrometer. The schematic block diagram of the Mössbauer spectrometer used by us is shown in Fig. 2.1.

2.2.1. Gamma-ray Photon Source

In the present work Mössbauer studies have been carried out in two different ways. In the first method we used a 'single-line source' of radioactive ^{57}Co diffused in Rh matrix as the Mössbauer source. Different samples under study were used as Mössbauer absorbers and Mössbauer spectra of these samples were recorded in the transmission mode. In the second method, solution of radioactive ^{57}Co (as $^{57}\text{CoCl}_2$) was diffused into the material under study (cobaltates, details given in Chapter 4) and these samples were used as Mössbauer sources and Mössbauer spectra in transmission mode were recorded using stainless steel (SS 310) and potassium ferrocynide as Mössbauer absorbers. In the remaining part of the chapter, however, our discussion will be limited to the first method i.e. use of single-line source as Mössbauer source. The desirable properties of a single-line source are as follows :

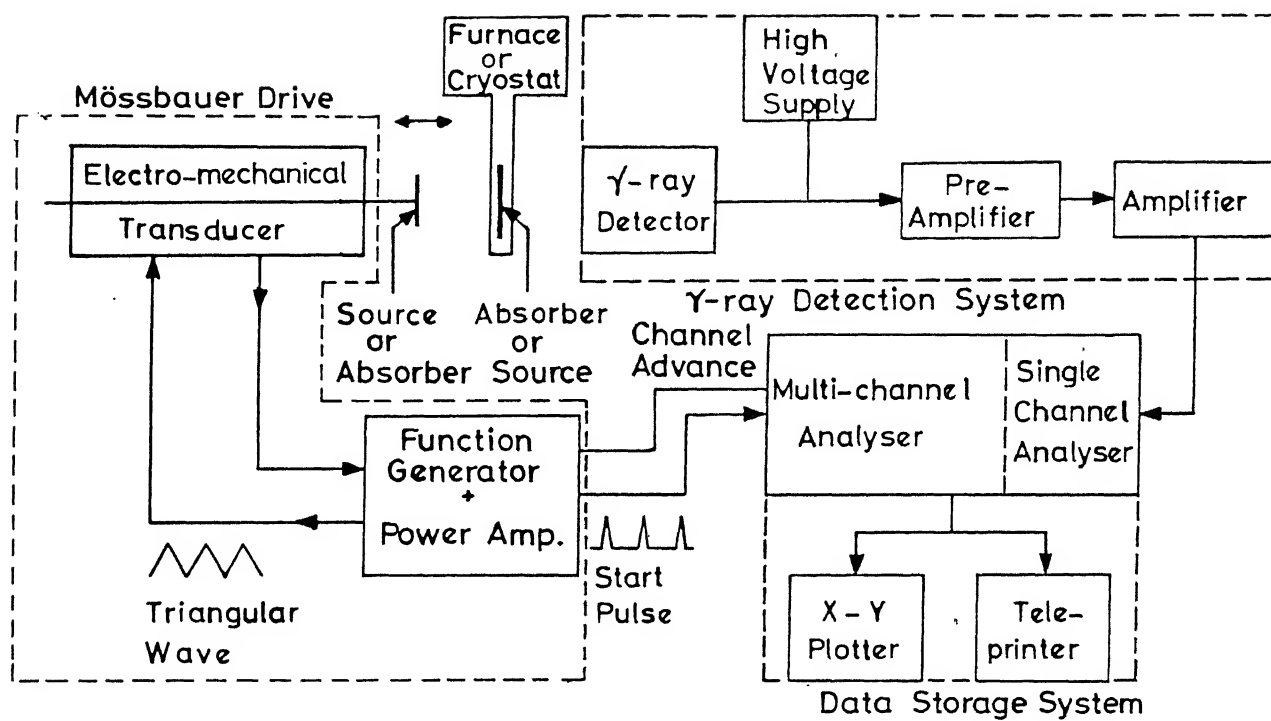


Fig. 2.1 Schematic block diagram of Mössbauer spectrometer.

- (i) The source material should be deposited in a host matrix which should be chemically inactive and stable.
- (ii) There should be no EFG or H_{int} at the source nucleus.
- (iii) The recoilless fraction in the given source matrix should be large.
- (iv) The source material should be deposited in a thin foil over a small area to keep the line-broadening to a minimum.
- (v) Radiation not contributing to the Mössbauer effect (such as characteristic X-rays and other gamma rays) should have a minimum contribution in the energy window selected for the Mössbauer 'signal' radiation.

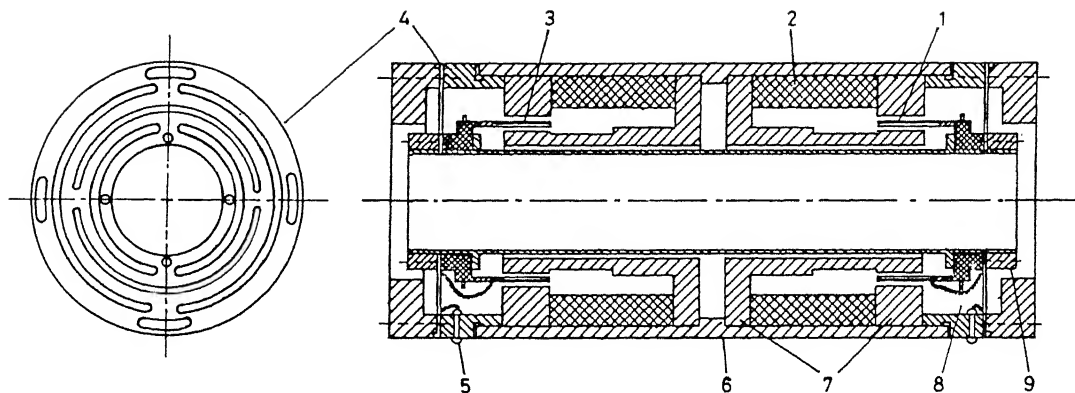
In our experiments we used as Mössbauer source a radioactive source of ^{57}Co deposited in 6 μm thick rhodium metal foil. Its initial activity was 25.5 mCi and it had a recoil-free fraction equal to 0.76_{at 293K.} This source was purchased from New England Nuclear Inc., U.S.A. and its properties came close to the ideal specifications mentioned above.

2.2.2 Mössbauer Drive

The Mössbauer **drive** consists of a velocity transducer, function generator and power amplifier. The modern Mössbauer velocity transducer [1-2] is based on principle of two mechanically coupled loudspeakers. The velocity transducer consists of rigidly connected (driving

and pick-up) coils wound on the same holder. The permanent magnets produce a homogeneous magnetic field (in the air gap of the coil system) which is constant within few parts in 10^4 along the axis of motion. The constant magnetic field ensures a high linearity of the driving system. The magnetic induction is approximately 0.25 tesla. The function generator produces a reference signal which is fed to the power amplifier. The output of the power amplifier which is proportional to the ^{integral of the} ideal velocity of the transducer, is provided to the driving coil. The actual velocity is sensed by the pick-up coil in the form of pick-up signal. The difference between the reference signal and the pick-up signal is known as the difference (or error) signal. This difference signal is proportional to the deviation of the actual velocity from its correct (stipulated) value. The difference signal is amplified and fed back to the driving coil through a feed-back loop amplifier to minimise the deviation from the ideal velocity.

Out of the two Mössbauer spectrometers used in the present work, one uses the velocity transducer (Model MA-260), the function generator (Model DFG-1200) and the driving unit (power amplifier, Model MR-360), all manufactured by Wissel, West Germany. The schematic diagram of the velocity transducer is shown in Fig. 2.2. The other Mössbauer spectrometer consists of a velocity transducer which was designed (see Fig. 2.3) and developed [3] in our laboratory



1-Pickup coil, 2-Permanent magnet, 3-Drive coil, 4-Guide spring,
5-Electrical feed through, 6-Connecting tube, 7-Magnet yokes, 8-Coil shell,
9-Flange for mounting source.

Fig. 2.2 Electromechanical Transducer.

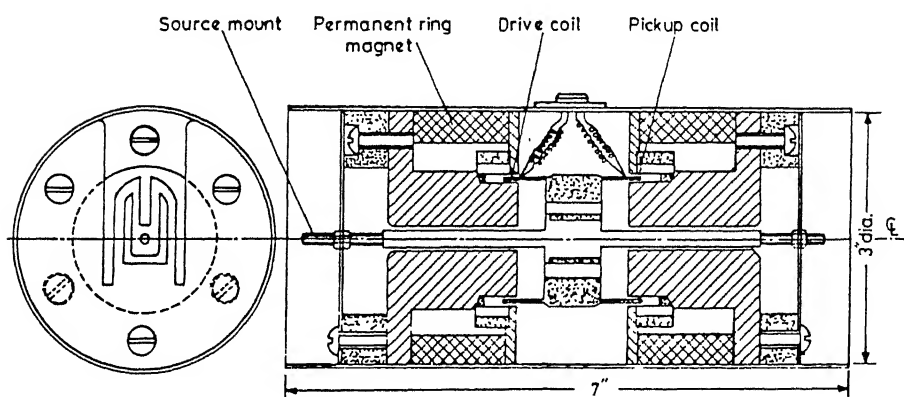


Fig.2.3 Schematic block diagram of the electromechanical transducer used in the
Mössbauer spectrometer.

but built by M/s Encardio Rite, Lucknow, India. The function generator used in this spectrometer was Model MFG-30 built by Gyanic Instruments, India while the power amplifier was designed and fabricated in our laboratory. The basic principle of both the transducers was same with some slight differences. While recording the Mössbauer spectra care was taken to use the same spectrometer for the same family (type) of samples.

2.2.3 Absorbers

Two different types of absorbers were used in the present work. The first type comprised of the standard absorbers which were used to calibrate the Mössbauer spectrometer and to study the ^{57}Co source deposited in the cobaltate samples while the second type of absorbers were the samples under investigation. The standard absorbers of the first type consisted of (i) natural iron foil (25 μm thick) ($\alpha\text{-Fe}$), (ii) 310 stainless steel (310 SS), (iii) enriched potassium ferrocyanide (PFC), (iv) sodium nitroprusside (SNP) and (v) ferric oxide ($\alpha\text{-Fe}_2\text{O}_3$). All these standard absorbers were obtained from the Amersham International Ltd., Amersham, U.K.

The sample absorbers under investigation were prepared in the following manner. About 30 to 40 mg of powdered material under study was spread uniformly on a circular area of 1 cm dia. on a cello tape (scotch tape) and covered by another

layer of cellotape to form a 'sandwich' absorber. Sample absorbers which needed measurements at high temperatures were prepared by making a sandwich absorber between the layers of mica or aluminium foils.

2.2.4 Gamma-ray Photon Detection System

Gas-filled sealed proportional counter (PC) was used to detect the gamma-ray photons transmitted by the absorber. The PC receives the gamma-ray photons and converts them into linear charge pulses (electrical pulses). These charge pulses are received by the preamplifier which gives as output, a set of linear tail voltage pulses. The amplitude (height) of the linear tail pulses is directly proportional to the energy of the gamma-ray photons received by the PC. A power supply capable of supplying high voltage (1500-3000 V at 100 μ A - 1 mA) is required to operate the PC. The output pulses from the preamplifier are further fed into a linear amplifier (LA). The LA delivers output pulses in the range 0 - 10 V and these pulses carry the energy information about the gamma-ray photons which are received by the PC [4,5]. Before recording the Mössbauer spectrum in the transmission mode it is necessary to fix the 'energy window' of the gamma-ray spectrum to ensure that the appropriate 14.4 keV (in the case of ^{57}Co - ^{57}Fe Mössbauer nuclei) gamma-rays are selected. This is achieved either by using a single channel analyzer (SCA) or by using a

multichannel analyzer (MCA) in the pulse height analysis (PHA) mode.

In our laboratory there were two Mössbauer spectrometers which were used in the present work. The first spectrometer consisted of the following units :

- (i) PC : Model No. I 1331; ECIL.
- (ii) Pre-amplifier : Model No. 401, Mechtronics; U.S.A.
- (iii) H.V. Power Supply : Model No. 3002, Canberra; U.S.A.
- (iv) LA/TSCA : Model No. 2015A, Canberra; U.S.A.

The other spectrometer comprised of the following units :

- (i) PC : Model No. RS-P3-1605-261 (97% Xenon + 3% CO₂ at 1 atoms pressure), Reuter-Stokes; U.S.A.
- (ii) Pre-amplifier : Model No. 2006, Canberra; U.S.A.
- (iii) H.V. Power Supply : Model No. 456, EG and G ORTEC; U.S.A.
- (iv) Spectroscopy Amplifier : Model No. 2021, Canberra; U.S.A.

2.2.5 Data Acquisition, Storage and Handling System

Multichannel analyzer (MCA) was used in the pulse height analysis (PHA) mode for recording pulse height spectrum and in the multichannel scaling (MCS) mode for recording the Mössbauer spectrum. Data acquired in the MCA was printed out using a Teletype printer which was interfaced with the MCA. In our work we used Nuclear Data

Model No. ND-60, Model No. ND-62 and Canberra Model No. S-80 MCA's depending upon the availability.

2.2.6 Cryostat and Furnace

In order to study the effect of temperature on the absorber (source) under study it is necessary to maintain the absorber at a desired temperature during the measurement of the Mössbauer spectra. This is achieved by placing the absorber (source) inside the cryostat or a furnace and by maintaining the temperature with the help of a cryogenic arrangement or heater and a stable temperature controller.

A liquid nitrogen cryostat in which temperature can be maintained from 80 K to 300 K was fabricated in our laboratory. The schematic diagram of the cryostat is shown in Fig. 2.4. The two concentric cylindrical brass vessels are connected by a thin-walled stainless steel tube. Liquid nitrogen is kept inside the inner vessel and it can be poured from time to time through the thin-walled stainless steel tube. The outer brass cylinder provides thermal insulation for the cryogenic vessel and for the cold finger (which was a 3-cm dia copper rod and which is attached to the inner vessel) when vacuum is maintained between two concentric brass cylinders with the help of an oil-diffusion pump. The Mössbauer absorber under study is put in the 1 cm dia. holder which is located in the cold finger along the direction of the mylar windows. Mylar windows allow

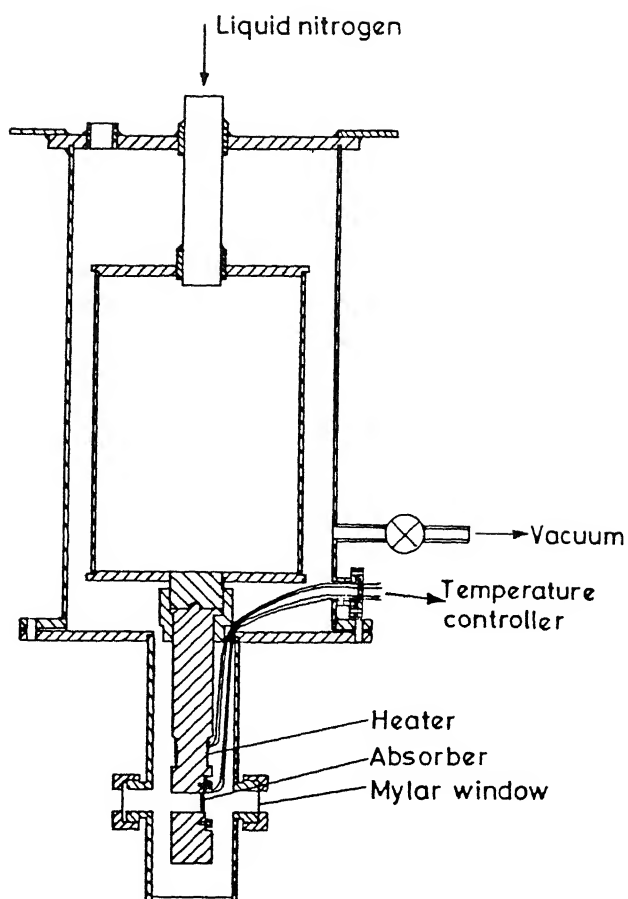


Fig.2.4 Design of the cryostat used in the Mössbauer experiments carried out in temperature range 80-300 K.

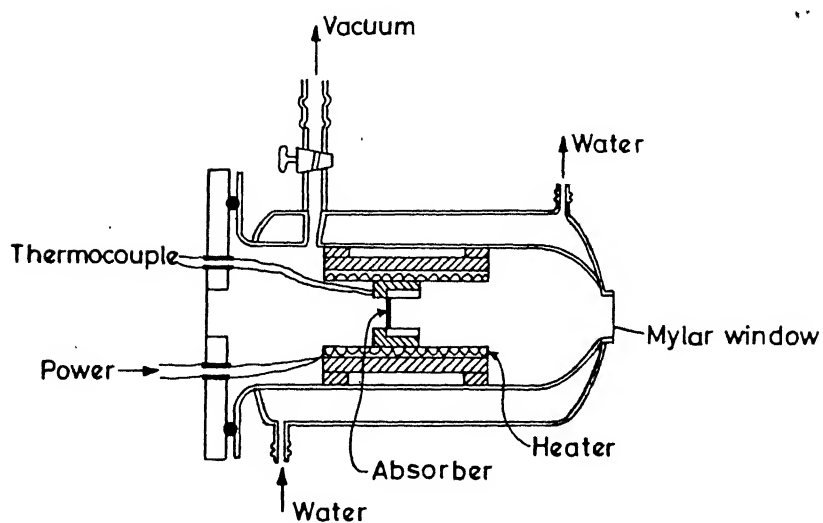
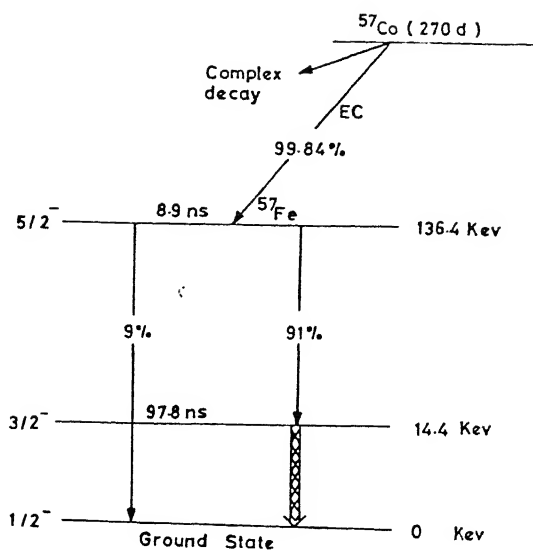
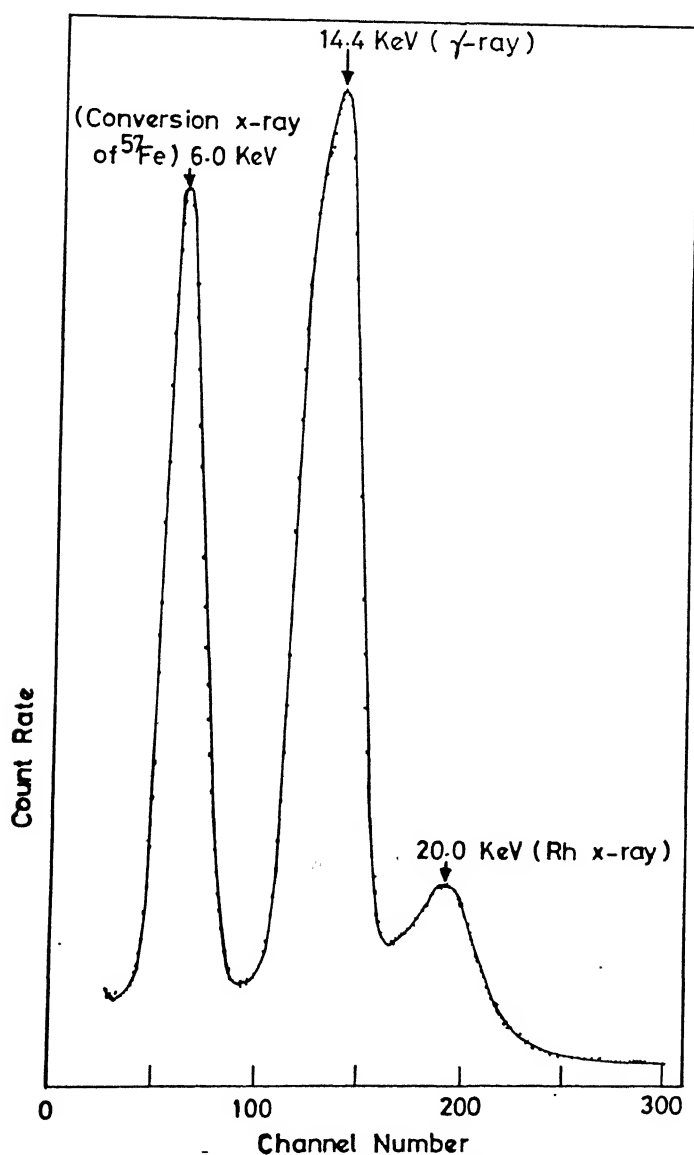


Fig. 2.5 Design of the furnace with resistance heating assembly.

A temperature controller model 457 (Indotherm, India) was used to maintain the desired temperature of the absorber with an accuracy of about ± 0.5 °C.

2.3 EXPERIMENTAL PROCEDURE

The velocity transducer, source, absorber and PC were mounted rigidly and aligned carefully on a vibration-free optical bench (see schematic diagram of Fig. 2.1). By adjusting the distance between the source and detector a well-resolved three-peak pulse height (PH) spectrum (Fig. 2.7) of the ^{57}Co in Rh was obtained. The intensity of the low-energy X-rays (6.2 keV) was suppressed by placing a thin aluminium foil between the source and the absorber. Further the lower level discriminator (LLD) and upper level discriminator (ULD) controls of the MCA were used to store the pulses whose height corresponded to the full photopeak of 14.4 keV gamma ray in the PH spectrum of the $^{57}\text{Co}/\text{Rh}$ source. In the transmission Mössbauer spectroscopy, the transmission of gamma rays through a resonant absorber is measured as a function of the relative velocity between the source and absorber. The relative velocity between the source and absorber was swept rapidly through the range of interest $-V_{\text{max}} < 0 < +V_{\text{max}}$ in both the directions by the help of a function generator which provided symmetric saw-tooth voltage waveform (reference signal) to the velocity transducer. The gamma rays transmitted through

Fig. 2.6 Decay scheme of ^{57}Co Fig. 2.7 Pulse height spectrum of ^{57}Co in Rh matrix (Mössbauer source) measured using proportional counter.

the absorber were detected by a gamma-ray detection system and were stored in the 512 channels of the MCA which was used in the multichannel scaling (MCS) mode. Synchronization of the channel number in the MCA with the velocity increment ΔV (between V and $V + \Delta V$) was achieved by advancing the address of the memory one by one through an external clock (channel advance pulses which are produced by FG), which divide the period of reference signal into 512 pulses. A start pulse which coincides with the beginning of the reference signal enabled the MCA to start with channel number 1 being advanced by the clock pulse.

Calibration of our Mössbauer spectrometer was performed with the help of standard Mössbauer absorbers whose Mössbauer parameters are well known. The peak positions of the Mössbauer spectral lines of some standard absorbers [6] with respect to α -Fe are given below (at room temperature, 293 K).

- (a) Sodium nitroprusside (SNP), $\text{Na}_2[\text{Fe}(\text{CN})_5\text{NO}]2\text{H}_2\text{O}$:
 -1.111 and $+0.592 \text{ mm s}^{-1}$
- (b) α -Fe (natural iron absorber) :
 $-5.328, -3.083, -0.838, +0.838, +3.083$ and $+5.328 \text{ mm s}^{-1}$
- (c) $\alpha\text{-Fe}_2\text{O}_3$: $-7.990, -4.470, -0.955, +1.675, +5.190$ and $+8.710 \text{ mm s}^{-1}$

The Mössbauer spectrum measured by us with α -Fe as an absorber yielded the following parameters :

- i) Centroid position : 127.55 Ch.

- (ii) Difference in the positions of the three centroids obtained from the 3 pairs of the 6-line spectrum : ± 0.05 Ch.
- (iii) Stability of the position of the centroid for over a month = ± 0.1 Ch.
- (iv) FWHM of inner lines 0.22 ± 0.01 and 0.23 ± 0.01 mm sec⁻¹.

2.4 OPTIMIZATION OF THE ABSORBER THICKNESS

Mössbauer spectrum is essentially a gamma-ray resonant absorption spectrum. It is, therefore, desirable that sufficient number of resonant nuclei (e.g. ⁵⁷Fe) should be present in the transmission path of gamma-ray photons. The intensity of the absorption line is given [7] by

$$N-N(t,v) = fN[1-\exp(-t/2) J_0(i t_{1/2})] \quad (2.1)$$

where t = thickness of the absorber,

106279

J_0 = zeroth order Bessel function

N = number of gamma-ray photons incident on the absorber.

f = recoil free fraction.

$N(t,V)$ = number of gamma-ray photons transmitted through an absorber of thickness t at a resonant velocity V .

It is seen from the above relation that the intensity of the absorption line will increase with the absorber thickness t . However for an absorber of given composition any

increase in the absorber thickness t is accompanied by the absorption of the incoming gamma-ray photons which is induced by the photoelectric effect. As a result the relative statistical accuracy

$\Delta r_{el} = [N(t, \nu)/N]^{-1/2}$ decreases exponentially with increase in thickness t .

The absorption of gamma-ray photons induced by photoelectric effect and originating from the shell (orbital) electrons of the atoms of the absorber is given by

$$\frac{N(t, \nu)}{N} = \exp\left[-\frac{t \bar{\mu} M}{f N_A \sigma_o \beta}\right] \quad (2.2)$$

where N_A = Avogadro's number

β = relative abundance of the Mössbauer atom

$\bar{\mu} = \frac{1}{M} \sum_i \mu_i M_i$ and

M_i = atomic weight of the i th atom in a molecule of mass M

μ_i = the absorption coefficient of the atom i for the Mössbauer gamma-ray photon of energy E .

In addition to the increase in the photoelectric absorption, there will be an increase in the linewidth (Γ) of the spectral line since $\Gamma = 2\Gamma_{nat} (1 + 0.135 t)$. As a result the resolution will decrease with the absorber thickness. It is thus seen that any increase in the layer thickness of the absorber leads to effects which work in opposite directions. There is, therefore, a need to settle for an

optimum layer thickness t of the absorber for obtaining a Mössbauer spectrum having best possible quality in a given time of measurement. In above the term 'quality' of the spectrum, stands for the ratio of the intensity $[N-N(t,v)]$ of the spectrum to the statistical error of the background counts, or the so-called signal to noise ratio.

A number of methods have been developed to determine this optimum layer thickness t for a single line absorber. Shimony [8] proposed a condition for maximising the intensity of the spectrum. Blamey [9] maximised the area of single line Mössbauer spectrum.

To find out the optimal layer thickness t , however one can also optimise the function $g(t)$ (instead of maximising the intensity or area of the spectral line) where

$$\begin{aligned}
 g(t) &= \frac{N - N(t,v)\sqrt{N(t,v)/N}}{2\Gamma_{\text{nat}}(1 + 0.135 t)} \\
 &= \frac{[1 - e^{-t/2} J_0(i t/2)] \exp[-t\bar{\mu}_M/2fN_A\sigma_o B]}{2\Gamma_{\text{nat}}(1 + 0.135 t)} \quad (2.3)
 \end{aligned}$$

One can plot $g(t)$ as a function of t and determine the optimal absorber thickness t from the plotted curve.

Above formula has been derived for a single-line absorber. In the case of an absorber which give many lines and which is made up of powder, we have determined the optimum thickness of the absorber on the basis of trial and error. We found that generally an amount of powdered sample of 30 - 50 mg spread over an absorber size of 1.0 cm

diameter was good enough to obtain a Mössbauer spectrum of good quality.

2.5 GEOMETRICAL EFFECTS

The geometrical arrangement of the source, absorber and detector includes various factors like the alignment of the source, absorber and detector, distance between them, finite size of the source and the detector window etc. and ^{how} it influences the shape of the Mössbauer spectral lines. Two important geometrical effects which influence Mössbauer effect significantly are

- (i) the source detector distance variation effect and
- (ii) the cosine effect. We shall now discuss these two effects in some detail.

2.5.1 Source-Detector Distance Variation Effect

If the relative velocity between the source and absorber is arranged in such a way that the source moves to and fro about its mean position and the absorber is kept at rest, the distance between the source and detector changes periodically during one cycle of motion. The counting rate or the number of gamma-ray photons received by the detector per second is directly proportional to the solid angle subtended by the source at the detector window. The counting rate, therefore, changes continuously and periodically as the source moves towards and away from the detector. As a consequence the baseline of the

Mössbauer spectrum shows a non-flat behaviour. In our experiment, we eliminated this kind of geometrical effect by folding the two Mössbauer spectra observed in the MCA (these two Mössbauer spectra are a consequence of the symmetric nature of the saw-tooth waveform of the signal fed to the Mössbauer drive). This type of effect can also be eliminated if the source is kept at rest and the absorber is allowed to move. The maximum displacement of the source from its mean position can be made smaller if the frequency of the reference signal is 20 to 30 Hz thus reducing the effect.

2.5.2 Cosine Effect

This effect arises out of the finite size of the source, absorber and detector window. Some of the gamma-ray photons emitted from the source travel at an angle θ with the direction of the relative velocity. These gamma-ray photons, which are emitted along directions other than the direction of the relative motion will have a Doppler energy shift $\Delta E = E_0(V/C) \cos \theta$ and they will be received by the absorber and later on by the detector window because of their finite sizes. As a result the Mössbauer spectral line becomes broader and shows a shift. In our experiment we minimised this effect by collimating the gamma-ray photon beam (by restricting it along the direction of relative motion) and by optimising the distance between the source and absorber.

2.6 DATA ANALYSIS

In all forms of spectroscopy it is desirable to find out precisely the peak positions, line-widths and the areas under the spectral lines. In order to obtain the most precise estimates of the peak parameters in Mössbauer spectroscopy it is essential to analyze the spectra with the help of digital computer. In Mössbauer spectroscopy the spectrum output is available in digital form. It has been shown by Margulies and Ehrman [10] that for a source and absorber having low effective layer thickness, the lines of the transmission spectrum have the shape of a Lorentzian curve and to a good approximation are additive. Taking above properties into account several computer programs have been developed by several authors. In our analysis we used a computer program based on the method developed by Law and Bailey [11]. Our program proceeded by finding the folding point of the two symmetric Mössbauer spectra and the values of the adjustable parameters (initial guess value of the peak parameters) to obtain closest agreement between the experimental data and the value predicted by the assumed function [12].

Let the function $\phi_i = \phi_i(B_1, B_2, \dots, B_n)$ be the functional form corresponding to the experimental data points Y_i . The following function S^2 , when set to a minimum, yields a set of adjustable parameters B_k :

$$S^2 = \sum_{i=1}^N S_i^2 = \sum_{i=1}^N (Y_i - \phi_i)^2 \quad (2.4)$$

$$\frac{dS^2}{dB_k} = 0 \quad (2.5)$$

Above condition leads to N simultaneous equations. These simultaneous equations are solved to obtain a correction ΔB_k in the approximate value B_k . The new parameters

$$B_k^{i+1} = B_k^i + \Delta B_k$$

are then selected for the (i+1)th iteration. These new parameters are then examined to ensure that S^2 approaches a minimum value. These iterations are continued until a minimum specified limit is reached. The goodness of fit was tested at each stage by calculating the χ^2 - values. In the analysis of our Mössbauer spectra we achieved χ^2 - values in the range 0.9 - 7.8. The standard error in the fitted parameter, B_k , was also calculated with the help of inversion matrix [13].

2.6.1 Hyperfine Field Distribution

In the case of absorbers having amorphous nature, the broadening of the Mössbauer spectral lines arises from the distribution of hyperfine fields (either the distribution of the EFG's or the distribution of the H_{int}). A number of methods have been developed to determine the distribution of the hyperfine fields from the broadening

of the Mössbauer spectra. In our analysis we have used Window's [14] method as outlined below.

Let us denote by $P(H)$ the hyperfine field distribution. The ^{57}Fe Mossbauer spectrum can then be defined as

$$Y(E) = \sum_{i=1}^N \int \frac{A_i P(H) dH}{1 + 4[(E - E_0)/W]^2} \quad (2.6)$$

where

A_i = intensity of the i th peak

W = FWHM

$E_0 = V_{ZZ}$, the principal component of the EFG distribution or $a_i(H)$, the position of the peak for the magnetic field distribution.

The values for a_i are given [15] as

$$a_6 = -a_1 = 16.15 \times 10^{-3} \text{ mm/kOe}$$

$$a_5 = -a_2 = 9.34 \times 10^{-3} \text{ mm/kOe}$$

$$a_4 = -a_3 = 2.54 \times 10^{-3} \text{ mm/kOe}$$

The $P(H)$ is expressed in terms of the Fourier series

$$P(H) = \sum_{n=1}^M b_n \left[\cos \frac{n\pi H}{H_{\max}} - (-1)^n \right] \quad (2.7)$$

M = Number of Fourier coefficients.

With the condition

$$\left[\frac{dP(H)}{dH} \right]_{H=H_{\min}} = 0 = \left[\frac{dP(H)}{dH} \right]_{H=H_{\max}} \quad (2.8)$$

The value of H_{\max} is chosen such that $P(H_{\max}) = 0$. The Fourier coefficient b_n were calculated with the help of computer program which was based on a least-squares-fit

to the experimental data. Generally the value of M was chosen to be between $n = 20$ and $n = 25$. The computer program for determining the distribution of hyperfine fields was tested by analyzing the spectra for the standard samples of α -Fe and sodium nitroprusside (Fig. 2.7, 2.8).

The average value of hyperfine field was calculated using the expression

$$\bar{H} = \sum_{i=1}^n P_i(H_i) H_i$$

or

$$\Delta E = V_{zz} = \sum_{i=1}^n P_i(V_i) V_i.$$

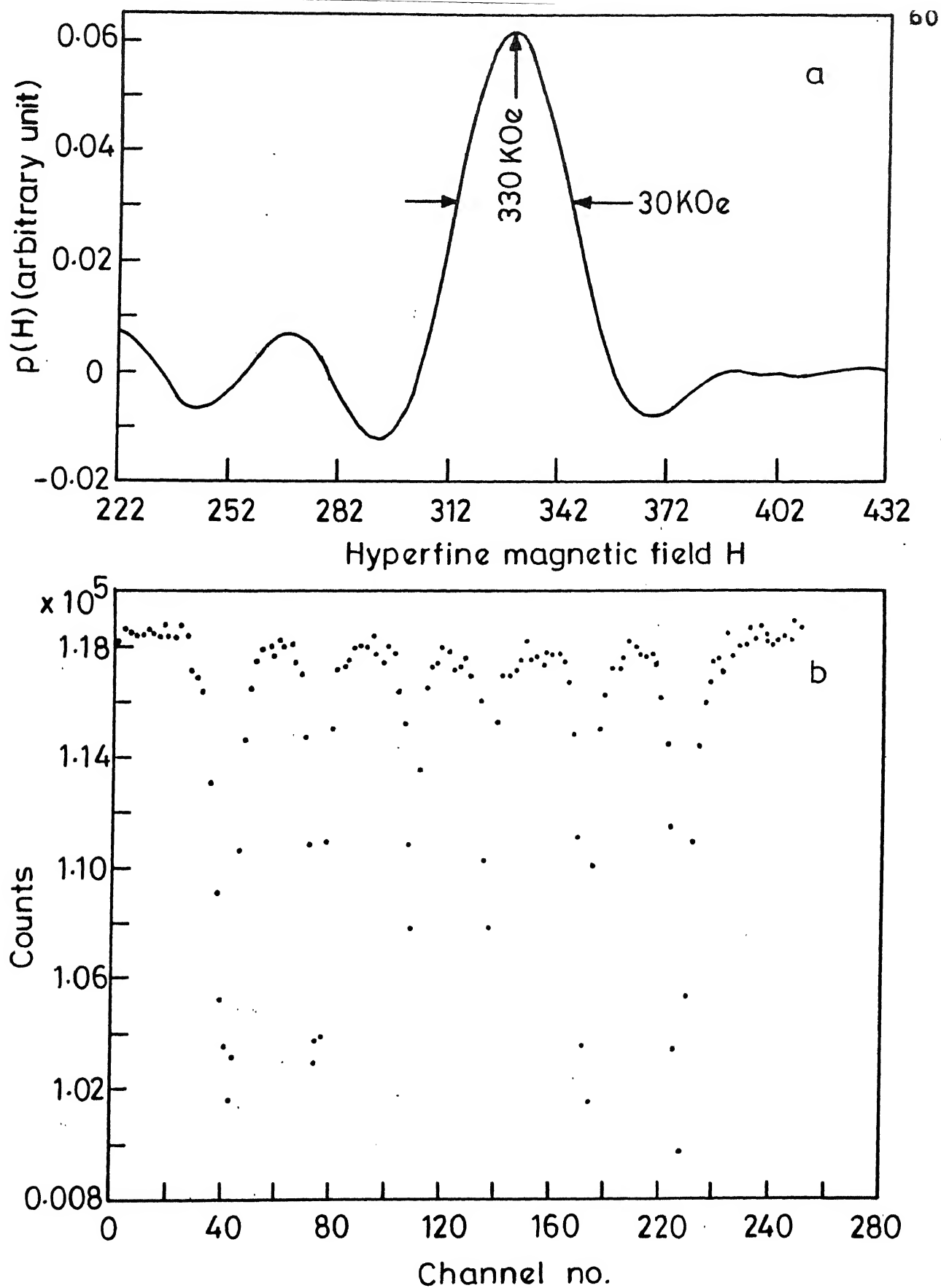


Fig.2.8 Hyperfine field distribution for α -Fe (absorber) at room temperature. The top figure shows the $p(H)$ distribution while the bottom figure shows the corresponding Mössbauer spectrum of α -Fe.

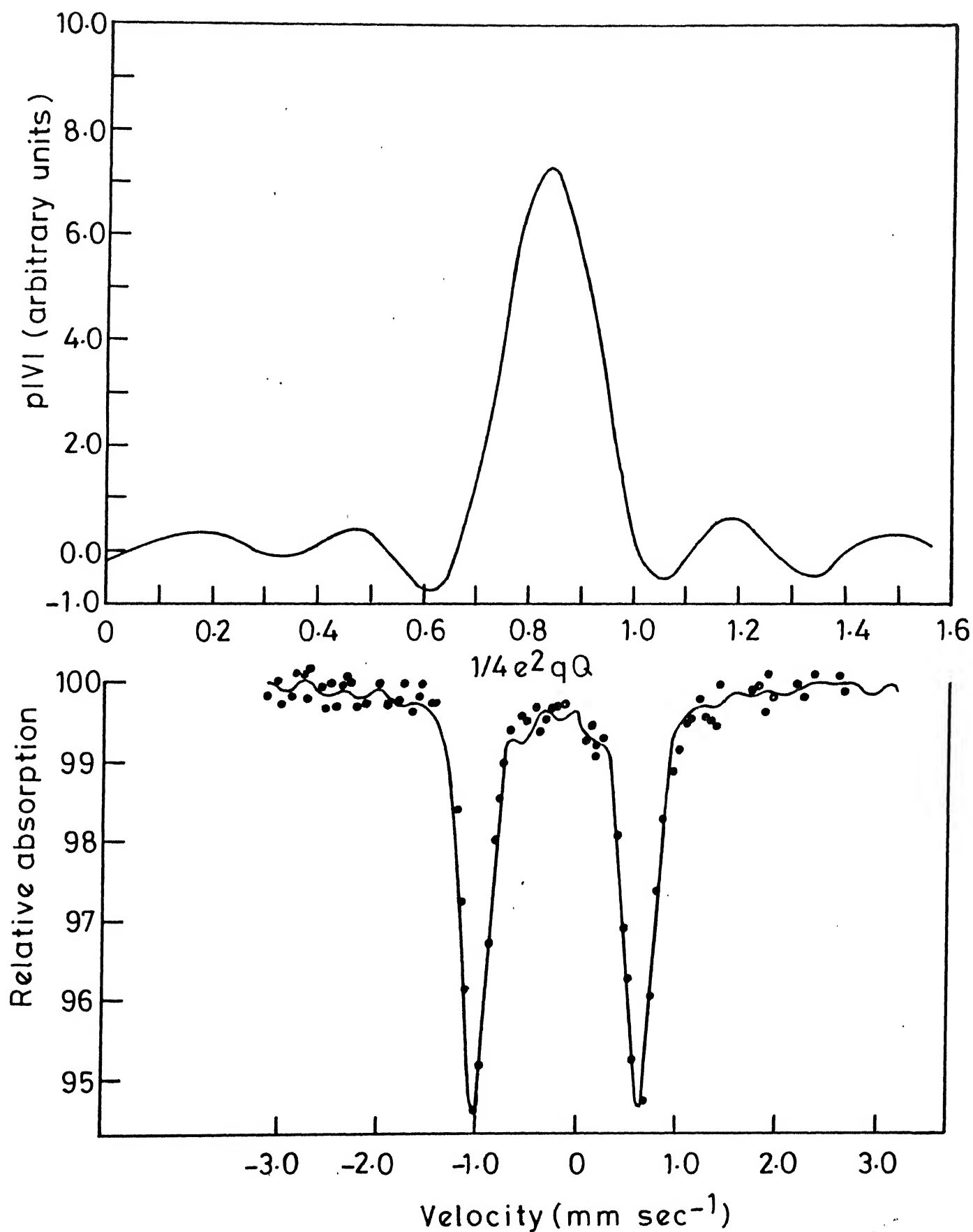


Fig.2.9 EFG distribution in sodium nitroprusside (absorber) at room temperature. The top figure shows the (pIV) distribution while the bottom figure shows the fitted Mössbauer spectrum

REFERENCES

1. G.K. Shenoy and F.E. Wagner, (Eds.), 'Mössbauer Isomer Shift' (North-Holland Publishing Company, Amsterdam, 1978).
2. 'Mössbauer Spectroscopy and Its Applications'
Proceedings of a Panel, Vienna, 24-28 May 1971
(International Atomic Energy Agency, Vienna, 1972).
3. A.K. Gupta, K.R. Sarma, J.J. Huntzicker and G.N. Rao,
Rev. Sci. Instrum. 45, 1423 (1974).
4. P.W. Nicholson, 'Nuclear Electronics' (John Wiley
and Sons, New York, 1979).
5. G.F. Knoll, 'Radiation Detection and Measurement'
(John Wiley and Sons, New York, 1979).
6. A. Vertes, L. Korecz and K. Burger (Eds.), 'Mössbauer
Spectroscopy' (Elsevier Scientific Publishing Company,
New York, 1979).
7. R.M. Housley, N.E. Brickson and J.G. Dash, Nucl. Instr.
and Methods 27, 29 (1964).
8. U. Shimony, Nucl. Instr. and Methods 37, 348 (1965).
9. P.J. Blamey, Nucl. Instr. and Methods 142, 553 (1977).
10. S. Margulies and J.R. Ehrman, Nucl. Instr. and Methods
12, 131 (1961).
11. V.J. Law and R.V. Bailey, Chem. Eng. Sci. 18, 189 (1963).
12. H.C. Verma, Ph.D. Thesis, Indian Institute of Technology,
Kanpur, India (1980), (Unpublished).

13. J.R. Wolberg, ''Prediction Analysis'' (D. Van Nostrand Company Inc., Princeton, 1967).
14. B. Window, J. Physics E4, 401 (1971).
15. C.L. Chien, Phys. Rev. B18, 1003 (1978).

CHAPTER 3

MÖSSBAUER AND OTHER STUDIES OF SOME GLASS-CERAMIC SYSTEMS CONTAINING MAGNETIC PHASES

3.1 INTRODUCTION

Glass ceramics are new inorganic materials of immense technological significance and future promise. The importance of the glass ceramics can be underlined by the fact that these materials possess an extremely favourable combination of mechanical, thermal, chemical, electrical and physical properties. Several possible areas for the practical applications of the glass ceramics are known at the present time. In the literature books [1,2] and several papers [3-8] are available which provide an introduction to glass ceramics and explain the need to study these materials in greater detail. The method of production leads to zero porosity and an outstanding uniformity of properties in the finished ceramic. These properties arise from the molten state and the nature of nucleation process. The factors that influence the final properties of a glass ceramic and which can be controlled are listed below.

- (i) Properties of crystalline phases :- In the case of glass ceramics, as compared to the traditional ceramics, the intrinsic properties of the crystal

will have a major effect on the final properties of the resulting artefact and the role of the texture will be less dominant.

- (ii) Grain size :- This property affects the final mechanical, magnetic and electrical properties of the product.
- (iii) Intergranular bonding :- This property affects the final strength and appearance of the product.
- (iv) Crystal orientation :- In case of magnetic material crystal orientation affects the magnetic anisotropic property and coercive force (magnitude of coercive field).
- (v) Percentage crystallinity and distribution of any remaining glassy phase :- Although glass ceramics should be 100% crystalline, this is not always possible and indeed for some applications it is desirable to have a residual glassy phase.

The above factors can be influenced by controlling the following (a) base composition (b) the choice of nucleant and (c) the heat treatment.

A glass ceramic is initially a glass in which first the formation of nuclei is enhanced and subsequently the crystallization (devitrification) occurs when the glass is subjected to the controlled heat-treatment schedule. The nucleation in the glass ceramic can be enhanced either by the addition of a nucleating agent or by using a special

base composition which is self-nucleating. The process of production of glass ceramic, therefore, involves a two-stage heating cycle in order to develop a suitable crystalline texture. In the first stage of heating, the formation of stable nuclei occurs while in the second stage of heating the growth of crystal (growth of nuclei and formation of crystals) takes place. The crystal growth is of course dependent on the viscosity of the glass and on the temperature through the base composition of glass.

Let us denote by T_1 and $T_1 + \Delta T$ the limits of the range of temperatures of the first stage of heating and by T_2 and $T_2 + \Delta T$ the corresponding limits of the range of temperatures of the second stage of heating. If these two temperature ranges (T_1 to $T_1 + \Delta T$ and T_2 to $T_2 + \Delta T$) are almost same, little control is possible over the crystallization of resulting glass ceramic. The reason for this is that as soon as nucleus forms it starts growing and as a result few large crystals would be produced. However if the two temperature ranges can be separated, the processes of nucleation and growth can also be separated. This happens in the following manner. The only process occurring between the temperatures T_1 and $T_1 + \Delta T$ is the formation of nuclei and then by maintaining any temperature between T_1 and $T_1 + \Delta T$ it is possible to control the number of nuclei. When sufficient number of nuclei have been produced, the temperature is quickly altered to one between T_2 and $T_2 + \Delta T$

which promotes rapid growth of the crystals. This explains how the percentage of crystallinity and grain size are controlled. The processes of both nucleation and growth are activated and therefore temperature-controlled. However this implies that the practical results will depend on both the temperature and the time spent at that temperature.

There is considerable scientific and technological interest attached to glass ceramics [1,2]. The scientific interest stems primarily from the fact that the study and development of glass ceramics are intimately connected to the studies of nucleation and crystallization of supercooled liquids and hence their study throws additional light on these basic processes. Secondly the composition of glass ceramics can be varied over a wide range and as a result nucleation and crystallization processes can be studied over a wide range. Glass ceramics can be produced to possess very fine microstructure and can also contain a wide variety of crystal types. This allows glass ceramic as a medium to investigate mechanical strength and fracture processes in brittle solids. Similarly other physical properties can be investigated through the study of glass ceramics.

Glass ceramics have stimulated considerable interest in various technological fields [1-2]. They assume importance in materials technology in view of the novel, excellent and wideranging combination of physical properties offered by them. They invoke considerable interest in the field of

glass technology. Glass ceramics provide special interest in the area of conventional ceramics because one can study the relationship between crystallographic constitution and physical properties. Crystal phases present in the glass ceramics can be varied in a controlled manner to prepare materials having identical chemical compositions but different crystallographic compositions. In view of the fact that the vitreous phase assumes an important role in determining certain properties of the ceramics, the problem of studying the effects of variations in the proportion and chemical compositions of the vitreous phase in the glass ceramics provides challenging interest. Glass ceramics are also of interest to mineralogists.

In the present chapter we shall describe the results of our experimental studies of those glass ceramics in which magnetic phases can be precipitated. Our studies consisted mainly of Mössbauer spectroscopic measurements and we have used experimental data obtained by recording X-ray, EPR and optical spectra and magnetization curves to aid the interpretation of our results. The systems studied by us include different base glasses containing silica-based substituted yttrium iron garnet (YIG), barium ferrite, strontium ferrite and lead ferrite. These systems can be divided into two types. The first type includes silica-based substituted yttrium iron garnet (YIG) in which external nucleating agents (viz. Bi_2O_3 , $\text{Ag}_2\text{O}+\text{As}_2\text{O}_3$ and Pd)

were added in the base glass and magnetic phases were precipitated during a controlled heat treatment. The second category included different compositions of the base glass which were self-nucleating and involved precipitation of the magnetic phases of different ferrites (barium ferrite, strontium ferrite and lead ferrite) under controlled heat treatment.

3.2 STUDY OF YTTRIUM IRON GARNET (YIG) SYSTEMS

3.2.1 Introduction

We shall first describe our studies of yttrium iron garnet (YIG) systems. In view of their interesting electrical and magnetic properties, the magnetic phase of yttrium iron garnet (YIG) has been studied extensively [9,10]. Several technological applications of YIG are known [10] and some of these are :

- i) tunable filters, circulators and gyrators in the microwave region.
- ii) magnetic bubble domain-type digital memory devices
- iii) magneto-optical device
- iv) acoustic devices.

In each of these applications one needs YIG having specific properties. The method of preparation of the YIG determines its properties. Nowadays there are available several methods of preparation of YIG and these are :

(i) melt quenching [11], (ii) spray pyrolysis [12], (iii) dc or rf sputtering [13,14], (iv) freeze drying [15], (v) amorphous citrate gel process [16,17] and (vi) glass ceramic method [6]. Among all these methods the glass ceramic method has a distinct advantage and we have used this method for preparing our samples.

3.2.2 Experimental Method

3.2.2.1 Sample preparation

Our samples consisted of YIG precipitated in four different glasses. The composition of each of these four glasses is given in Table 3.1 where the four compositions are labelled as C1, C2, C3 and C4. The composition C1 and C2 contain Bi_2O_3 as the nucleating agent. In the compositions C3 and C4 the nucleating agents are $(\text{Ag}_2\text{O} + \text{As}_2\text{O}_3)$ and Pd respectively. The glasses were prepared from reagent grade chemicals by melting the mixture in alumina crucible in electrically heated furnace between 1300 to 1450 °C. Glass plates were cast by pouring the melt on the aluminium mould. In the case of the glass (composition C4) containing Pd, we added 0.05wt% of Pd through a complex salt $\text{Pd}(\text{PY})_2(\text{SCN})_2$. The nucleation and crystal growth temperatures were estimated with the help of differential thermal analysis (DTA). In Table 3.2 we have described the different heat treatments (based on the DTA results) given by us to different samples which are also labelled with a code.

Table 3.1 : Composition of the glasses investigated with different nucleating agents.

Glass Code Compound	Composition (wt%)			
	C1	C2	C3	C4
SiO ₂	48	49.6	48	48
Na ₂ O	26	33.6	26	26
Y ₂ O ₃	9	5.9	9	9
Fe ₂ O ₃	15	10.1	16	17
Bi ₂ O ₃	2	0.8	-	-
Ag ₂ O	-	-	0.5	-
As ₂ O ₃	-	-	0.5	-

In C4 0.05 wt% of palladium is added through the complex salt Pd(PY)₂(SCN)₂.

Table 3.2 : Sample labels and details of heat treatment given to different glass compositions (Heat-treatment is described in terms of temperature/period) with X-rays and Magnetization data.

Glass	Heat treatment	Sample Label	Crystalline phases as assigned from the X-ray data. Relative intensity is shown in parantheses very weak (VW) weak (W) Strong (S)[18]	Magnetization M_s (emu g ⁻¹) [18]
C1	As prepared	C10	-	-
	1015k/2h+			
	1055k/24h	C11	Fe ₂ O ₃ (S) YIG (W)	0.3
	1015k/5h+			
	1055k/24h	C12	Fe ₂ O ₃ (W) YIG (S)	0.3
	As prepared	C20	-	-
C2	895k/2h+	C21	Fe ₂ O ₃ (S) YIG (W)	-
	990k/2h			
	895k/2h+			
	990k/24h	C22	Fe ₂ O ₃ (VW) YIG (S)	6.0
	As prepared	C30	-	-
C3	555k/2h+	C31	Fe ₂ O ₃ (S) YIG (W)	1.0
	555k/2h			
	865k/2h+	C32	Fe ₂ O ₃ (VW) YIG (S)	1.2
	905k/2h			
	1000k/2h+	C33	Fe ₂ O ₃ (VW) YIG (VS)	1.8
	1095k/2h			
	As prepared	C40	-	-
C4	1070k/2h+	C41	Fe ₂ O ₃ (W) YIG (S)	2.0
	1105k/2h			

C11: 1015k/2h + 1055k/24h indicates that the glass of composition C1 was heated at 1015k for 2 hours (nucleating temperature first stage heating) and this was followed by heating it at 1055k for 2 hours (crystallization temperature, second stage heating).

3.2.2.2 Mössbauer spectroscopic studies

The above samples were powdered and Mössbauer absorbers were prepared following the procedure described in Chapter 2. Transmission Mössbauer spectra of different sample absorbers were taken with the help of Mössbauer spectrometer (already described in Chapter 2) operated in constant acceleration mode. The spectra were recorded either at the room temperature (RT) or at liquid nitrogen (80 K) temperature and the appropriate temperature of measurement is mentioned in the following discussion. The Mössbauer spectrometer was calibrated using α -Fe foil and isomer shift (IS) was measured and reported with respect to α -Fe. Other details of the Mössbauer spectrometer, measurements and data analysis are already described in Chapter 2.

3.2.2.3 Measurement of X-ray, EPR and optical spectra and magnetization curves

To supplement our results obtained by Mössbauer spectroscopy we used data for the present samples obtained by measuring X-ray, EPR and optical spectra and magnetization curves. These other measurements were carried out by S. Ram and D. Bahadur [18] in the Advanced Centre for Materials Science of our Institute. X-ray powder diffraction patterns of the samples were recorded with a Rich and Seifert Iso-Debyeflex 2002 diffractometer. The EPR measurements were carried out in a Varian Associates Spectrometer

(Model V 4502-12) in the X-band frequency and with a 100 KHz field modulation. The optical absorption measurements in visible and UV regions were carried out on a Cary 17 D spectrophotometer in double beam operation. Magnetization measurements were carried out with a PAR vibrating sample magnetometer (model 150A) in conjunction with a Varian 9'' magnet (model V-7200).

3.2.3 Results and Discussion

The Mössbauer spectra of as-prepared sample and heat-treated samples (Table 3.1 and 3.2) C10, C11, C12, C21, C22, C41, C31, C32 and C33 are shown in Figs. 3.1a-3.1c. The spectra corresponding to samples C31, C32 and C33 are grouped together in Fig. 3.1c because these spectra are similar and these samples share the same nucleating agents ($\text{Ag}_2\text{O}+\text{As}_2\text{O}_3$). Mössbauer parameters obtained by analyzing these spectra are given in Table 3.3.

The Mössbauer spectra of all the samples, except the as-prepared sample C10, C20, C30, C40, consist of a doublet (quadrupole split) spectrum along with one or two six-line (sextet) Zeeman spectrum. The as-prepared sample C10, C20, C30, C40 shows a doublet spectrum while all other samples show, in addition to the doublet spectrum, six-line spectra arising out of the magnetic phases which are precipitated after suitable heat treatment. We shall first discuss the doublet spectra for all samples so that their systematic behaviour

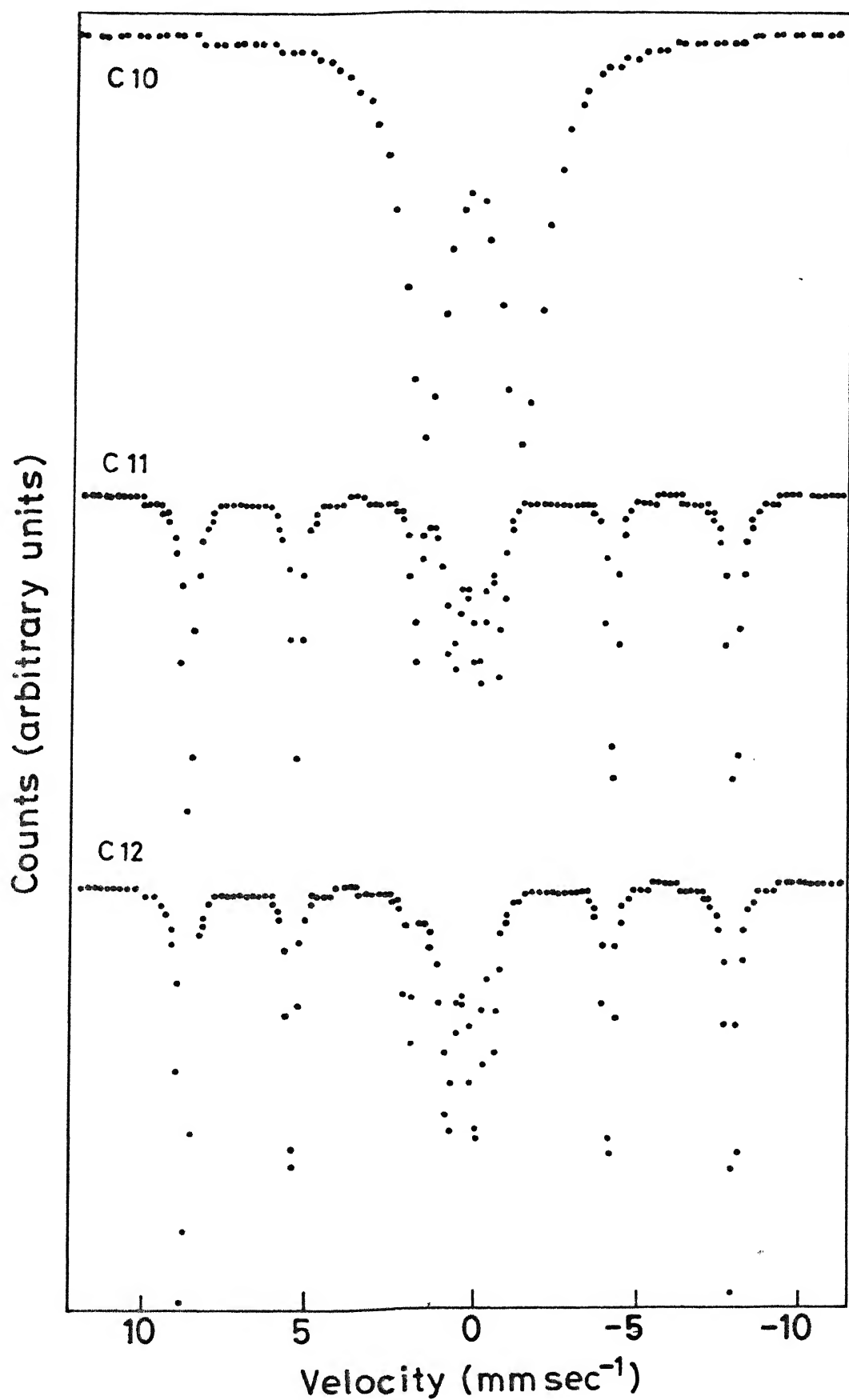


Fig. 3.1(a) Mössbauer spectra of C10, C11 and C12 at 293 K.

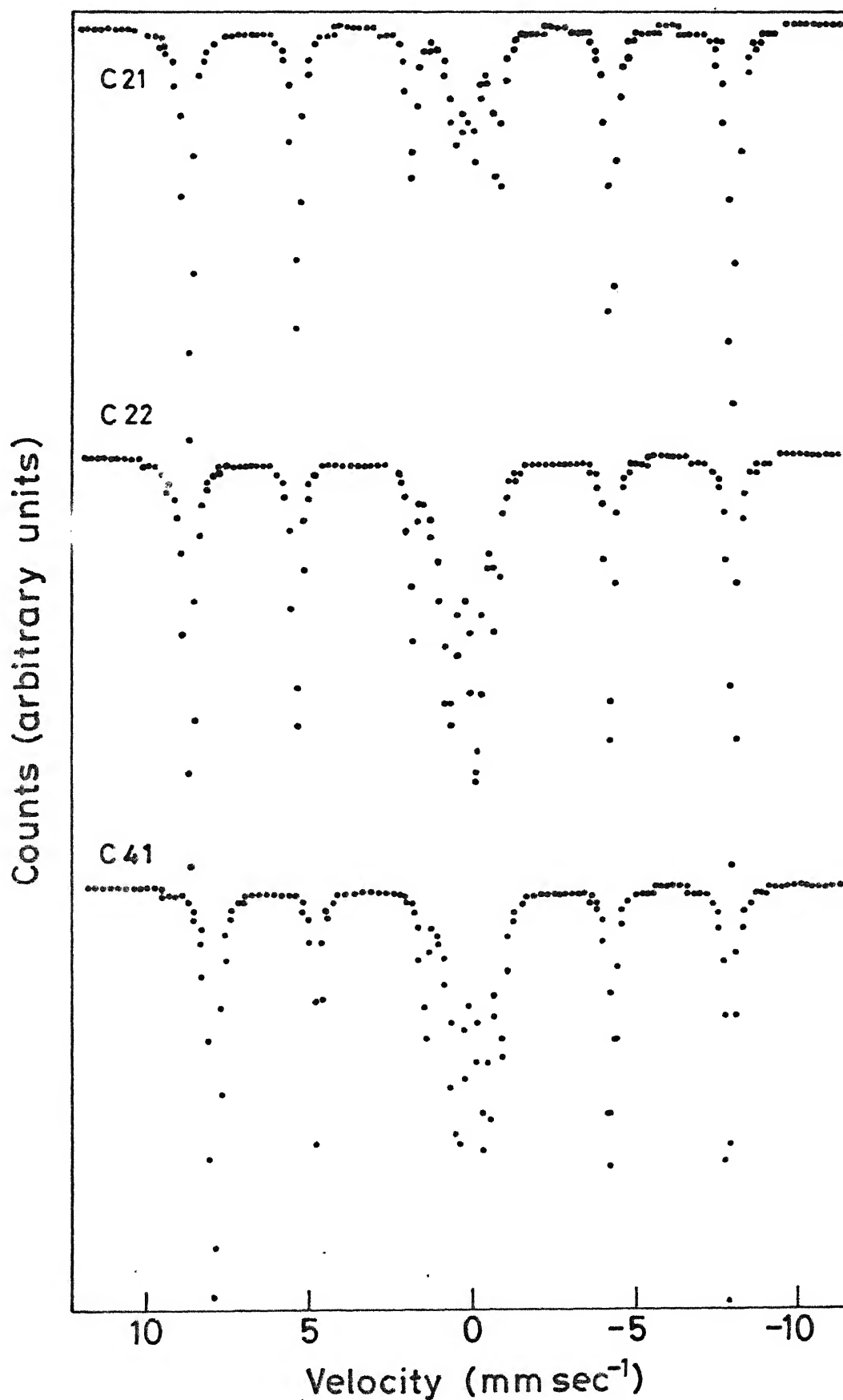


Fig. 3.1(b) Mössbauer spectra of C21, C22 and C41 at 293K.

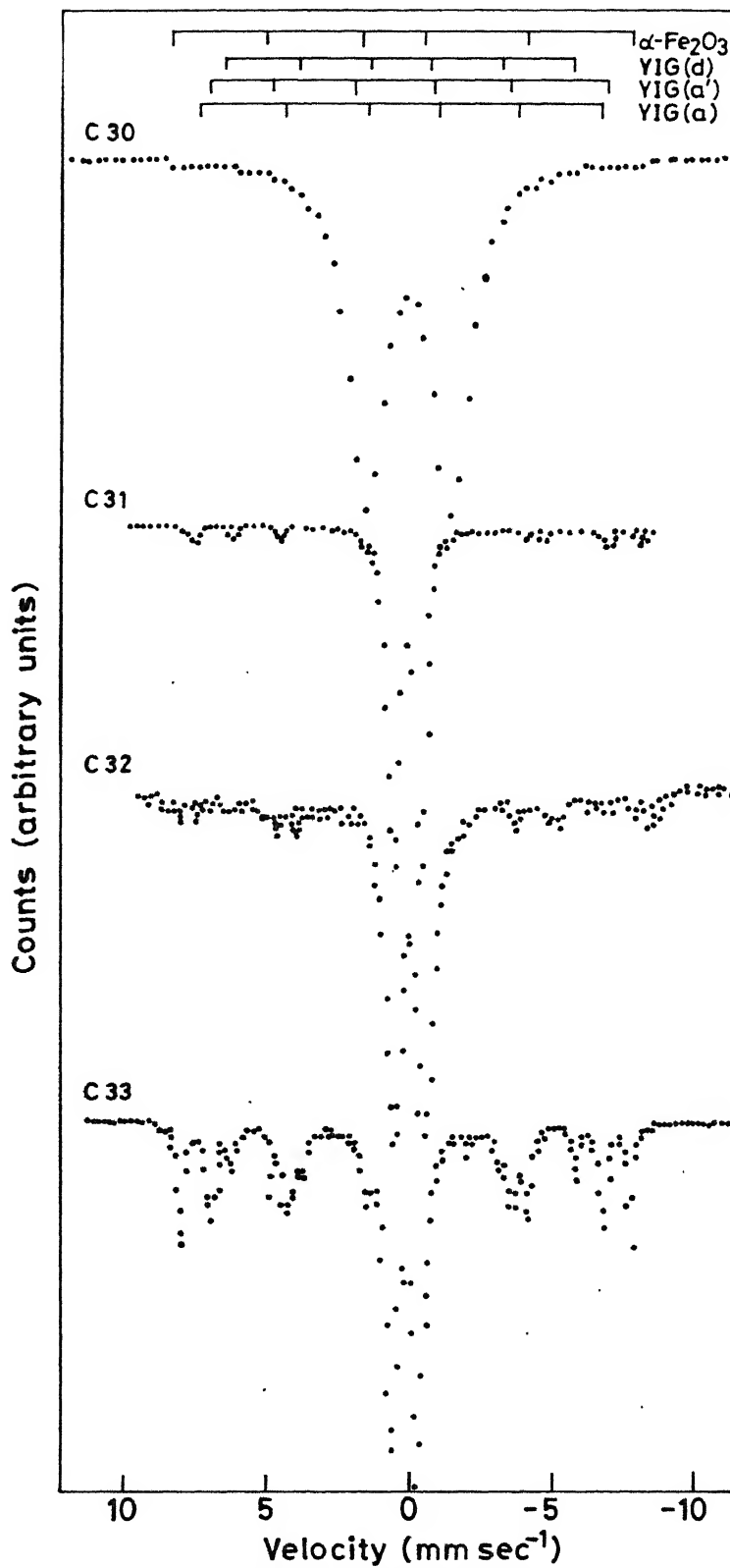


Fig. 3.1(c) Mössbauer spectra of C30, C31, C32
C33 at 293 K.

Table 3.3 : Mössbauer parameters (measured at room temperature) for samples C10, C11, C12, C20, C21, C22, C30, C31, C32, C33, C40 and C41.

Sample	Doublet Spectra			Six-line Spectra				Assignment
	IS(a)	$\Delta E(b)$	$\Gamma(c)$	IS(a)	$\Delta E(b)$	$H_{int}(d)$	$\Gamma(c)$	
C10	0.23	0.971	0.50	-	-	-	-	Glass
C11	0.24	0.782	0.48	0.36	-0.111	510 \pm 2	0.23	α -Fe ₂ O ₃
C12	0.24	0.841	0.46	0.36	-0.112	512 \pm 2	0.23	α -Fe ₂ O ₃
C20	0.23	0.971	0.50	-	-	-	-	Glass
C21	0.23	0.773	0.43	0.34	-0.104	509 \pm 2	0.23	α -Fe ₂ O ₃
C22	0.22	0.835	0.48	0.36	-0.120	512 \pm 2	0.23	α -Fe ₂ O ₃
C30	0.23	0.971	0.50	-	-	-	-	Glass
C31	0.23	0.926	0.49	-	-	-	-	-
C32	0.22	0.901	0.48	-	-	-	-	-
C33	0.23	0.791	0.46	0.36	-0.112	512 \pm 2	0.23	α -Fe ₂ O ₃
				0.37	0.00	392 \pm 2	0.32	YIG-d site
				0.38	-0.13 \pm 0.03	425 \pm 4	0.26	YIG-a' site
				0.34	0.07 \pm 0.03	431 \pm 4	0.26	YIG-a site
C40	0.23	0.971	0.50	-	-	-	-	Glass
C41	0.22	0.852	0.49	0.38	-0.098	515 \pm 2	0.23	α -Fe ₂ O ₃

- (a) IS = Isomer shift, values in mm s⁻¹ with respect to α -Fe :
Typical error is ± 0.01 mm s⁻¹. room temperature
- (b) ΔE = Electric quadrupole splitting in mm s⁻¹ : Typical error is 0.005 mm s⁻¹.
- (c) Γ (FWHM) = width of the spectral line, values in mm s⁻¹ :
Typical error is 0.01 mm s⁻¹.
- (d) H_{int} = Internal magnetic field at ⁵⁷Fe nucleus: in units of kOe.

is understood more clearly. The Mössbauer spectra of as-prepared samples C10, C20, C30 and C40 are same (Table 3.3) and hence in Fig. 3.1(a) only the spectrum of the sample C10 is shown. Mössbauer spectrum of the as-prepared sample yields an isomer shift $IS = 0.23 \pm 0.01 \text{ mm s}^{-1}$ and a quadrupole splitting $\Delta E = 0.971 \pm 0.005 \text{ mm s}^{-1}$. The observed value of the IS indicates that the iron ion in this glass is in the high spin state Fe^{3+} with tetrahedral coordination [19, 20]. The large value for ΔE , as well the large line-width Γ (FWHM) $= 0.50 \pm 0.01 \text{ mm s}^{-1}$ of the lines, indicate that there are a large number of "non-identical" sites and larger departures from cubic symmetry in glasses than in crystals. The Mössbauer parameters of the sodium silicate quenched glass observed by us agree well with the values reported by several other workers [19-21].

Before we examine the effect of composition and nucleating agent on the crystallization of the magnetic phases, we wish to discuss the results corresponding to the doublet spectrum for the series of samples C30, C31, C32 and C33 (Table 3.2). These four samples consist of the same nucleating agent ($Ag_2O + As_2O$) and they were subjected to heat-treatment involving three different schedules. The Mössbauer spectrum of as-prepared sample C30 yields the values of $IS = 0.23 \text{ mm s}^{-1}$, $\Gamma = 0.50 \text{ mm s}^{-1}$ and $\Delta E = 0.971 \text{ mm s}^{-1}$. However the Mössbauer spectra of the heat-treated samples C31, C32 and C33 (Fig. 3.1c) are observed to be more complex than for C30.

In addition to the doublet spectra which is attributed to the glassy phase, other lines appear and they are attributed to the other magnetic phases (e.g. α -Fe₂O₃ and Si-substituted YIG) that have crystallised after the heat treatment. Mössbauer parameters for the doublet spectra indicate that the doublet spectra are due to paramagnetic Fe³⁺ in the glassy state. As the magnetic phases are being crystallised, the IS values for the doublet spectra remain essentially unchanged but the ΔE values decrease from 0.971 (C30) to 0.791 (C33). Constancy of IS implies that the s -electron density at the ⁵⁷Fe nucleus does not change and hence the bond characteristics of Fe³⁺ and O²⁻ does not change as the magnetic phases are being precipitated. Observed decrease in ΔE , on the other hand, indicates that the distortion in the Fe³⁺-O₄²⁻ tetrahedron decreases with the precipitation of the magnetic phases. This observed behaviour of IS and ΔE for the doublet spectra suggests that these spectra consist of several overlapping and unresolved subspectra arising out of the random variation of electric field gradient (EFG) V_{zz} from site to site.

In order to examine this variation of the EFG we have analyzed our data with the help of the Fourier series method developed by Window [22,23]. This method has been described in Sec. 2.6.1 and it has been used widely in the literature to determine hyperfine field distributions in

magnetic systems having amorphous nature. The probability distribution, $P(V)$, for the EFG V_{zz} (and hence for $\Delta E = eQV_{zz}/2$) corresponding to the doublet spectra for C30, C31, C32 and C33 are shown in Fig. 3.2. The numerical values for various parameters related to the $P(V)$ distributions are given in Table 3.4. It is observed from Fig. 3.2 that the $P(V)$ distribution becomes narrower and the peak position shifts to lower values of ΔE as we go from the sample C30 to C33. Although the values of ΔE obtained from the $P(V)$ distributions (Table 3.4) do not agree with those obtained by least-square-fit of the spectra (Table 3.3), the general trend of ΔE decreasing with heat treatment is evident in both the cases. Starting from the as-prepared sample (C30), the FWHM of the $P(V)$ distributions decreases by a factor of 2 for the sample (C33). This behaviour is understood as an effect of decreasing disorder in the glasses as they are heated. Precipitation of crystalline phases reduce the distortion in the FeO_4 tetrahedron in glasses and this results in the behaviour seen in Fig. 3.2 and Table 3.4.

Upon examining the values of IS and ΔE for the samples C10, C11 and C12 (Table 3.3) we note that starting from the as-prepared sample C10, the value of ΔE first decreases from C10 to C11 and again increases from C11 to C12. In fact the distribution curve, $P(V)$, for C11

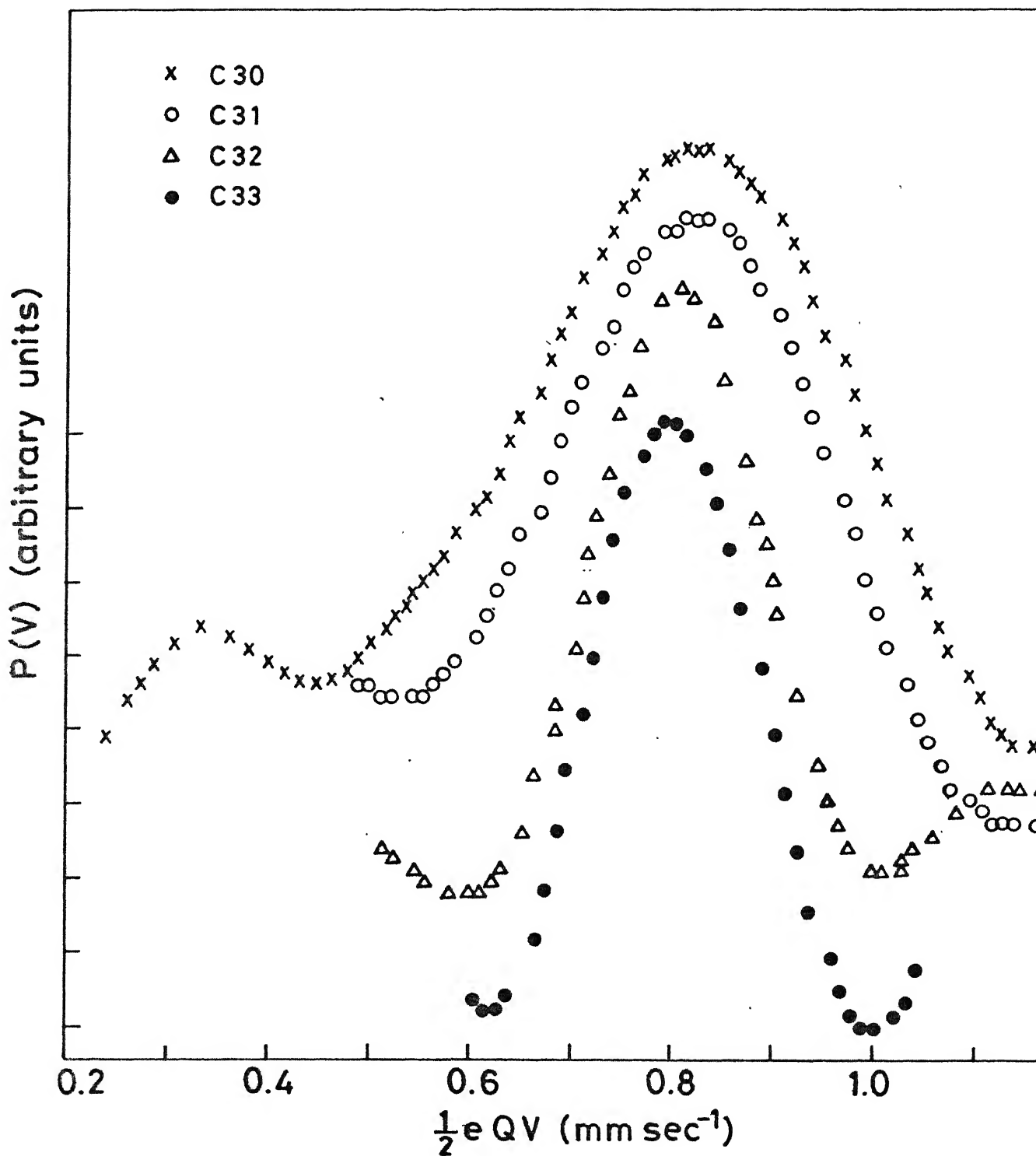


Fig. 3.2 Distribution of the electric field gradient $P(V)$ at ^{57}Fe nuclei in C30, C31, C32 and C33.

Table 3.4 : Different parameters related to the P(V) distributions obtained for the four sample C30, C31, C32 and C33.

Sample	Mean $\overline{\Delta E}$ $\overline{\Delta E} = \sum_i P_i(V_i)V_i$ (mm s ⁻¹)	FWHM of the P(V) distribu- tions (mm s ⁻¹)	Number of Fourier coeffici- ents used	χ^2 -value
C30	0.83	0.38	25	4.8
C31	0.82	0.31	20	2.9
C32	0.80	0.20	20	2.2
C33	0.79	0.19	25	2.6

Table 3.5 : Different parameters related in the P(V) distributions obtained for samples C11 and C12.

Sample	Mean value $\overline{\Delta E}$ $\overline{\Delta E} = \sum_i P_i(V_i)V_i$ mm s ⁻¹	FWHM of the P(V) distribu- tion mm s ⁻¹	Number of Fourier Coefficient used	χ^2
C11	0.31	0.23	20	2.9
	0.67	0.25		
C12	0.27	0.20	20	3.2
	0.72	0.19		

(Fig. 3.3) yields two values of ΔE (Table 3.5). The smaller value of $\overline{\Delta E}$ ($= 0.31 \text{ mm s}^{-1}$) is assigned to the quadrupole split doublet corresponding to the fine particles of $\gamma\text{-Fe}_2\text{O}_3$. It is possible that some amount of YFeO_3 is also present. The larger value of $\overline{\Delta E}$ ($= 0.67 \text{ mm s}^{-1}$) corresponds to the $^{57}\text{Fe}^{3+}$ in the glassy state. The fine particles of $\gamma\text{-Fe}_2\text{O}_3$ and YFeO_3 are both known to yield quadrupole-split Mössbauer spectrum because of superparamagnetism [24]. Further the presence of $\gamma\text{-Fe}_2\text{O}_3$ in C11 is confirmed by the Mössbauer spectrum of sample C11 observed at 80 K (Fig. 3.4 and Table 3.6).

The nucleation time is increased from 2 to 5 hours while going from the sample C11 to C12 and this has caused the value of ΔE to increase from 0.782 (C11) to 0.841 (C12). In the curve for the distribution, $P(V)$, for the sample C12 (Fig. 3.3), the smaller area under the peak assigned to $\gamma\text{-Fe}_2\text{O}_3$ indicates that the volume fraction of $\gamma\text{-Fe}_2\text{O}_3$ is small in the sample C12. The Mössbauer spectrum for the sample C12 observed at 80 K (Fig. 3.4) also supports this conclusion.

As far as the distribution curve, $P(V)$ and Mössbauer spectrum at 80 K are concerned, we observe a similarity between samples C11 and C21 as well as between samples C12, C22 and C41. We therefore conclude that the volume fraction of $\gamma\text{-Fe}_2\text{O}_3$ in the samples C12

and C22 decreases because of the increase in the nucleation and crystallization time period. As compared to the sample C12, C11 yields a lower value of ΔE because of the higher volume fraction of the fine particles of $\gamma\text{-Fe}_2\text{O}_3$. Similar behaviour is also observed for the samples C20, C21 and C22.

Let us now analyze the spectra of various samples for their magnetic hyperfine parameters. We first note that magnetic phases are precipitated in all the samples C11, C12, C21, C22, C31, C32 and C33 which have been heat treated. However as observed in Fig. 3.1c, the magnetic phases in the samples C31 and C32 have not grown enough (in population) to allow an accurate estimate of magnetic hyperfine parameters. Analysis of Mössbauer spectra for samples C11, C12, C21, C22, C41 and C33 measured at room temperatures supports the presence of a six-line spectrum having magnetic hyperfine parameters as $IS = 0.36 \pm 0.01 \text{ mm s}^{-1}$, $\Delta E = -0.112 \pm 0.005 \text{ mm s}^{-1}$, $H_{\text{int}} = 512 \pm 2 \text{ kOe}$ and $\Gamma = 0.23 \pm 0.01 \text{ mm s}^{-1}$. These parameters agree very closely with the set of parameters observed in the Mössbauer spectrum of $\alpha\text{-Fe}_2\text{O}_3$ [25]. The narrow line-widths ($0.23 \pm 0.01 \text{ mm s}^{-1}$) observed by us rule out any overlapping contribution from $\gamma\text{-Fe}_2\text{O}_3$ in these samples at room temperature. The Mössbauer spectra of these samples were also measured by us at 80 K and are shown in Fig. 3.4 and they confirm the presence of $\alpha\text{-Fe}_2\text{O}_3$

alongwith $\gamma\text{-Fe}_2\text{O}_3$ in the samples C11, C12, C21, C22 and C41. The Mössbauer spectrum (Fig. 3.4) of sample C11 observed at 80 K gives rise to two sets of values : (i) $\text{IS} = 0.49 \pm 0.03$ mm s⁻¹, $H_{\text{int}} = 514.0 \pm 5$ kOe and $\Delta E = 0$ (ii) $\text{IS} = 0.46 \pm 0.03$ mm s⁻¹, $H_{\text{int}} = 540 \pm 5$ kOe and $\Delta E = 0.17 \pm 0.03$ mm s⁻¹ (Table 3.6) and these are assigned to $\gamma\text{-Fe}_2\text{O}_3$ and $\alpha\text{-Fe}_2\text{O}_3$ respectively [25]. However such a resolution between the spectra from $\gamma\text{-Fe}_2\text{O}_3$ and $\alpha\text{-Fe}_2\text{O}_3$ was not observed for the Mössbauer spectrum for the sample C12 at 80 K (Fig. 3.4). This further supports our observation that the volume fraction of $\gamma\text{-Fe}_2\text{O}_3$ in the sample C12 is smaller.

It will be observed from Fig. 3.1c that the Mössbauer spectrum measured for the sample C33 is the most complex. Our data analysis, using computer program, has shown that the spectrum for the sample C33 can be resolved into one six-line spectrum attributable to $\alpha\text{-Fe}_2\text{O}_3$ and three other six line spectra attributable to substituted YIG (in addition to doublet spectra). The magnetic hyperfine parameters obtained by us for the YIG phase are shown in Table 3.3.

The Mössbauer spectrum of sample C33 at room temperature consists of characteristic spectrum of YIG accompanied by the spectrum of $\alpha\text{-Fe}_2\text{O}_3$ as well as of the glassy state of the material. The spectrum characteristic of YIG consists of spectra from d and a sublattices respectively. The d sublattice spectrum is symmetric about its

centroid but this is not the case with a sublattice spectrum. This difference arises out of the interaction between the quadrupole moment of the ^{57}Fe (in its first excited state) and the EFG at the nucleus. The YIG being a cubic ferrimagnetic crystal, neither the tetrahedral nor the octahedral iron site (which are occupied in a 3:2 ratio) has cubic symmetry. However each site has sufficient symmetry to ensure that the EFG tensor is axially symmetric [26]. The axis of the local symmetry of the EFG at the d site is in the $[100]$ direction because the d site corresponding to a tetrahedron of O^{2-} ions has a four-fold rotation inversion axis in the $[100]$ direction. On the other hand the octahedron has a three-fold axis of rotation in a $[111]$ direction which is also the axis of local symmetry of EFG tensor at the a site. As a result electric hyperfine interaction occurs and a combined effect of quadrupole splitting and magnetic hyperfine splitting is seen in the Mössbauer spectrum of each sublattice a. The magnitude of the quadrupole splitting depends on the angle β between the axis of local symmetry and the direction of magnetization. In YIG the easy direction of magnetization is along $[111]$ direction of the unit cell [26] which restricts the number of possible values of β to 3. All symmetry axes of the d sites make an angle of 55° with the direction of magnetization and as a result the quadrupole splitting $\langle e q^2 Q/4 \rangle (3 \cos^2 \beta - 1)$ is vanishingly

small. This gives a symmetric nature (about its centroid) to the Mössbauer spectrum of the d sublattice. In the case of a site β is either 70° or 0° , with the former occurring three times as often as the latter. Consequently the a sublattice gives rise to two six-line hyperfine spectra with the quadrupole splitting $\Delta E = -(0.12 \pm 0.03) \text{ mm s}^{-1}$ for the a' site ($\theta = 70^\circ$) and $\Delta E = +(0.05 \pm 0.15) \text{ mm s}^{-1}$ ($\theta = 0^\circ$), as shown by Van Loef in [26]. We propose to use this result while analyzing the Mössbauer spectrum of sample C33 (Table 3.3). We conclude from the above discussion that the Mössbauer spectrum of YIG at room temperature should consist of three different sets of six-line hyperfine spectra : one for the d-site nuclei and two for the a-site nuclei with their intensities in the ratio $I_{\underline{d}}:I_{\underline{a}'}:I_{\underline{a}}::6:3:1$.

We are now ready to analyze and interpret the room temperature Mössbauer spectrum of sample C33. As seen from Fig. 3.1c and Table 3.3 the computer analysis of the total spectrum of sample C33 has yielded 3 sets of different six-line spectra. We have, therefore, assigned these three sets of spectra to (i) YIG:d site, (ii) YIG:a' site and (iii) YIG:a site. The one yielding Mössbauer parameters $\Delta E = 0.0$ and $H_{\text{int}} = (392 \pm 2) \text{ kOe}$ is assigned to the YIG phase corresponding to the d-sublattice magnetization. This assignment agrees with the Mössbauer parameter $\Delta E \approx 0$ (see previous paragraph) and $H_{\text{int}} = (393.5 \pm 2.0) \text{ kOe}$

reported by Van Loef [26] for YIG at the corresponding tetrahedral \underline{d} -site. The other two six-line spectra (Table 3.3) have been assigned to YIG \underline{a}' and \underline{a} sites respectively. The main argument behind this assignment is the set of values of quadrupole splitting observed by us : $\Delta E = -0.13 \pm 0.03$ and $0.07 \pm 0.03 \text{ mm s}^{-1}$. These values agree (within the experimental error) with the values $\Delta E = -(0.12 \pm 0.03)$ and $\Delta E = +(0.05 \pm 0.15) \text{ mm s}^{-1}$ observed by Van Loef [26] and assigned by him to YIG \underline{a}' site and \underline{a} -site respectively.

Mössbauer measurements by Van Loef [22] further yield the values $H_{\text{int}} = 484.1 \pm 1.4 \text{ kOe}$ and $490.3 \pm 2 \text{ kOe}$ from the two other six-line spectra attributed to the octahedral \underline{a}' and \underline{a} sites respectively. The values of H_{int} observed by us for the other two six-line spectra (for the sample C33) are $H_{\text{int}} = 425 \pm 4$ and $431 \pm 4 \text{ kOe}$ and they appear to be lower than those reported by Van Loef [26] for the \underline{a}' and \underline{a} sites respectively. In spite of this observed difference in the values of H_{int} , we choose to assign the other two six-line spectra observed by us for the sample C33 to the \underline{a}' and \underline{a} sites in YIG. We justify our choice below by providing an explanation of the lower values of H_{int} observed by us.

Lyubutin et al. [27] have investigated the magnetic and electric hyperfine interactions of ^{57}Fe nuclei in vanadium and silicon garnets. The ^{57}Fe Mössbauer

spectroscopic studies of the substituted garnet systems $Y_{3-x}Ca_xFe_{5-x}Si_xO_{12}$ ($0 \leq x \leq 3.0$) and $Y_{3-2x}Ca_{2x}Fe_{5-x}V_xO_{12}$ ($0 \leq x \leq 1.5$) carried out by these authors showed that the hyperfine magnetic field H_{int} at the octahedral \underline{a} site decreases by about 10% with increasing content (x) of diamagnetic ions Si^{4+} and V^{5+} , but the H_{int} values at the \underline{d} site did not show much change with x .

The behaviour of the magnetization, Curie temperature, Mössbauer spectra and lattice parameter in the garnet series $Bi_{0.8}Ca_{2x}Y_{2.2-2x}Fe_{3-x}V_xO_{12}$ has been studied by Popma et al. [28]. Their measurement of the Mössbauer spectra of these samples at room temperature showed that the hyperfine field at the octahedral (\underline{a}' , \underline{a} sites) ^{57}Fe nuclei decreased by about 10% (from 483 to 440 kOe at the \underline{a}' site and from 495 to 447 kOe at the \underline{a} site) when the x -value was increased from $x = 0.0$ to 1.1. The value of H_{int} for the tetrahedral \underline{d} -site, on the other hand, did not show any change within the experimental error. The linewidth (Γ) of the \underline{a} -site (octahedral) spectral lines was also observed to increase with x . In other words, Popma et al. [28] have observed a decrease in H_{int} (at the \underline{a}' and \underline{a} sites) with x as a result of the increasing number of non-magnetic V^{5+} ions being substituted at the tetrahedral \underline{d} sites. This observed behaviour was ascribed by these authors [27,28] to the formation of

magnetically non-equivalent a sites in YIG because of the substitution of the diamagnetic d sites (arising out of the strong a-d interaction in garnets).

Keeping in mind these results by Lyubutin et al. [27] and Popma et al. [28] we propose that the other two six-line spectra observed by us for sample C33 arise from the a' and a sites in YIG. The reduction in the hyperfine magnetic fields to values $H_{int} = 425 \pm 4$ and 431 ± 4 kOe observed by us is attributed to the substitution of the Fe^{3+} ions at the d-sites by the diamagnetic Si^{4+} ions during the precipitation of YIG in the silicate glasses. This mechanism is similar to the one observed by Lyubutin et al. [27] and Popma et al. [28]. However in our case the linewidth of the a site spectral lines does not show any increase after the substitution of Si^{4+} ions. We explain this by proposing that the Si^{4+} ions get distributed uniformly during the precipitation of YIG in the glass sample thus arresting any line broadening.

A comment about the relative intensities of the lines at the d, a' and a sites is in order here. Van Loef [26] has observed that the relative intensities of the lines at the d, a' and a sites in YIG (measured at room temperature) are in the ratio 6:1:3. Results of the Mössbauer spectra measured by us for the sample C33 (at room temperature) indicate that this ratio is 2:1:3 in our case. This difference is again attributed to the

effect of Si^{4+} ions being substituted in place of Fe^{3+} ions at the d-sites. The occupation of the d-sites by Fe^{3+} ions is lowered by this process and as a consequence the relative intensity of the d-site line is reduced. It should be pointed out that the ratio of the intensities of lines due to the a' and a sites remained as 1:3 in our case.

As shown by Geller et al. [31] it is possible to observe the effects of spin reorientation in YIG:Si from the Mössbauer spectra. When the magnetization in the sample is in the [111] direction, the YIG a site produces two hyperfine spectra with appreciable quadrupole splitting and the YIG d site gives rise to a single hyperfine spectrum with negligible quadrupole splitting. If, however, the magnetization direction changes over to [100] direction, the a site produces single hyperfine spectrum with negligible quadrupole splitting while the d site will give rise to two hyperfine spectra with appreciable quadrupole splitting. Since the values of H_{int} for the a site and the d site are distinctly different, it is possible to analyze the Mössbauer spectra of YIG:Si for getting information about the easy axis (i.e. whether the magnetization is along the [111] or [100] direction). Working with YIG:Si samples having silicon content of 0.3 per formula unit, Geller et al. [32] observed the spin-reorientation region to be from 100-165 K. In their case

they observed the easy axis to be along the [111] direction at 298 K while at 80 K they observed the reorientation to be complete with the easy axis along the [100] direction. The mechanism of spin reorientation in YIG:Si is not understood completely, although it is certain that the induced Fe^{2+} ions are responsible for the continuous transition in YIG:Si, Rudowicz [33] employed the single-ion anisotropy and the two-center model to study theoretically the mechanism of spin reorientation in YIG:Si. Balestrino et al. [32] have carried out Mössbauer spectroscopic studies to show the composition dependence of the spin reorientation in silicon-substituted YIG and have proposed a semiquantitative model to explain their results in terms of the effects of Fe^{2+} ions.

We have measured the Mössbauer spectrum of the sample C33 at 293 K and 80 K. From these spectra we observed that the spin-reorientation changed from the [111] direction at 293 K to the [100] direction at 80 K. We could not locate the reorientation region because we could not make the measurements continuously over the temperature range (80 - 293 K). The Mössbauer spectrum of the sample C33 at 80 K was not well resolved as far as the different sites were concerned. Nevertheless we have obtained the following set of Mössbauer parameters (Table 3.6) for C33 at 80 K.

Table 3.6 : Parameters obtained from Mössbauer spectra for samples C11, C21 and C33 at 80 K.

Samples	Doublet spectra				Six line spectra			Assignment
	IS(a)	$\Delta E(b)$	$\Gamma(c)$	IS(a)	$\Delta E(b)$	$H_{int}(d)$	$\Gamma(c)$	
C11	0.27±0.03	0.73±0.03	0.53±0.03					
				0.49±0.03	0	514±5 KOe	0.31±0.02	Glass $\gamma\text{-Fe}_2\text{O}_3$
				0.46±0.03	+0.17±0.3	540±5 KOe	0.32±0.02	$\alpha\text{-Fe}_2\text{O}_3$
C21	0.33±0.03	0.90±0.03	0.52±0.03					Glass
				0.47±0.03	+0.13±0.03	537±5 KOe	0.36±0.02	$\alpha\text{-Fe}_2\text{O}_3$ small am- unt
C33	0.31±0.03	0.85±0.05	0.51±0.03					$\gamma\text{-Fe}_2\text{O}_3$ Glass
				+0.45±0.03	+0.13±0.03	527±10 KOe	0.33±0.02	$\alpha\text{-Fe}_2\text{O}_3$ and small amount
				+0.33±0.05	-0.04±0.05	495±10 KOe	-	$\gamma\text{-Fe}_2\text{O}_3$ YIG:Si - a site
				+0.43±0.05	+0.17±0.05	468±10 KOe	-	YIG:Si - d site
				+0.45±0.05	-0.20±0.05	459±10 KOe	-	YIG:Si - d' site

(a) IS = Isomer shift, values in mm s^{-1} with respect to $\alpha\text{-Fe}$ IS at 295 K.

ΔE = Electric quadrupole splitting in mm s^{-1}

(c) (FWHM) = width of the spectral line, values in mm s^{-1}

(d) H_{int} = Internal magnetic field at ^{57}Fe nucleus : in units of KOe.

- (i) $IS = 0.45 \pm 0.03 \text{ mm s}^{-1}$, $\Delta E = +0.13 \pm 0.03 \text{ mm s}^{-1}$, $\Gamma = 0.33 \pm 0.02 \text{ mm s}^{-1}$, $H_{\text{int}} = 527 \pm 10 \text{ kOe}$. These parameters are assigned to $\alpha\text{-Fe}_2\text{O}_3$ with a small amount of $\gamma\text{-Fe}_2\text{O}_3$ being present. The smaller value of $\Delta E = 0.13 \text{ mm s}^{-1}$ (as compared to the value of $\Delta E = 0.18 \text{ mm s}^{-1}$ for pure $\alpha\text{-Fe}_2\text{O}_3$) and the lower H_{int} value of 527 kOe are caused by the presence of small amount of $\gamma\text{-Fe}_2\text{O}_3$ present in C33.
- (ii) $IS = 0.33 \pm 0.05 \text{ mm s}^{-1}$, $\Delta E = -0.04 \pm 0.05 \text{ mm s}^{-1}$, $H_{\text{int}} = 495 \pm 10 \text{ kOe}$. These parameters are assigned to the a-site of YIG:Si.
- (iii) $IS = 0.43 \pm 0.05 \text{ mm s}^{-1}$, $\Delta E = 0.17 \pm 0.05 \text{ mm s}^{-1}$, $H_{\text{int}} = 468 \pm 10 \text{ kOe}$. These parameters are assigned to the d-site of YIG:Si.
- (iv) $IS = 0.45 \pm 0.05 \text{ mm s}^{-1}$, $\Delta E = -0.20 \pm 0.05 \text{ mm s}^{-1}$, $H_{\text{int}} = 459 \pm 10 \text{ kOe}$. These parameters are assigned to the d'-site of YIG:Si.

Lower values of H_{int} observed at 80 K for the a-site are attributed to the presence of Si^{4+} ions at the d-site. The higher values of IS observed at 80 K and 293 K are not understood by us clearly. One possible reason may be the following. The radius of the Si^{4+} ion is 0.26 \AA as compared to that of Fe^{3+} ion which is 0.49 \AA . This will lead to reduction in the size of tetrahedron wherever Si^{4+} has substituted Fe^{3+} ions. Further the Si^{4+} ion has more positive charge and hence the $\text{Si}^{4+} - \text{O}^{2-}$ size may

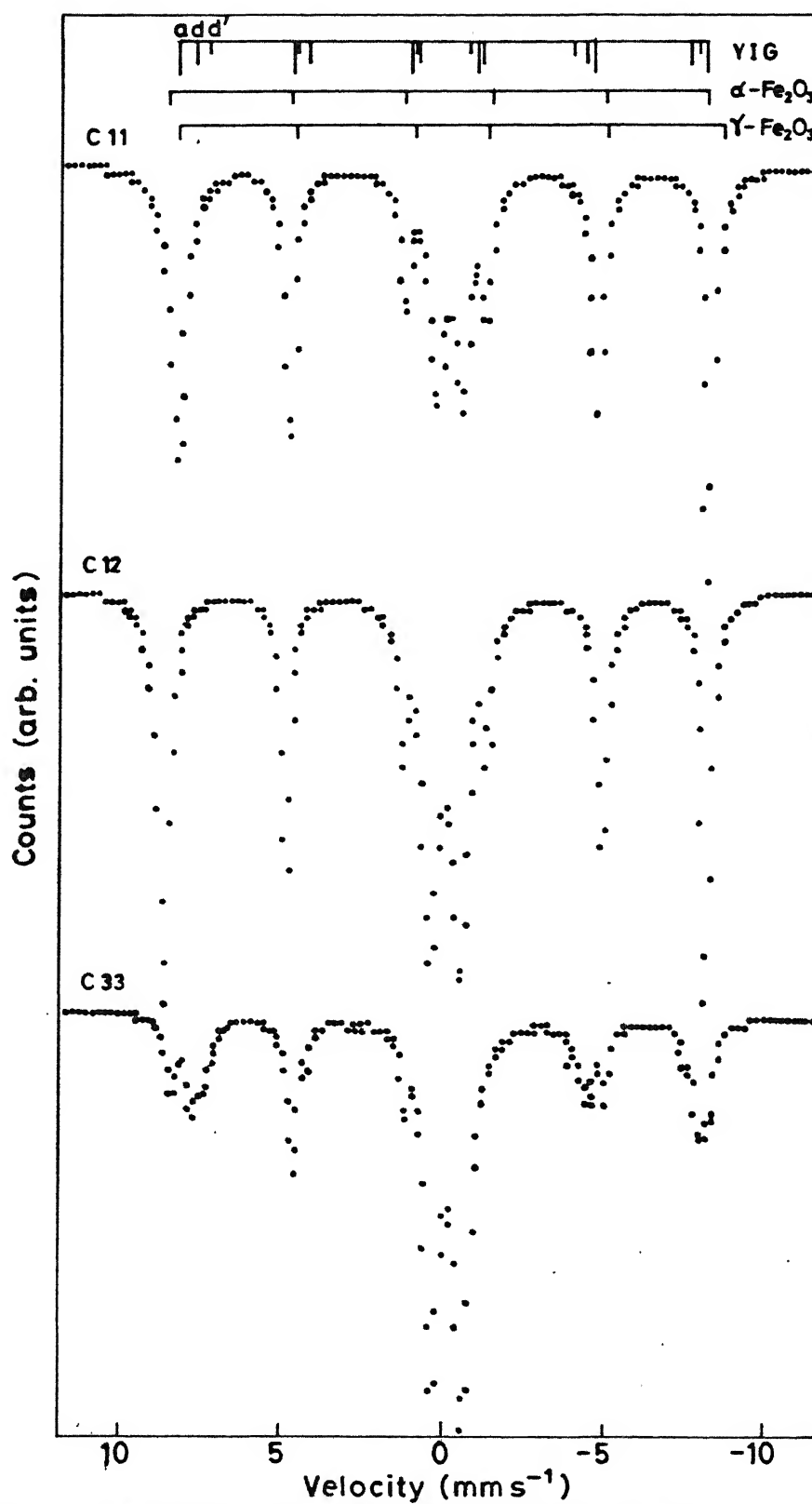


Fig. 3.4 Mössbauer spectra for C11, C12 & C33 at 80 K.

decrease and $\text{Fe}^{3+} - \text{O}^{2-}$ size may increase. As a result the s -electron density decreases at the Fe^{3+} nucleus at the Fe^{3+} tetrahedral site and this gives rise to a larger IS value.

The EPR measurements were carried out for samples C10, C11, C12, C21, C22 and C33 (Fig. 3.5) at 298 K. The EPR spectrum of the as-prepared sample C10 shows a broad resonance ($g \approx 2.1$) which is attributed to the amorphous nature of this sample. The other heat-treated samples C11, C12, C21 and C22 show two or three sharper resonances ($g \approx 1.6, 2.0$ and 2.6) and these are ascribed to the presence of more than one phase in all these samples. The large line-width $\Delta H \approx 1000$ Oe and the values $g \approx 2.0, 2.6$ confirm the formation of $\text{Fe}^{3+} - \text{O}^{2-} - \text{Fe}^{3+}$ and $\text{Fe}^{2+} - \text{O}^{2-} - \text{Fe}^{3+}$ superexchange coupled pairs and the appearance of inter-particle dipolar interaction between precipitated $\gamma\text{-Fe}_2\text{O}_3$, $\alpha\text{-Fe}_2\text{O}_3$ and YIG crystals in these samples [34].

The sample C33 exhibits a sharp resonance line with $\Delta H \approx 300$ Oe and $g \approx 2.1$ (Fig. 3.5). The resonance $g \approx 2.6$ which arises because of the presence of the distorted octahedrally and/or tetrahedrally coordinated Fe^{3+} magnetic site [5,35] is absent in the sample C33. Only one resonance $g \approx 2.1$ and $\Delta H \approx 300$ Oe, therefore, confirms the fact that the nucleating agent ($\text{As}_2\text{O}_3 + \text{Ag}_2\text{O}$) activates YIG:Si particles to grow free from structural defects.

As prepared glass sample C10 and various other heat-treated samples exhibit strong absorption of radiation from the near IR to the UV region. The optical absorption spectra obtained for samples C10, C22 and C33 are shown in Fig. 3.6. The spectrum from the sample C10 has very low absorption intensity in the UV (330 - 200 nm) region. The intensity in this region rapidly increases as heat-treated glass crystallizes. The spectrum shifts as a whole from the visible to the UV region in the case of series having the composition C1 and C2 (the representative sample being C22). The sample C33 indicates absorption having maximum intensity at ~ 550 nm accompanied by weak satellite bands extending in the UV region.

The increase of the absorption intensity in the UV region observed for the heat-treated samples is characteristic of the growth of the YIG crystalline phase. The spectrum of pure YIG [36] is often obscured below 400 nm (absorption becomes infinitely large) by the strong absorption of $O^{2-} - Fe^{3+}$ charge transfer bands and/or the continuous energy spectrum due to $3d^5 \rightarrow 3d^4 4p^1$ (Fe^{3+}) transition. This prohibits the measurement below this cut off limit even with a crystal as thin as ~ 0.5 mm (in thickness) used by Clogston [36]. The $3d^4 4p^1$ excited states, in fact, lie far below the UV region but a strong crystalline field, as in YIG, depresses these energy states and extends them in the UV region [37]. On account of

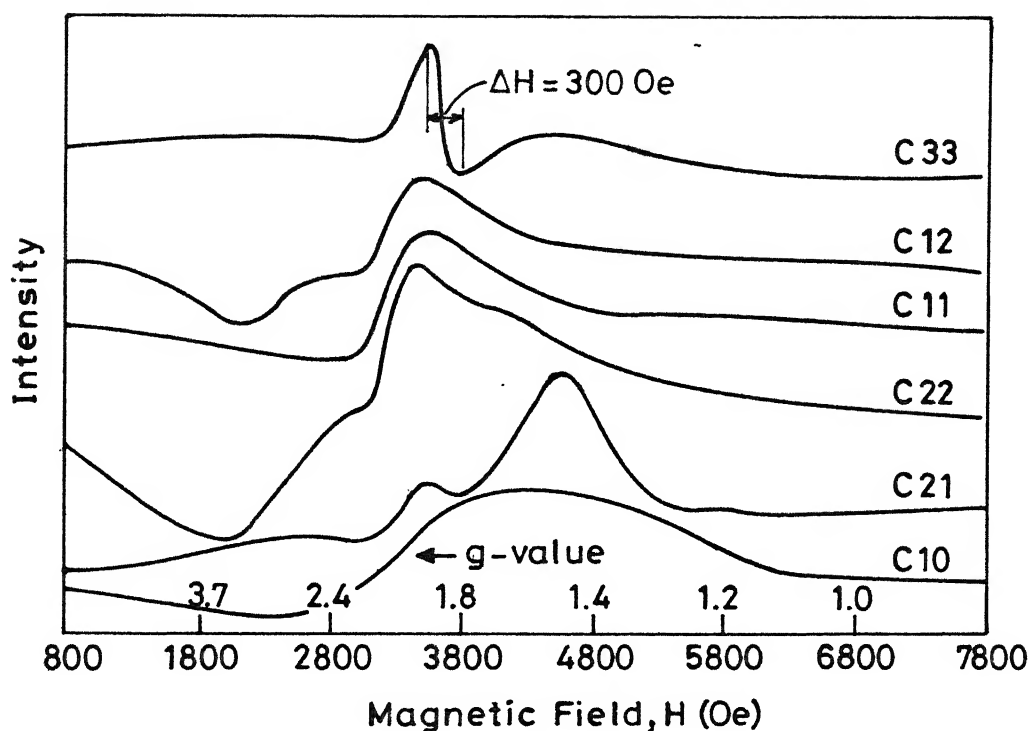


Fig. 3.5 EPR spectra of sample C10, C22, C11, C12 and C33.

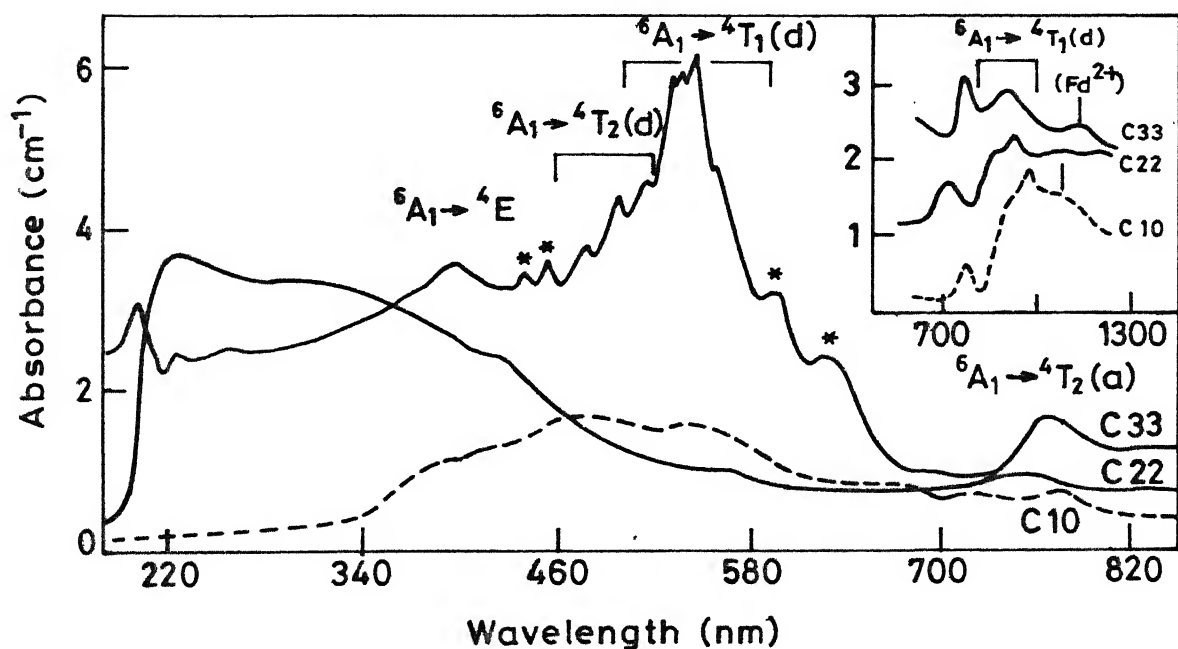


Fig.3.6 The electronic absorption spectra for sample C10, C22 and C33. Band marked by arrows refer Fe^{2+} absorption * vibronic band. Absorption scale is given for sample C33.

the above reason, the present glass systems do not show appreciable absorption in the UV region. The strength of the crystalline field of YIG is reduced and varies for the different samples showing a maximum effect for the sample C33 (which exhibits relatively weak absorption in the UV region in Fig. 3.6).

The electronic transitions of Fe cations have been extensively studied in YIG and other iron-containing systems [37-39]. In a close analogy, therefore, the spectrum shown for sample C33 (Fig. 3.6) can be easily assigned to various Fe^{3+} electronic transitions in tetrahedral and octahedral sites (Table 3.7). The bands associated with tetrahedral sites usually fall at lower wavelengths (higher energies) and exhibit stronger intensity than the corresponding bands at octahedral sites. This is in accordance with well-known criterion that the Fe^{3+} at tetrahedral sites exhibit an intensity which is about 15 times higher than that at the octahedral sites [38]. An anomalous peculiarity of the results in the sample C33 is the fact that it exhibits much enhanced intensity of ${}^6\text{A}_1 - {}^4\text{T}_1$ transition in the tetrahedral Fe^{3+} site assigned for ~ 550 nm band group. The multiple band structure corresponds to Stark splitting of the excited state (${}^4\text{T}_1$). The intensity (integrated) ratio for the corresponding bands in tetrahedral and octahedral sites is estimated to be ~ 100 . This is much larger than the expected ratio of

Table 3.7 : Absorption bands of Fe^{3+} corresponding to the different sites in YIG observed in sample C33.

Octahedral site nm	Tetrahedral site nm	Transitions
870(0.55)	563(4.0)	${}^6\text{A}_1 \rightarrow {}^4\text{T}_1$ (G)
	549(5.5)	
	540(5.3)	
	534(5.2)	
768(0.80)	515(3.4)	${}^6\text{A}_1 \rightarrow {}^4\text{T}_2$ (G)
	499(3.0)	
	480(2.3)	
	400(1.7)	${}^6\text{A}_1 \rightarrow {}^4\text{E}$ (G)
	365(1.3)	
	342(1.0)	
	332(0.9)	${}^6\text{A}_1 \rightarrow {}^4\text{T}_1$ (D)
	252(0.4)	${}^6\text{A}_1 \rightarrow {}^2\text{T}_1$ (F)
	230(0.3)	${}^6\text{A}_1 \rightarrow {}^2\text{T}_2$ (F)
	205(1.1)	

Absorbance (per cm thickness) are written in parentheses : The bands corresponding to octahedral sites below 400 nm are not identified. They are marked in the strong absorption due to the tetrahedral sites.

15 (the ratio of Fe^{3+} cations for YIG in the two sites is 3:2).

In conformity to our Mössbauer results, the above observation suggests substitution of Si^{4+} ions at the tetrahedral site in the garnet lattice. A most plausible reason which could account for the additionally induced intensity (electric dipole moment) seems to be the presence of Si^{4+} at the tetrahedral site. The formation of coupled Fe^{3+} - Si^{4+} dipole pairs in the resulting system would impart expectedly large dipole moment [40] by increasing the Fe-Si bond length. This is because of the fact that Si^{4+} has smaller radius ($\text{Si}^{4+} = 0.26 \text{ \AA}$) and more charge than Fe^{3+} (0.45 \AA). Also in YIG:Si few Fe^{2+} ions are produced at the octahedral sites and the bands characteristic of Fe^{2+} are shown in Fig. 3.6.

3.3 STUDY OF THE PRECIPITATION OF HEXAGONAL FERRITES ($\text{BaFe}_{12}\text{O}_{19}$, $\text{SrFe}_{12}\text{O}_{19}$, $\text{PbFe}_{12}\text{O}_{19}$) IN BORATE GLASSES

In the previous section we have presented the results of our studies of the sodium silicate glass ceramic system Na_2O - SiO_2 - Fe_2O_3 - Y_2O_3 in which mainly the YIG:Si was precipitated with the help of different nucleating agents like Bi_2O_3 , ($\text{As}_2\text{O}_3 + \text{Ag}_2\text{O}$) and Pd.

In this section of the present chapter we shall present the results of our studies of borate glasses ($\text{MO-B}_2\text{O}_3\text{-Fe}_2\text{O}_3$ where $\text{M} = \text{Ba, Sr or Pb}$) in which hexagonal ferrites are precipitated. No nucleating agent was added to this glass system because the borate glass system acts as a self-nucleating system. The ferrites $\text{BaFe}_{12}\text{O}_{19}$ (denoted as BaM in the literature), $\text{SrFe}_{12}\text{O}_{19}$ (denoted as SrM) and $\text{PbFe}_{12}\text{O}_{19}$ (PbM) were developed long ago by Went et al. [41] and Fahlenbrach and Heister [42] as a typical hexagonal ferrimagnetic oxide for permanent magnetic materials. These ferrites were also used as materials in the magnetic information storage methods such as master tapes and magnetic cards.

Recently barium-ferrite particulate media have generated considerable excitement because of their interesting digital and analog applications such as the possibility of superior recording performance at relatively low cost [43]. These applications arise because barium ferrite particulate media provide mass producible perpendicular recording media utilizing existing coating facilities. The barium ferrite particles when synthesized by the glass crystallization method, display suitable properties for making the particulate perpendicular media. Such media (consisting of these particles) allow high density recording even in a low coercivity range in which

a ferrite head is usable without saturation. Such media further offer several advantages like excellent mass producibility, high recording density, good oxidation resistance^{and} preservation of existing head-medium interface [43]. Barium ferrite particulate media have been utilized in fields ranging from audio and video recorders to flexible disk memories, as promising high density recording media.

At this Institute, Ram et al. [44] have developed glass ceramics containing barium and strontium hexaferrites respectively as the major phase, which have been developed in the glass system $\text{MO-B}_2\text{O}_3\text{-Fe}_2\text{O}_3$ ($\text{M} = \text{Ba}, \text{Sr}$). The optimum conditions for crystallization of the hexaferrite phase have been examined by varying the nucleation and growth times. These workers [44] have determined that the hexaferrite is the major magnetic crystalline phase in most of the samples and they have shown that the microstructure, coercivity and other magnetic properties are strongly dependent on the heat-treatment schedule. In another paper Ram et al. [45] have reported similar studies on hexagonal lead ferrites. We, therefore, thought it interesting to study the magnetic phases in $\text{MO-B}_2\text{O}_3\text{-Fe}_2\text{O}_3$ ($\text{M} = \text{Ba}, \text{Sr}$ or Pb) by Mössbauer spectroscopy. To this end we have varied the heat-treatment schedule and studied the Mössbauer spectra of such heat-treated samples. Results of these studies are described in detail in the following.

3.3.2 Experimental

The glass compositions chosen for the three MO-B₂O₃-Fe₂O₃ systems were (by wt %)

- (i) 35 BaO - 40 B₂O₃ - 25 Fe₂O₃
- (ii) 35 SrO - 40 B₂O₃ - 25 Fe₂O₃
- (iii) 47 SrO - 28 B₂O₃ - 25 Fe₂O₃
- (iv) 50 PbO - 30 B₂O₃ - 20 Fe₂O₃.

The glasses were prepared by melting and casting the required mixture of oxides (reagent grade chemicals) in an alumina crucible between 1400 K and 1750 K in an electrically heated furnace [44, 45]. The samples were then heat-treated in two successive steps at various combinations of nucleation and growth temperatures to obtain ceramised glasses.

The as-prepared glass sample for the above four compositions were labelled as B10, S10, S20 and P10 respectively (Table 3.8). The schedule of heat-treatment given to these samples is described in Table 3.8 where the temperature and period of the nucleation and crystallization stage are given. The glass transition (T_g) and crystallization (T_c) temperatures were estimated from DTA obtained on an MOM Hungary derivatograph.

The as-prepared glasses as well as the heat-treated glasses were powdered and the absorbers for Mössbauer spectroscopy were prepared by following the method

Table 3.8 : Sample lables and details of heat-treatment given to different glass composition (heat-treatment is described in terms of teperature/period) with X-rays. and magnetization data.

Composition	Heat treated Degrees K/period	Sample label	Crystalline phase identified from X-ray analysis [44,45] S - Strong W - Weak	M (emu g ⁻¹) at H=10 kG [44,45]	H_c (G) [44,45]	T_c (K) [44,45]
35BaO-40B ₂ O ₃ -25Fe ₂ O ₃	-	B10	-	-	-	-
	850/2h + 895/20h	B11	-	-	-	-
	850/2h + 1015/20h	B12	-	-	-	-
	850/2h + 1065/2h	B13	BaFe ₁₂ O ₁₉ and α -Fe ₂ O ₃ (W)	14.0	500	635,725
35SrO-40B ₂ O ₃ -25Fe ₂ O ₃	850/2h + 1065/20h	B14	BaFe ₁₂ O ₁₉ (S) and α -Fe ₂ O ₃ (W)	-	-	-
	975/2h + 1015/2h	B15	Barium Borate (W) BaFe ₁₂ O ₁₉ (S) and α -Fe ₂ O ₃ (W)	13.5	315	590,750
	1035/2h + 1065/5h	B16	BaFe ₁₂ O ₁₉ (single phase)	11.5	1050	720
	-	S10	-	-	-	-
	885/5h + 1035/10h	S11	SrFe ₁₂ O ₁₉ (S)	7.3	385	750,850
47SrO-28B ₂ O ₃ -25Fe ₂ O ₃	965/2h + 1120/10h	S12	SrFe ₁₂ O ₁₉ (S) Fe ₂ O ₃ (W)	7.2	235	750,850
	-	S20	-	-	-	-
	1100/2h+1135/25h	S21	SrFe ₁₂ O ₁₉ (S) Fe ₂ O ₃ (W)	4.5	4300	730,830
	-	P10	-	-	-	-
50PbO-30B ₂ O ₃ -20Fe ₂ O ₃	725/2h + 765/2h	P11	PbFe ₁₂ O ₁₉ (S) α -Fe ₂ O ₃ (W)	9.0	1580	695,920
	850/2h + 925/2h	P12	PbsFe ₁₄ O ₂₆ (W) FeB ₄ O ₇ α -Fe ₂ O ₃ (W)	2.5	765	670,925

described earlier (Sec. 3.2). Mössbauer spectra were recorded at room temperature (293 K) with the apparatus described earlier.

3.3.3 Results and Discussion

The Mössbauer spectra from the as-prepared glass samples B10, S10, S20 and P10 were observed to be similar (Fig. 3.7) and they all showed three lines which could be decomposed into two doublets. Such an analysis of a representative sample S20 is shown in Fig. 3.7(a). The Mössbauer parameters of the two doublet spectra arising out of S20 are as follows (Table 3.9).

- (i) $IS = +0.445 \pm 0.005 \text{ mm s}^{-1}$, $\Delta E = 1.040 \pm 0.010 \text{ mm s}^{-1}$ and $\Gamma = 0.58 \pm 0.01 \text{ mm s}^{-1}$. This spectrum can be assigned to Fe^{3+} in six coordination with O^{2-} ions [46, 47].
- (ii) $IS = +0.977 \pm 0.005 \text{ mm s}^{-1}$, $\Delta E = 2.60 \pm 0.01 \text{ mm s}^{-1}$ and $\Gamma = 0.58 \pm 0.01 \text{ mm s}^{-1}$. This spectrum is attributed to Fe^{2+} in glassy medium [48].

The large value of the line-widths (Γ) observed by us are characteristic of borate (and other) glasses. The probability distribution $P(V)$ for the EFG (V_{zz}) corresponding to two doublet spectra for S20 are shown in Fig. 3.7(b). The numerical values for various parameters related to the $P(V)$ distribution are given in Table 3.9.

Table 3.9 : Different Mössbauer parameters for sample S2O
at 293 K.

Mössbauer parameter obtained from Lorentzian least square fit program.

Doublet	IS(a)	ΔE (b)	Γ (c)
Ist	+ 0.445	1.040	0.58
IInd	+ 0.977	2.60	0.58

Different parameters related to the P(V) distribution.

Doublet	Mean value $\Delta L = \sum_i P_i(V_i)V_i$ (mm s ⁻¹)	$\overline{\Delta E}$ FWHM of the P(V) Dis- tribution (mm s ⁻¹)	Number of Fourier Coefficient	2
Ist	0.91	0.64	20	1.46
IInd	2.45	0.71		

(a) IS = Isomer shift, values in mm s⁻¹ with respect to room temperature α -Fe : Typical error is ± 0.005 mm s⁻¹.

(b) ΔE = Electric quadrupole splitting in mm s⁻¹ :
Typical error is ± 0.01 mm s⁻¹.

(c) Γ (FWHM) = Width of the spectral line, value in
mm s⁻¹ : Typical error is ± 0.01 mm s⁻¹.

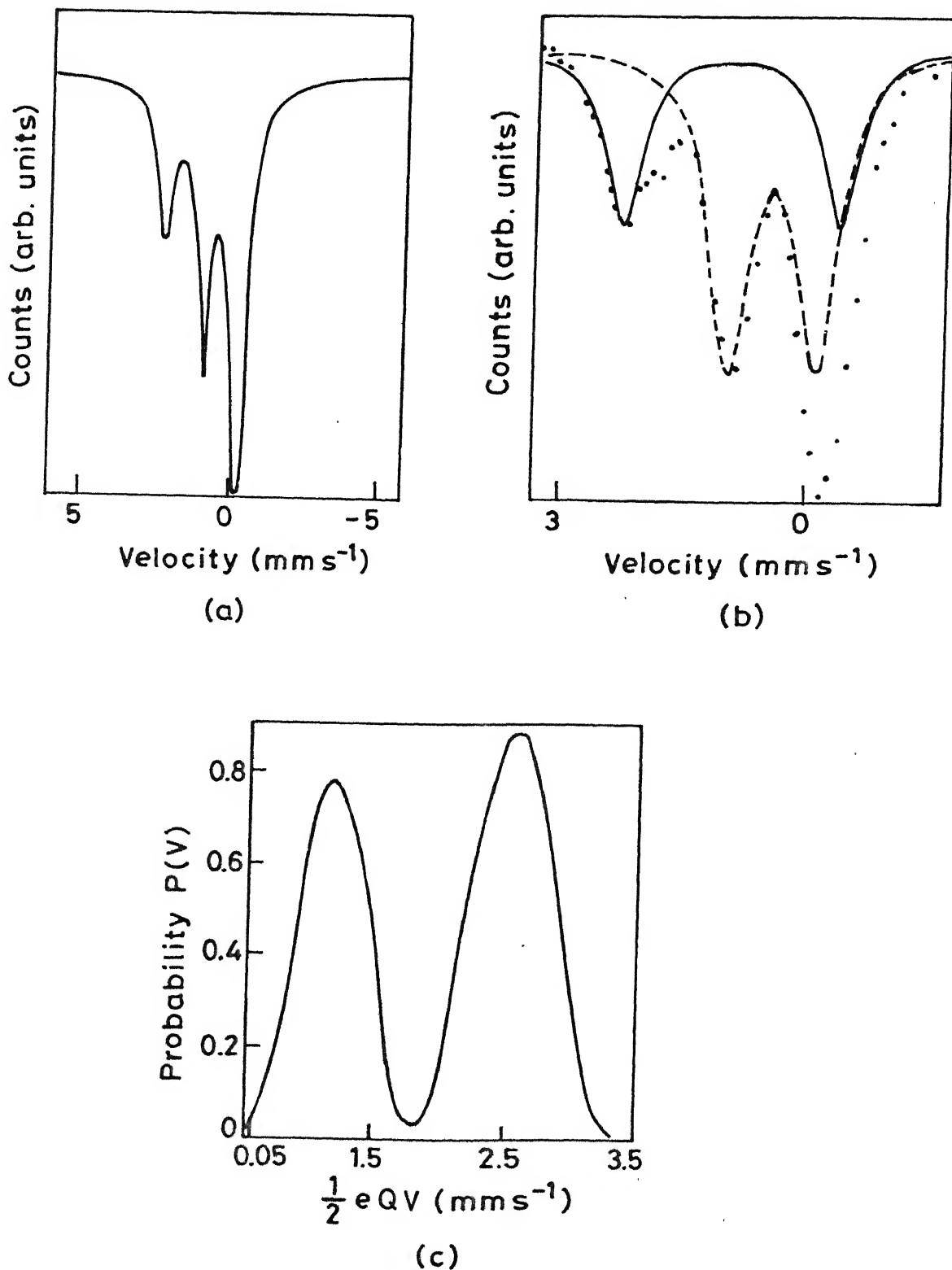


Fig. 3.7 (a) Mössbauer spectrum of S20 at 293K
 (b) S20 spectrum resolved in two doublet
 (c) Distribution of the electric field gradient, $P(V)$, at ^{57}Fe nuclei in S20.

We now turn our attention to the Mössbauer spectra of heat-treated samples, taking the 35 BaO-40 B₂O₃- 25 Fe₂O₃ sample first. The spectra of these samples B11, B12, B13, B14, B15 and B16 are shown in Fig. 3.8a-3.8b. All these spectra appear complex in nature. Taking clue from the results of Ram et al. [44] on X-ray analysis etc. (See Table 3.8) we looked for the presence of the magnetic phases BaFe₁₂O₁₉ and α -Fe₂O₃. It is known that the Mössbauer spectrum of BaFe₁₂O₁₉ consists of five sextets arising out of five different magnetic sublattices [49,50]. The sublattice magnetization of BaFe₁₂O₁₉ has been studied by Van Loef and Franssen [51] and by Kreber et al. [52]. Fundamental properties of hexagonal ferrites with magnetoplumbite structure have been reviewed by Kojima [53, 54]. In Table 3.10 we summarize the Mössbauer parameters of the five sextets assigned to BaFe₁₂O₁₉ in these (B11 to B16) samples. The assignment of the sublattice (a, b, c, d or e) has been made on the basis of the H_{int} value reported by Van Loef and Franssen [51] and Kreber et al. [52]. It may be pointed out that the value of H_{int} (for each sublattice) obtained for the B11 sample appears much lower than the corresponding H_{int} values for other (B12 to B16) samples. We ascribe this behaviour to the effect of super-paramagnetism arising out of incomplete crystallization in sample B11 (since its second stage heating was done at 895 K as compared to

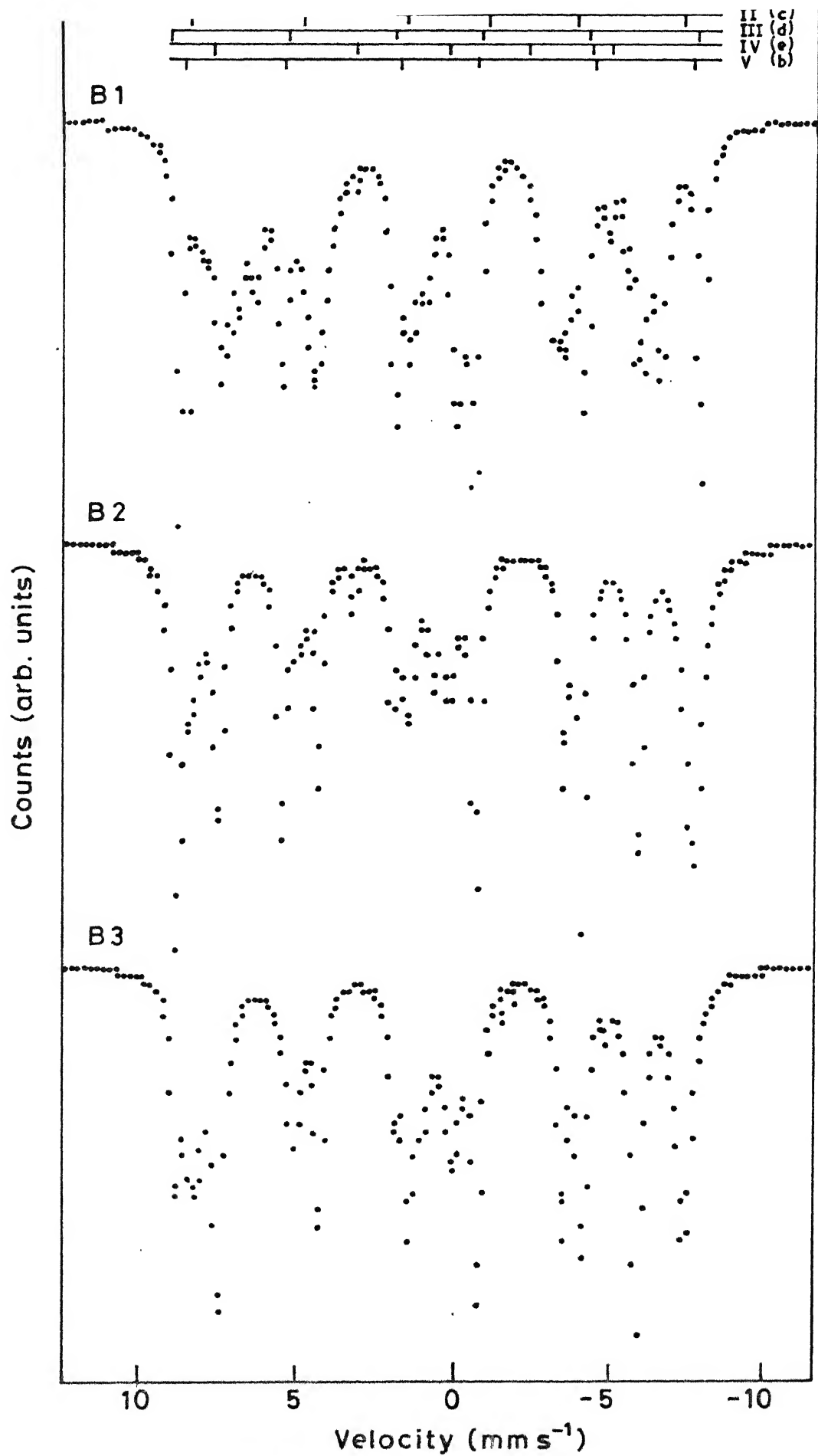


Fig. 3.8(a) Mössbauer spectra at B11, B12, and B13 at 293K.

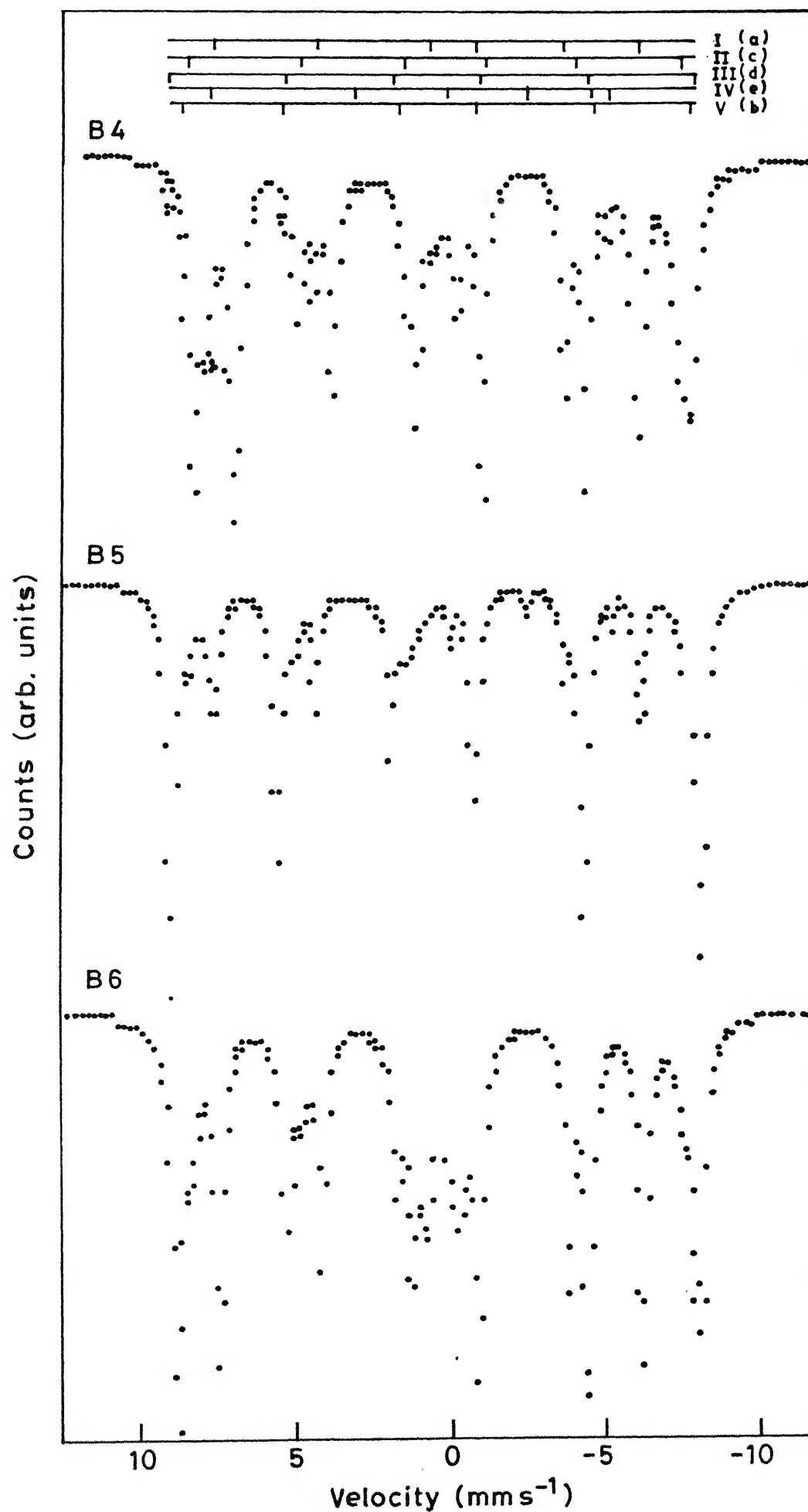


Fig.3.8(b) Mössbauer spectra at B14, B15 and B16 at 293 K.

Table 3.10 : Mössbauer parameters of samples B11, B12, B13, B14, B15 and B16 at 293 K.

Assign- ment	Sample B11			Sample B12			Sample B13			Sample B14			Sample B15			Sample B16		
	IS	ΔE	H_{int}	IS	ΔE	H_{int}	IS	ΔE	H_{int}	IS	ΔE	H_{int}	IS	ΔE	H_{int}	IS	ΔE	H_{int}
I(a)	0.32	0.10	390	0.39	0.19	409	0.35	0.13	418	0.36	0.12	420	0.37	0.13	420	0.36	0.13	420
II(c)	0.24	0.05	420	0.22	0.09	475	0.24	0.09	480	0.22	0.09	485	0.23	0.06	480	0.22	0.08	480
III(d)	0.36	0.12	450	0.37	0.09	514	0.34	0.10	510	0.34	0.10	510	0.38	0.12	512	0.36	0.12	510
IV(e)	0.15	1.40	418	0.13	1.40	420	0.12	1.37	435	0.10	1.42	420	0.11	1.48	422	0.11	1.46	420
V(b)	0.38	0.06	420	0.36	0.09	465	0.40	0.03	460	0.39	0.05	455	0.36	0.08	460	0.36	0.06	465
α -Fe ₂ O ₃	0.36-0.11	512	0.36-0.11	512	Small amount α -Fe ₂ O ₃ possible	512	Small amount α -Fe ₂ O ₃ possible	512	Small amount α -Fe ₂ O ₃ possible	515	0.36-0.11	515	0.36-0.11	515	0.36-0.11	512		

IS = Isomer shift values in mm s⁻¹ with respect to α -Fe : Typical error \pm 0.08 mm s⁻¹.

ΔE = Quadrupole splitting in mm s⁻¹ : Typical error is \pm 0.09 mm s⁻¹.

H_{int} = Internal magnetic field at ⁵⁷Fe nucleus : Typical error is \pm 10 kOe.

≥ 1015 K for other samples, See Table 3.8). Because of this behaviour, the results of the H_{int} values of B11 were not considered while assigning the sublattices. In other words the sublattice were assigned using the H_{int} values of the samples B12 to B16. The sublattices in the sample B11 were assigned by examining the values of IS and ΔE and by comparing them with the values for the other samples B12 to B16.

Table 3.10 also shows the Mössbauer parameters of the $\alpha\text{-Fe}_2\text{O}_3$ phase present in varying degree in samples B11-B16. It is observed that the volume fraction of $\alpha\text{-Fe}_2\text{O}_3$, as deduced from Mössbauer spectra, is smaller in samples B13, B14 and B16. Ram et al. [44] had previously studied the samples B13, B15 and B16. The data for the values of magnetization M and coercive field H_c , temperature T_c as well as the crystalline phase identified by them from X-ray analysis for samples B13, B15 and B16 are also reproduced in Table 3.8.

We have been able to identify different magnetic phases and optimum temperatures and time periods for maximum volume fraction of BaM in the present glass system. The $\alpha\text{-Fe}_2\text{O}_3$ phase is present in all the samples (B11-B16) although in varying proportion. The X-ray diffraction studies [44], however reveals the presence of the BaM phase (and no $\alpha\text{-Fe}_2\text{O}_3$) in B16. It is known that there is

no 1:1 correspondence between the results about volume fraction of a phase obtained from X-ray diffraction and Mössbauer spectroscopic results particularly when the volume fractions involved are small. This behaviour probably arises out of the different size (and nature) of samples required for the two techniques. Results of the magnetic measurements in the present case [44] provide evidence that fine particles of $\gamma\text{-Fe}_2\text{O}_3$ may be present along with $\alpha\text{-Fe}_2\text{O}_3$. This is indicated by the plot of magnetization versus magnetic field for different samples, where it was observed that none of these samples saturates upto a field of 10 kG.

According to the results of our Mössbauer measurements (Fig. 3.8a-3.8b), the maximum volume fraction of BaM is present in sample B14. It is indicated, on the basis of Mössbauer measurements, that the optimum nucleation temperature is 850 K and optimum crystallization temperature is 1065 K with time periods being 2h and 20h respectively (Table 3.10). We now discuss each of the samples in the series B11 to B16 on the basis of their Mössbauer measurements. The presence of $\alpha\text{-Fe}_2\text{O}_3$ is indicated in B11 as shown by the intense lines characteristic of $\alpha\text{-Fe}_2\text{O}_3$. While going from sample B11 to the sample B12, the nucleation temperature (850 K) and time period (2h) (Table 3.8) remains same but the crystallization temperature is increased from 895 to 1015 K. This has led to a reduction

in the volume fraction of $\alpha\text{-Fe}_2\text{O}_3$ (Fig. 3.8a). We also observed that the volume fraction of different phases is also affected by the time period of heat treatment given to the samples. As we go from the sample B13 to B14 the nucleation temperature and the time period as well as the crystallization temperature remains same but the time period for the crystallization stage is increased from 2h to 20h. This has resulted in the reduction of the volume fraction of the $\alpha\text{-Fe}_2\text{O}_3$ phase. It is possible that the increase in the crystallization time period helped Fe_2O_3 and barium borate to react and to give rise to BaM. Similar result was reported in the case of the synthesis of BaM from a mixture of barium-carbonate and iron oxide [55]. These authors found that BaFe_2O_4 is formed as an intermediate product which further reacts with Fe_2O_3 to give BaM. In the case of our present composition it is likely that BaB_2O_9 is the main intermediary product because the temperature of heat treatment is much lower than what was used for the ceramic method [55].

We shall now discuss the results of our studies of the systems $35\text{SrO}-40\text{B}_2\text{O}_3-25\text{Fe}_2\text{O}_3$ and $47\text{SrO}-28\text{B}_2\text{O}_3-25\text{Fe}_2\text{O}_3$ through the samples S11, S12 and S21 (Table 3.8). The Mössbauer spectra of all these three samples (S11, S12 and S21, see Fig. 3.9) show non-flat base line which is an indication of the effect of spin-fluctuations arising out of superparamagnetism [56]. In the case of sample

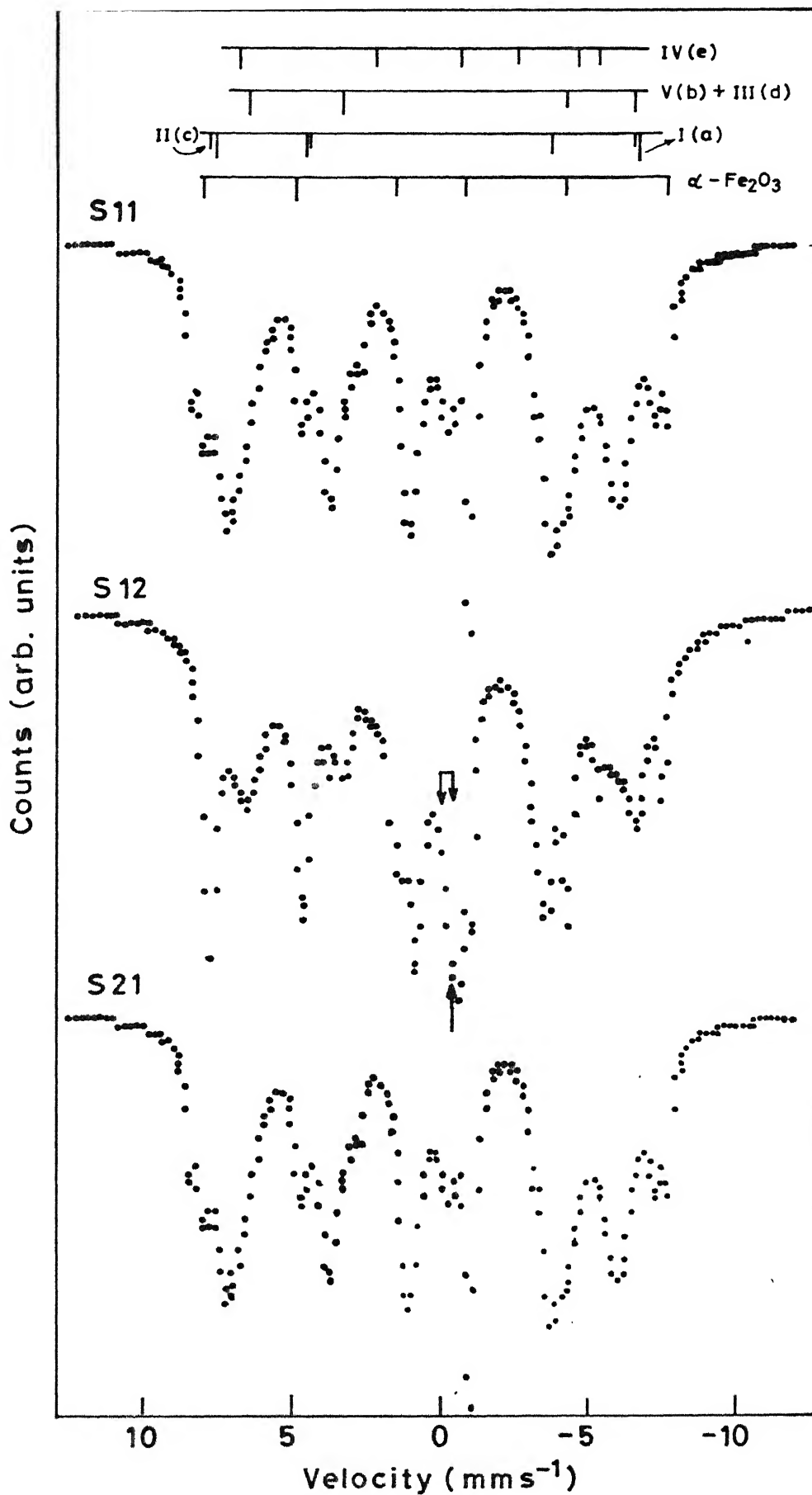


Fig.3.9 Mössbauer spectra of S11, S12, S21 at 293K.

S11, the Mössbauer lines corresponding to $\alpha\text{-Fe}_2\text{O}_3$ are seen distinctly with the relevant Mössbauer parameters as $IS = 0.36 \pm 0.01 \text{ mm s}^{-1}$, $\Delta E = -0.12 \text{ mm s}^{-1}$ and $H_{\text{int}} = 515 \pm 5 \text{ kOe}$. In addition to the lines arising out of $\alpha\text{-Fe}_2\text{O}_3$, the spectrum of sample S11 shows the presence of other lines which are assigned to the five magnetic sublattices of $\text{SrFe}_{12}\text{O}_{19}$ (SrM) as suggested by Kreber et al. [52] and Belov et al. [57]. Following Kreber et al. [52] we observe that the lines due to the sublattice V(b) and III(d) appear too close to be resolved while the other lines due to the sublattices I(a), II(c) and IV(e) appear resolved (Fig. 3.9). The Mössbauer parameters for the sublattice of $\text{SrFe}_{12}\text{O}_{19}$ as analyzed by us from our spectra are shown in Table 3.11 where these results are also compared with the Mössbauer parameters reported by Belov et al. [57] for $\text{SrFe}_{12}\text{O}_{19}$. It is seen that there is good agreement between our results and those obtained by Belov et al. [57]. We, however, observe from our spectra that the intensity of the spectral lines due to V(b) and III(d) sublattices is lower than those due to the I(a) and II(c) sublattices. We ascribe this behaviour to the presence of $\alpha\text{-Fe}_2\text{O}_3$ along with SrM in our samples, which make the computer analysis of the spectra difficult. We further point out that the X-ray analysis (see Table 3.8) does not reveal the presence of $\alpha\text{-Fe}_2\text{O}_3$ in the sample S11. Once again this type of behaviour shows that the

Table 3.11 : Mössbauer parameter of samples S11, S12 and S21 at 293 K.

Assignment	Sample S11				Sample S12				Sample S21				Results by Belov et al. [57] for SrFe ₁₂ O ₁₉			
	IS	ΔE	H _{int}		IS	ΔE	H _{int}		IS	ΔE	H _{int}		IS	ΔE	H _{int}	
I(a)	0.43	0.22	420		0.46	0.26	410		0.46	0.24	415		0.49	0.19	402	
II(c)	0.36	0.04	495		0.32	0.06	485		0.35	0.06	485		0.30	0.05	486	
SrM III(d)+V(b)	0.42	0.18	510		0.40	0.15	512		0.42	0.15	515		0.41	0.15	506	
	0.22	1.08	410		0.23	0.10	410		0.24	1.08	410		0.23	1.14	406	
α-Fe ₂ O ₃	0.36	-0.12	515		0.34-0.11		512		0.36-0.11		512		±0.03	±0.03	± 5	
IV(e)	±0.01		± 5													
<u>Sr₃Fe₂O_{6.2}</u>																
Fe ^{IV}					-0.32	-	-		-0.34							
Fe ³⁺					+0.32	0.40	-		0.33	0.42						

IS = Isomer shift values in mm s⁻¹ with respect to $\alpha\text{-Fe}$: Typical error ± 0.06 mm s⁻¹.
 ΔE^{H} = quadrupole splitting : Typical error ± 0.08 mm s⁻¹.
 H_{int} = Internal magnetic field : Typical error ± 10.0 kOe.

two techniques, X-ray diffraction and Mössbauer spectroscopy differ in their sensitivities because of the different nature (i.e. thickness, powdered nature, surface or bulk studied etc.) of the samples analyzed.

The Mössbauer spectrum for the sample S12 shows the presence of spectral lines from $\alpha\text{-Fe}_2\text{O}_3$ and SrM, (Fig. 3.9) although the amount of $\alpha\text{-Fe}_2\text{O}_3$ in the sample S12 appears to be lower than that in the sample S11. It is further observed that the intensity of the low-velocity lines is higher in the Mössbauer spectrum of sample S12 and this suggests the presence of phases other than $\alpha\text{-Fe}_2\text{O}_3$ and SrM. These additional phases could be $\text{Sr}_3\text{Fe}_2\text{O}_{6.9}$ and $\text{SrFe}^{\text{IV}}\text{O}_3\text{-SrFe}^{\text{III}}\text{O}_{2.5}$. However the Mössbauer spectrum of $\text{SrFe}^{\text{IV}}\text{O}_3\text{-SrFe}^{\text{III}}\text{O}_{2.5}$ is known to give a single line [58] at a velocity indicated by a dotted arrow in Fig. 3.9. It is seen that at this velocity the line due to $\text{SrFe}^{\text{IV}}\text{O}_3\text{-SrFe}^{\text{III}}\text{O}_{2.5}$ is totally masked by the lines due to $\alpha\text{-Fe}_2\text{O}_3$ and SrM. It is therefore difficult to confirm the presence of $\text{SrFe}^{\text{IV}}\text{O}_3\text{-SrFe}^{\text{III}}\text{O}_{2.5}$ in our spectra. It has been reported [59] that $\text{Sr}_3\text{Fe}_2\text{O}_{6.9}$ gives rise to three lines in the Mössbauer spectrum with a singlet due to Fe^{IV} with $\text{IS} = -0.32 \text{ mm s}^{-1}$ and a doublet due to Fe^{3+} with $\text{IS} = +0.32 \text{ mm s}^{-1}$ and $\Delta E = 0.40 \text{ mm s}^{-1}$. We have indicated the expected peak position of these three lines due to $\text{Sr}_3\text{Fe}_2\text{O}_{6.9}$ in our spectrum (Fig. 3.9) by solid

arrows. We feel, therefore, that there is evidence for the presence of $\text{Sr}_3\text{Fe}_2\text{O}_{6.9}$ phase in sample S12 as revealed by our Mössbauer spectrum. In Table 3.11 we have given the Mössbauer parameters of $\text{Sr}_3\text{Fe}_2\text{O}_{6.9}$ as analyzed from our spectra.

The Mössbauer spectrum of the sample S21 also shows the presence of $\alpha\text{-Fe}_2\text{O}_3$, SrM and $\text{Sr}_3\text{Fe}_2\text{O}_{6.9}$ (Fig. 3.9). The Mössbauer parameters obtained for the sample S21 are given in Table 3.11, where it is observed that the experimental errors are relatively larger for the sample S21. This effect is due to the fact that different lines in the Mössbauer spectrum for the sample S21 are poorly resolved. We ascribe this behaviour to the composition of the sample S21 ($47\text{SrO}-28\text{B}_2\text{O}_3-25\text{Fe}_2\text{O}_3$) which is different from that of the samples S11 and S12 ($35\text{SrO}-40\text{B}_2\text{O}_3-25\text{Fe}_2\text{O}_3$).

A comparison of the results for the three samples S11, S12 and S21 is in order here. All these three samples show the presence of $\alpha\text{-Fe}_2\text{O}_3$ and SrM while the samples S12 and S21 indicate the presence of the additional phase $\text{Sr}_3\text{Fe}_2\text{O}_{6.9}$. We feel that the phase $\text{Sr}_3\text{Fe}_2\text{O}_{6.9}$ is being crystallised in the samples S12 and S21 because the heat-treatment of these two samples involves nucleation and crystallization at temperatures higher than that for the sample S11 (Table 3.8). If the aim of the heat-treatment is to achieve a more efficient precipitation of SrM then our results indicate that the heat-treatment

Table 3.12 : Mössbauer parameters of samples P11 and P12
at 293 and 80 K.

Sample Temperature K	Double Spectra			Six-line Spectra			
	IS(a) mms ⁻¹	ΔE (b) mms ⁻¹	Γ (c) mms ⁻¹	IS(a) mms ⁻¹	ΔE (b) mms ⁻¹	H_{int} (d) kOe	Γ (c) mms ⁻¹
P11/80 K	0.38	1.85	0.32	0.46	0.16	540	0.32
P11/293 K	0.30	1.81	0.32	0.36	-0.12	512	0.33
P12/80 K	0.39	1.69	0.32 ± 0.02	0.46	0.18	540	0.34
P12/293 K	0.34	1.72	0.31 ± 0.02	0.36	0.12	512	0.32

(a) IS = Isomer shift measured with respect to α -Fe : Typical error ± 0.01 .
room temperature

(b) ΔE = Quadrupole splitting : Typical error ± 0.01 mm s⁻¹.

(c) Γ (FWHM) = Width of the spectral line : Typical error ± 0.01 mm s⁻¹.

(d) H_{int} = Internal magnetic field at ⁵⁷Fe nucleus : Typical error ± 3 kOe.

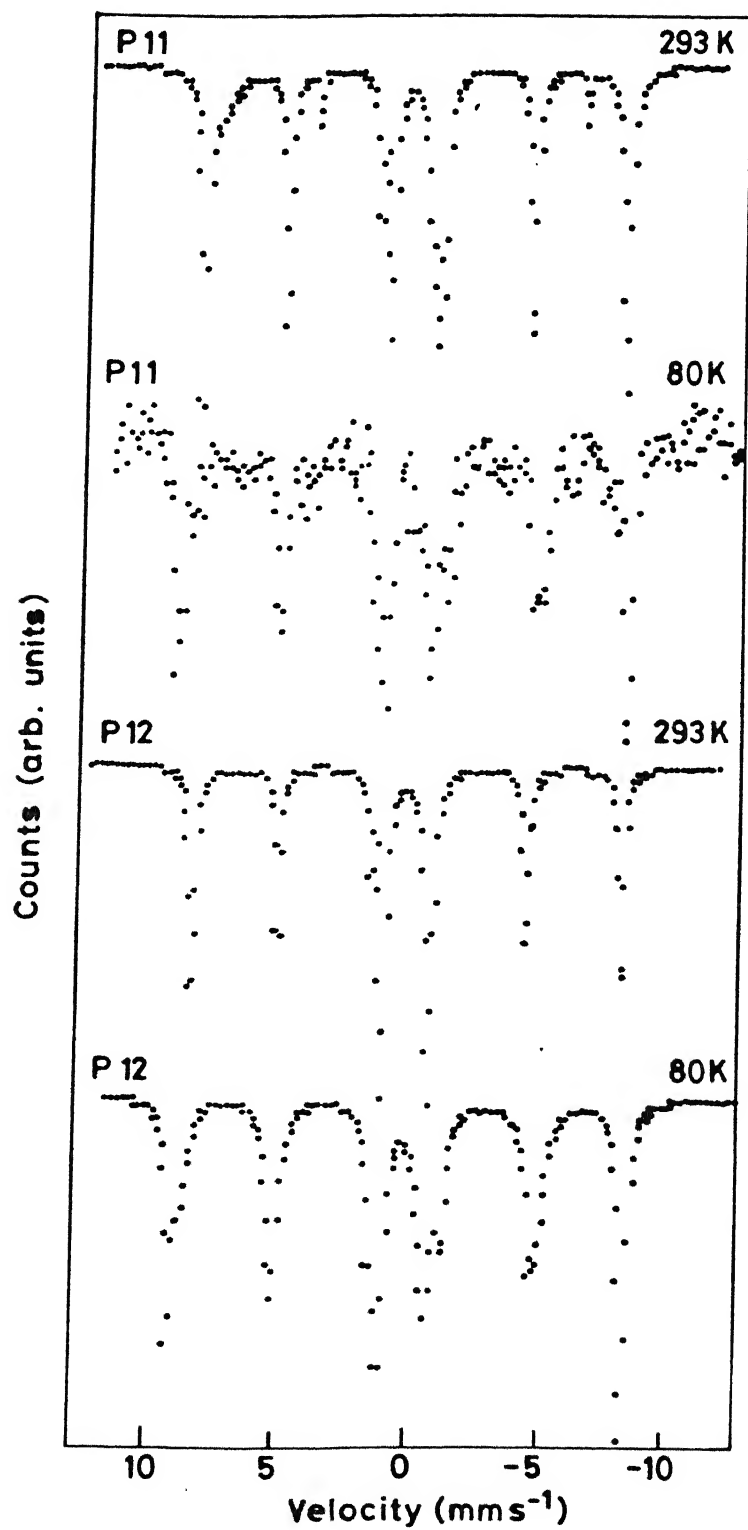


Fig.3.10 Mössbauer spectra of P11, P12 at 80 and 293K.

the amorphous nature of PbM (short range order in PbM). The other structure observed in the Mössbauer spectrum of P11 is not fully developed and it might be due to the weak contribution arising from the partial crystallization of the five magnetic sublattices of PbM. All this behaviour could be due to the possibility that the temperatures employed in the heat-treatment of P11 are too low for a proper nucleation and crystallization to occur and this might give rise to amorphous nature and poor formation of PbM observed here.

The Mössbauer spectrum of the sample P12 shows the presence of $\alpha\text{-Fe}_2\text{O}_3$ and the doublet (seen in sample P11). However no other structure is observed, although the nucleation and crystallization temperatures are higher than those used for the sample P11 (Table 3.8). The Mössbauer parameters obtained for the sample P12 are given in Table 3.12. We see that the values for IS, ΔE and Γ observed for the doublet spectrum in sample P12 are not much different from those observed for the sample P11. It may be added that we measured the Mössbauer spectra for the samples P11 and P12 at 80 K also and the observed Mössbauer parameters are given in Table 3.12. No additional information or interpretation was available from these measurements made at 80 K. We, therefore, feel that the temperature used by us in the heat-treatment of the samples P11 and P12 are not the most appropriate for efficient crystallization of PbM for the glass composition used by us.

3.4 SUMMARY AND CONCLUSIONS

In this section we shall summarise the results presented earlier in this Chapter and shall put forth the important conclusions arising out of our work. For the sake of convenience we shall divide our discussion by summarising the study of YIG systems in sodium silicate glasses first and the study of hexagonal ferrites in borate glasses next.

The main aim of our study of sodium silicate glasses was to examine the precipitation of the magnetic YIG phase in these glasses particularly in relation to three factors (i) their composition, (ii) nucleating agent and (iii) the heat-treatment given. Our studies have shown that each of these factors affects the precipitation of the magnetic phase with accompanying changes which can be studied by Mössbauer spectroscopy. In the case of samples C10, C11 and C12 (composition ^{by wt} 48% SiO₂, 26% Na₂O, 9% Y₂O₃, 15% Fe₂O₃ and 2% Bi₂O₃), the heat-treatment results in the crystallization of the magnetic phase due to α -Fe₂O₃. The amount of YIG phase, as observed by our Mössbauer studies, was not significant although the X-ray diffraction studies indicated that the amount of the YIG phase in the sample C11 was small while in the sample C12 it was fairly large. Such differences in the estimation of volume elements of different compounds as observed by Mössbauer spectroscopy and by X-ray diffraction studies are known

to occur [60]. These differences arise out of the different sensitivities of the two techniques with regard to the nature of samples used (i.e. thickness and method of preparation of the samples, surface or bulk characterization probed by each technique etc.). Although the schedule of heat-treatment for the samples C11 and C12 was different in respect of the time period for nucleation stage, the Mössbauer spectra and the resulting parameters did not show any change in going from C11 to C12. We thus conclude that for this composition (series C1), the heat-treatment given by us does not lead to significant precipitation of the YIG phase in the sodium silicate glasses.

Considering the results for the samples C20, C21 and C22 (having the composition ^{by wt} 49.6% SiO₂, 33.6% Na₂O, 5.9% Y₂O₃, 10.1% Fe₂O₃, 0.8% Bi₂O₃) we see that their general behaviour is similar to the samples C10, C11 and C12 in that only the magnetic phase due to α -Fe₂O₃ is precipitated in a significant manner after the heat-treatment is given.

The sample C41 has the composition ^{by wt} 48% SiO₂, 26% Na₂O, 9% Y₂O₃, 17% Fe₂O₃ and a small (0.5 wt %) amount of Pd (which acts as a nucleating agent). We did not observe any precipitation of the YIG phase and only α -Fe₂O₃ was precipitated after the heat-treatment given (Table 3.2). A comparison of the samples of series C1, C2 and C4 shows that changing the composition and the nucleating agent

from Bi_2O_3 to Pd does not bring in the precipitation of the YIG phase. It may be pointed out that we have raised the time period of the crystallization stage from 2h to 24h in going from the sample C21 to C22. Yet this heat-treatment has not helped to precipitate the YIG phase. We, therefore, conclude that the composition and nucleating agent chosen for the samples belonging to the series C1, C2 and C4 is not appropriate enough for the precipitation of the YIG magnetic phase in these sodium silicate glasses. There is, however, a change in the magnetization (M_s) measured for these samples and the values of M_s observed [18] with C11: $M_s = 0.3$ (emu/gm), C12 : 0.3 (emu/gm), C22 = 6.0 (emu/gm) and C41 = 2.0 (emu/gm). Precipitation of the YIG phase has, however, been observed in some of the samples belonging to the C3 series having a composition ^{by wt} 48% SiO_2 , 26% Na_2O , 9% Y_2O_3 , 16% Fe_2O_3 , 0.5% Ag_2O and 0.5% As_2O_3 with the ($\text{Ag}_2\text{O} + \text{As}_2\text{O}_3$) acting as nucleating agents. As a result of the heat-treatment the samples C31, C32 and C33 showed a behaviour much different from those belonging to the series C1, C2 and C4. The sample C31 showed a weak amount of the YIG phase being precipitated after the heat-treatment. The low intensity of these lines did not allow us a satisfactory analysis of the Mössbauer spectra observed for the sample C31. In going from the sample C31 to C32, the nucleating temperature was raised from 555K to 865 K and the crystallization temperature was raised from

555 to 905 K and this resulted in an increase in the amount of the YIG phase being precipitated. However the amount of YIG phase seen in the sample C32 was still not large enough as observed in the Mössbauer spectra. Only when the nucleating and crystallization temperatures were raised to 1000 K and 1095 K respectively for the sample C33, could we observe a sizable amount of the YIG phase being precipitated. The spectral lines due to α -Fe₂O₃ and Si-substituted YIG could be separated in the Mössbauer spectrum of C33 in a clear manner. The analysis of the Mössbauer parameters for the sample C33 has helped us to assign the observed spectra to the different sites (d, a' and a) of the magnetic sublattices in the Si-substituted YIG phase. Closer examination of the Mössbauer parameters have further enabled us to compare the results for the Mössbauer spectra of Si-substituted YIG and pure YIG and has allowed us to explain the observed differences in terms of the effects arising out of the substitution of Si in YIG. It can be concluded, on the basis of these observations that the characteristics of Si-substituted YIG are different from those of pure YIG. This conclusion is supported by other studies reported by other workers [26-28].

The studies of the present samples carried out by the EPR and optical spectroscopy techniques support our results of Mössbauer spectroscopy. Thus the EPR spectrum of the sample C33 showed a sharper spectrum indicating

the precipitation of YIG in a larger amount. The optical spectra observed for C33 showed a distinctly different character for the Fe^{3+} ions at tetrahedral and octahedral sites. The difference in the intensities arising from Fe^{3+} ions at these two sites have been explained in terms of the increase in the $\text{Fe}^{3+} - \text{Si}^{4+}$ bond length (which arises from the smallness of the radius of Si^{4+} and its larger change).

We now summarize the results of borate glass systems in which hexagonal ferrites (BaM, SrM and PbM) were precipitated. Let us first consider the system $35\text{BaO}-40\text{B}_2\text{O}_3-25\text{Fe}_2\text{O}_3$ in which BaM was precipitated after giving suitable heat-treatment to the as-prepared (as-quenched) glass sample. The sample B11 which was given a heat-treatment schedule 850 K/2h (nucleation temperature) followed by 895 K/20h (crystallization temperature) showed the precipitation of the two phases : $\alpha\text{-Fe}_2\text{O}_3$ and BaM. The Mössbauer spectrum of the sample B11 showed a six-line spectrum due to $\alpha\text{-Fe}_2\text{O}_3$ and four other six-line spectra (sextets) attributed to five magnetic sublattices of BaM. The observed values of H_{int} for different sublattices of BaM were found to be lower and this reduction has been ascribed to the nature of small particles precipitated in B11. In going from the sample B11 to B12, B13 and B14, the heat-treatment schedule was altered (Table 3.8) and this led to changes in the precipitation of $\alpha\text{-Fe}_2\text{O}_3$

and BaM phases which could be observed by Mössbauer spectroscopy. Thus we found in the case of B12 that the particle size of BaM was enhanced giving rise to a clearer resolution between the Mössbauer spectra due to different sublattices. The amount of $\alpha\text{-Fe}_2\text{O}_3$ precipitated was more in the sample B12 but was less in the samples B13 and B14. Taking an overall view of the results for the samples B11, B12, B13, B14, B15 and B16, we summarize that in $35\text{BaO-}40\text{B}_2\text{O}_3\text{-}25\text{Fe}_2\text{O}_3$ systems the choice of nucleation temperature 850 K and crystallization temperature 1065 K is optimum for the precipitation of BaM (as far as the control of particle size and volume fraction of BaM is concerned).

Let us now consider the $35\text{SrO-}40\text{B}_2\text{O}_3\text{-}25\text{Fe}_2\text{O}_3$ system of which the heat-treated sample S11 and S12 were studied by us. The present Mössbauer spectroscopic studies have shown that the heat-treatment schedule given to the sample S11 resulted in the precipitation of the $\alpha\text{-Fe}_2\text{O}_3$ and SrM phases, the latter giving rise to the spectra due to the five magnetic sublattices. In the case of the sample S12 additional magnetic phases $\text{Sr}_3\text{Fe}_2\text{O}_{6.9}$ and perhaps $\text{Sr}_3\text{Fe}_2\text{O}_{6.2}$ were also precipitated as a result of the higher nucleation and crystallization temperatures. Comparing the results of the samples S11 and S12 we feel that for the composition $35\text{SrO-}40\text{B}_2\text{O}_3\text{-}25\text{Fe}_2\text{O}_3$ the heat-treatment schedule involved in S11 is more preferable for the clear-cut growth of the SrM phase. Although the volume fraction of the $\alpha\text{-Fe}_2\text{O}_3$

phase is somewhat larger in the case of sample S11, compared to S12 it is relatively free from the growth of other magnetic phases. A change of the composition to $47\text{SrO}-28\text{B}_2\text{O}_3-25\text{Fe}_2\text{O}_3$ (sample S20 and S21) does not seem to improve the matter. Perhaps this choice of the composition and the heat-treatment chosen by us was not the most appropriate. In summary, a comparison among the samples S11, S12 and S21 the composition and heat-treatment involved in the sample S11 appears to be optimum for the growth of the SrM phase.

In the case of the system $50\text{PbO}-30\text{B}_2\text{O}_3-20\text{Fe}_2\text{O}_3$, we have tried only two heat-treatments as given to the samples P11 and P12. Somehow for this composition and these heat-treatments the yield of crystalline PbM appears to be very low. Some other composition involving different heat-treatments should be investigated to find out the optimum combination for good growth of crystalline PbM phase.

REFERENCES

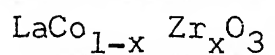
1. P.W. McMillan, 'Glass Ceramics', (Academic Press, London-New York, 1964).
2. A.I. Bereznoi, 'Glass Ceramics and Photo Sitalis', (Plenum Press, New York-London, 1970).
3. M. Tashiro, S. Sakka and T. Kokubo, J. Ceramic Assoc. Jpn. 72, 20 (1964).
4. R.R. Shaw and J.H. Heasley, J. Am. Ceram. Soc. 50, 297 (1967).
5. T. Komatsu, N. Soga and M. Kunugi, J. Appl. Phys. 50, 6469 (1979).
6. Akhilesh Prasad, D. Bahadur, R.M. Singru and D. Chakravorty, J. Mater. Sci. 17, 2687 (1982).
7. B.T. Shirk and W.R. Buessem, J. Am. Ceram. Soc. 53, 192 (1970).
8. W.J.S. Blackburn and B.P. Tilley, J. Mater. Sci. 9, 1265 (1974).
9. W.H. Von Aulock (Ed.), Handbook of Microwave Ferrite Materials (Academic Press, New York-London, 1965).
10. E.P. Wohlforth (Ed.) Ferromagnetic Materials, Vol 2 (North-Holland Publishing Co. Amsterdam, 1980).
11. R. Schulte , H. Schieder, F.J. Literstand and G.M. Kalvius, Nucl. Inst. and Methods, 199, 343 (1982).
12. D. Bahadur and D. Roy , International Conference of Ferrite, San-Fransisco, USA, Nov. 1984.

13. M. Eibschutz, M.E. Lines and K. Nasu, Phys. Rev. B22, 3767 (1980).
14. E. Sawatzky and E. Kay, J. Appl. Phys. 39, 4700 (1968).
15. D.W. Johnson and F.J. Schnettler, J. Am. Ceram. Soc. 53, 440 (1970).
16. Th. J.A. Popma and A.M. Von Diepen, Mater. Res. Bull. 9, 119 (1974).
17. D. Roy, R. Bhatnagar and D. Bahadur, J. Mater. Sci. 20, 157 (1985).
18. S. Ram and D. Bahadur (Private Communication); also D. Bahadur, D. Chakravorty, D. Chattopadhyaya, S. Datta, S.K. Khan, S. Mitra, S. Ram, D. Roy and K. Sengupta, J. Mater. Sci. 21, 2793 (1986).
19. C.R. Kurkjian and E.A. Sigety, Phys. Chem. Glasses 9, 73 (1968).
20. T. Komatsu and N. Soga, J. Appl. Phys. 51, 601 (1980).
21. T. Nishida, N. Kai and Y. Takashima, Phys. Chem. Glasses 22, 107 (1981).
22. B. Window, J. Phys. E4, 401 (1971).
23. M. Eibschutz, M.E. Lines, L.G. Van Uitert, H.J. Guggenheim and G.J. Zyzdik, Phys. Rev. B24, 2343 (1981).
24. Pushan Ayyub, Manu Mulani and R. Vijaya Raghavan, Phys. Lett. A119, 95 (1986).

25. N.N. Greenwood and T.C. Gibb, 'Mössbauer spectroscopy' Chapman and Hall Ltd., London (1971), we checked the values of the Mössbauer parameters for $\alpha\text{-Fe}_2\text{O}_3$ independently by using standard $\alpha\text{-Fe}_2\text{O}_3$ absorber (R35092) supplied by Amersham International PLC. U.K.
26. J.J. Van Loef, J. Appl. Phys. 39, 1258 (1968).
27. I.S. Lyubutin, L.M. Bilyaev, S. Yu. Vishnyakov, T.V. Dmitrieva, A.P. Dodokin, V. Ya. Dubossarskaya and L.P. Shlyakhina, Soviet Phys. JETP 31, 647 (1970).
28. T.J.A. Popma, A.M. Van Diepen and P.F. Bongers, J. Phys. Chem. Solid, 35, 201 (1974).
29. R.M. Housley, 'Magnetism and Magnetic Materials', AIP Conf. Proc. 24, 374 (1975).
30. B. Antonini, S. Geller, P. Paroli, A. Tucciarone and A.A. Colville, Appl. Phys. Lett. 27, 700 (1975).
31. S. Geller and G. Balestrino, Solid State Commun. 33, 315 (1980).
32. G. Balestrino, S. Geller, W. Tolksdorf and P. Willich, Phys. Rev. B22, 2282 (1980).
33. Czeslaw Rudowicz, Z. Naturforsch 39a, 605 (1984).
34. T. Komtsu and N. Soga, J. Mat. Sci. 19, 2353 (1984).
35. K.J. Rao and B.G. Rao, Proc. Ind. Acad. Sci. 95, 169 (1985).
36. A.M. Clogston, J. Appl. Phys. 31, 1985 (1960).
37. K.A. Wickersheim and R.A. Lefever, J. Chem. Phys. 36, 844 (1962).

38. D.L. Wood and J.P. Remeika, J. Appl. Phys. 38, 1038 (1967).
39. J.F. Dillon, Jr., E.M. Gyorgy and J.P. Remeika, J. Appl. Phys. 41, 1211 (1970).
40. D.K. Sarkar, M.D. Shinn and W.A. Sibley, Phys. Rev. 26B, 2382 (1982).
41. J.J. Went, G.W. Rathenau, E.W. Gorter and G.W. Van Oosterhout, Phillips Techn. Rev. 13, 194 (1952).
42. H. Fahlenbrach and W. Heister, Arch. Eisenhüttenw 29, 523 (1953).
43. T. Fujiwara, IEEE Trans. Mag. MAG-21, 1480 (1985).
44. S. Ram, D. Bahadur and D. Chakravorty, Proc. XIV Int. Congress on Glass held at New Delhi, India (a special publication of Indian Ceramic Society), 1, 336 (1986).
45. S. Ram, D. Bahadur and D. Chakravorty, J. Non-Cryst. Solids 88, 311 (1986).
46. M.J. Tricker, J.M. Thomas, M.H. Omar, A. Osman and A. Bishay, J. Mater. Sci. 9, 1115 (1974).
47. E. Burzo and Doira Ungur, Mat. Res. Bull. 17, 935 (1982).
48. T. Nishida, T. Shiotsuki and Y. Takashima, J. Non-Cryst. Solids 43, 115 (1981).
49. J.S. Van Wieringen, Phillips Tech. Rev. 28, 33 (1967).
50. J.J. Van Loef and A.B. Van Groenou, Proc. Int. Conf. Magn. Nottingham 646 (1964).
51. J.J. Van Loef and P.J.M. Franssen, Phys. Lett. 7, 225 (1963).

52. E. Kreber, U. Gonser, A. Trautwein and F.E. Harris, J. Phys. Chem. Solids 36, 263 (1975).
53. H. Kojima, ''Ferromagnetic Materials'' Ed. E.D. Wohlforth North-Holland Publishing Company CH5, 3.305 (1982).
54. I.G. Rensen and I.S. Van Wieringen, Solid State Commun. 1, 1139 (1969).
55. J. Beretka and M.J. Ridge, J. Chem. Soc. A3, 2463 (1968).
56. H.H. Wickman and C.F. Wagner, J. Chem. Phys. 51, 435 (1969).
57. V.F. Belov, T.A. Khimich, M.N. Shipko, I.S. Zheludev, E.V. Korneev and N.S. Ovanesyan, Sov. Phys. JETP, 37, 1089 (1974).
58. P.K. Galaghev, J.B. Machesney and D.N.E. Buchanan, J. Chem. Phys. 41, 2429 (1964).
59. P.K. Galaghev, J.B. Machesney and D.N.E. Buchanan, J. Chem. Phys. 45, 2466 (1966).
60. Akhilesh Prasad, Virendra Kumar, R.M. Singru and T.R. Ramachandran (Unpublished data).

MÖSSBAUER AND OTHER STUDIES OF

4.1 INTRODUCTION

The fundamental problem in the study of transition metal oxides is to find an adequate description of their outer atomic electrons so that the rich variety of their physical properties could be explained satisfactorily. It is well-known that when atoms are brought together to form a crystal, the spin and valence states of the atoms and the degree of the overlapping of different atomic orbitals within the crystalline array determine the properties of the crystal. Two limiting theories exist for describing the state of outer electrons of atoms in the crystal. In one, the outer electrons are assumed to be localized at specific atomic sites and the states of electrons are described by the crystal field theory. In the other, the outer electrons are assumed to be collective, belonging to the crystal as a whole and are described by the band theory. The outer s and p orbitals of neighbouring atoms in a crystal overlap one another sufficiently to ensure a collective-electron behaviour. The electrons in these s and p orbitals are responsible for the binding energy of the crystal. The outer f electrons, on the

other hand, are tightly bound to the atomic nucleus and are largely screened from the neighbouring atoms by the core s and p electrons of larger principal quantum number. The outer f electrons, however, are always described by a localized-electron theory. The outer d electrons are intermediate, sometimes treated as collective and sometimes as localized. As a combination of all these effects, the transition metal compounds possess a rich variety of physical properties and they form a subject of several interesting studies.

In view of the above, the compounds TaF_3 , MoF_3 , WO_3 etc. having ReO_3 structure (where the ReO_3 structure consists of a simple cubic cation sublattice with anion at the center of the cube) and LaCoO_3 , SrFeO_3 , BaTiO_3 etc. having the cubic perovskite structure (in the perovskite structure the body center position is occupied by a large cation) have been investigated extensively by using different experimental techniques.

Among these perovskite oxides, LaCoO_3 has been a subject of extensive research [1-6] because of its interesting electrical and magnetic properties. Along with LaCoO_3 , the substituted LaCoO_3 , where different transition metal atoms have been substituted at the La site as well as at the Co site, have been investigated by several workers [7-18]. In our laboratory previous work has

been reported about EuCoO_3 , YCoO_3 , ErCoO_3 and $\text{La}_{1-x}\text{Sr}_x\text{CoO}_3$ [9-11] and about $\text{La}_{1-x}\text{Sr}_x\text{Co}_{1-y}\text{Ti}_y\text{O}_3$ [17]. We have extended this work to the system $\text{LaCo}_{1-x}\text{M}_x\text{O}_3$ where $\text{M} = \text{Zr}$ and $x = 0.1, 0.3$ and 0.5 by means of Mössbauer spectroscopy and magnetic susceptibility measurements with an aim of observing the effect of 4d transition metal elements on LaCoO_3 . These results of our present work are being reported in this Chapter and they will be discussed by comparing them with the results for LaCoO_3 and substituted LaCoO_3 .

It is known [2-4] that the transition metal oxides with low cationic spin ($s \leq 1/2$) exhibit metallic conductivity and Pauli paramagnetism. The d electrons in these oxides are treated as collective and are well described by band theory (e.g. LaTiO_3 and LaNiO_3). On the other hand, transition metal oxides with high cationic spin ($s \geq 2$) carry a spontaneous atomic moment that gives rise to a predictable temperature dependent magnetic susceptibility at higher temperatures and a magnetic order below a magnetic ordering temperature and the d-electrons in these oxides are treated as localized and their atomic moment is described by crystal field theory (e.g. LaCrO_3 , LaMnO_3 and LaFeO_3) [3-4]. In these cases the compounds having $s = 2$ exhibit Jahn-Teller distortion. The spin-state of transition metal ion in the compound is essentially

determined by two factors : (i) the crystal field splitting Δ_{cf} and (ii) the exchange energy Δ_{ex} . If $\Delta_{cf} > \Delta_{ex}$ the low-spin state of the transition metal ion becomes the stable state as in WO_3 , $LaTiO_3$, $CaVO_3$ and $ZnCO_2O_4$ [1-4]. On the other hand, the high spin state becomes energetically more stable if $\Delta_{cf} < \Delta_{ex}$ as in the case of $LaCrO_3$ and $LaMnO_3$ [1-4,19]. If $\Delta_{cf} \approx \Delta_{ex}$ both the low-spin as well as the high-spin states of transition metal ions can coexist as in the case of $LaCoO_3$ [3-4].

Properties exhibited by the $LaCoO_3$ system have been studied in detail by Raccach and Goodenough [1-4]. The variation in the slope of the inverse magnetic susceptibility versus temperature plot was explained by these workers as due to the variation of relative population of the low-spin and high-spin cobalt ions. Similarly it was proposed that the observed plateau in the inverse susceptibility versus temperature curve arose out of the short range order. This proposed short range order is also supported by DTA and other measurements. The symmetry of $LaCoO_3$ is observed to change from $\overline{R3c}$ to $\overline{R3}$ following the short range ordering. The first order transition arising out of the delocalization of the e_g electrons (localized at the lower temperature at high-spin Co^{3+} ion) to form σ^* band electrons at 1210 K was observed. The compound $LaCoO_3$ becomes metallic at 1210 K and all Co^{3+}

ions transfer to form a σ^* band. The electron transport properties of LaCoO_3 were explained in terms of temperature variation of the spin and valence state equilibria of cobalt ion. It was further interpreted that the $e_g \rightarrow \sigma^*$ transition could indicate that the crystal field and band limits of d electrons are two distinct thermodynamic states. The mechanism for the electrical conduction in LaCoO_3 assumed the formation of high-spin divalent and low-spin tetravalent cobalt ion pairs.

Mössbauer studies on the rare earth cobaltates carried out in our laboratory previously [9-11, 17] in the temperature range (78-1200 K) have shown how Mössbauer spectroscopy can be a valuable technique to study the spin-state equilibria in these cobaltates. The main advantage arises because one can prepare the source by thermally diffusing radioactive ^{57}Co into the cobaltates and then perform Mössbauer spectroscopic studies using the 14.4 keV Mössbauer gamma-ray in ^{57}Fe . In the case of EuCoO_3 one could also perform ^{151}Eu Mössbauer studies.

Previous results of Mössbauer spectroscopic studies on EuCoO_3 along with magnetic susceptibility, differential thermal analysis (DTA), X-ray diffraction and electrical resistivity data have shown that cobalt ions exist predominantly in the low-spin $\text{Co}^{\text{III}} (t_{2g}^6 e_g^0)$ state at low temperatures and partially transform to the high-spin $\text{Co}^{3+} (t_{2g}^4 e_g^2)$ state upto 350 K. Above this temperature

there is electron transfer from Co^{3+} to Co^{III} to produce di- and tetra-valent cobalt ions. There is ordering of cobalt ions in the 500-700 K range but at high temperature the Co^{3+} population decreases significantly and completely disappears at the localised-itinerant electron ($e_g \rightarrow \sigma^*$) transition temperature (1180 K).

Similar studies on YCoO_3 have shown that its properties are similar to LaCoO_3 and that there is considerable electron transfer from Co^{3+} to Co^{III} giving rise to charge-transfer states. However ErCoO_3 was found to be similar to HoCoO_3 showing no evidence of electron transfer and the ratio of Co^{3+} to Co^{III} is essentially constant over the entire temperature range studied.

The system $\text{La}_{1-x}\text{Sr}_x\text{CoO}_3$ has similarly been studied for $0 < x \leq 0.50$. It becomes ferromagnetic for $x > 0.125$ and when $x = 0.5$, it is metallic. The Mössbauer and other studies [9] have shown that in $\text{La}_{1-x}\text{Sr}_x\text{CoO}_3$ ($x > 0.125$), ferromagnetic Sr^{2+} -rich clusters coexist with paramagnetic La^{3+} -rich regions both being in the same crystallographic phase. The ferromagnetic component increases with increasing x and decreasing T . The $3d$ -holes created by Sr^{2+} substitution are itinerant both above and below the curie temperature.

Above work was further extended in our laboratory by investigating the system $\text{La}_{1-x}\text{Sr}_x\text{Co}_{1-y}\text{Ti}_y\text{O}_3$ for (a) $x = 0$ and (b) $x = y$ by Mössbauer spectroscopic measurements

carried out between 77 and 800 K. Such systems are of interest from the point of view of existence of itinerant electron ferromagnetism. It was observed that none of the Mössbauer spectra shows hyperfine splitting even at 77 K and it was explained as the effect of the Ti^{4+} substitution which restricts the generation of Co^{4+} (which is mainly responsible for itinerant electron ferromagnetism in $La_{1-x}Sr_xCoO_3$). The variation of the isomer shift and other data with temperature was discussed in the framework of spin-state and valence-state equilibria of cobalt ions in these materials.

In our Institute the substituted perovskite systems (a) $LaCo_{1-x}Zr_xO_3$ with $x = 0.1, 0.3$ and 0.5 have been prepared by D. Bahadur who has also studied the X-ray diffraction spectra and magnetic susceptibility measurements [19]. These results indicated that the spin-state and valence equilibria in these systems can be interesting. We, therefore, decided to study these systems using Mössbauer spectroscopy. With this aim in mind samples of above substituted perovskite systems were prepared and radioactive ^{57}Co was deposited in them. Mössbauer spectra, using such samples as sources and stainless steel (SS 310) and potassium ferrocyanide (PFC) were recorded at 80, 293, 500 and 700 K temperatures. In the following section we give details of these measurements followed by the discussion of the results.

4.2 EXPERIMENTAL

We now report out studies of the substituted perovskite system $\text{LaCo}_{1-x}\text{Zr}_x\text{O}_3$ with $x = 0.1, 0.3$ and 0.5 . Various experimental techniques such as X-ray diffraction, magnetic susceptibility measurements and Mössbauer spectroscopy have been used to investigate the above substituted perovskite systems. Among these techniques the Mössbauer spectroscopic studies are particularly useful because they help us to understand the spin- and valence-state equilibria in these compounds.

4.2.1 Preparation of the Cobaltates

Samples of $\text{LaCo}_{1-x}\text{Zr}_x\text{O}_3$ for various values of x were prepared by ceramic method wherein a mixture of appropriate amount of oxalates having high purity constituent elements was ground in a ball mill. The ground mixture of oxalates was decomposed at 1050 K. The decomposed material was again ground, made into pellets and sintered for 12 hours in air at 1500 K. The mixing and sintering was repeated and X-ray diffraction data were taken at each stage to monitor the completion of reaction. Chemical analysis of $\text{LaCo}_{1-x}\text{Zr}_x\text{O}_3$ showed that the sample is nearly stoichiometric for $x = 0.1$. However the samples having other values of x were not found to be stoichiometric.

4.2.2 Measurement of X-ray and Magnetic Susceptibility

The X-ray diffraction measurements were carried out using Rich-Seifert X-ray diffractometer with $\text{CuK}\alpha$ radiation. The X-ray patterns of $\text{LaCo}_{1-x}\text{Zr}_x\text{O}_3$ compounds were indexed on a hexagonal as well as on a rhombohedral basis. The results of this analysis are presented in Table 4.1 and they show that the compound $\text{LaCo}_{1-x}\text{Zr}_x\text{O}_3$ has rhombohedral structure when $x = 0.1$. In the case of $x = 0.3$ and 0.5 both the compounds show cubic perovskite structure accompanied by a change in cell dimensions. This change in cell dimensions can be understood because substitution of small radius of Co^{3+} (0.525 \AA) by larger radius of Zr^{4+} (0.79 \AA).

Magnetization measurements were carried out with a PAR vibrating sample magnetometer (model 1500 A) in conjunction with a Varian 9" magnet (model V - 7200). The results of these measurements will be presented in the next section.

4.2.3 Mössbauer Spectroscopic Measurements

We carried out ^{57}Fe Mössbauer spectroscopic measurements using $\text{La}^{57}\text{Co}_{1-x}\text{Zr}_x\text{O}_3$ as Mössbauer source and 316 stainless steel (316 SS) or ^{57}Fe -enriched potassium ferrocyanide (PFC) absorber. The actual absorber used in a particular measurement will be specified later. To

Table 4.1 : Lattice parameters (measured at 293 K) for
 $\text{LaCo}_{1-x}\text{Zr}_x\text{O}_3$.

Composition x	a (Å)	α (degrees)	Structure
0.1	5.410	60.53	Perovskite with rhombohedral structure
0.3	5.510	—	Cubic
0.5	5.580	—	Cubic

prepare the $\text{La}^{57}\text{Co}_{1-x}\text{Zr}_x\text{O}_3$ Mössbauer source, 1.0-1.5 mm thick pellets of diameter 12-14 mm were made and $^{57}\text{CoCl}_2$ (radioactive) aqueous solution was added to every pellet drop by drop. Each drop was allowed to be deposited and dried by heating the pellet under infrared lamp and only after the drop had dried was the next drop put. These pellets were then heated in air at 1450 K for 12 hours to allow ^{57}Co to diffuse into the pellets. The pellets were then slowly cooled to room temperature. The surface of the pellet was then gently polished to remove any undiffused radioactivity. Transmission Mössbauer spectra of different $\text{La}^{57}\text{Co}_{1-x}\text{Zr}_x\text{O}_3$ Mössbauer sources were taken with the help of the Mössbauer spectrometer (already described in Chapter 2) in the constant acceleration mode. The spectra were recorded at 80, 293, 500 and 700 K. The Mössbauer spectrometer was calibrated using $\alpha\text{-Fe}$ foil as an absorber and the IS was measured with respect to ^{57}Fe at room temperature.

4.3 RESULTS AND DISCUSSION

In this section we shall present our results on the system $\text{LaCo}_{1-x}\text{Zr}_x\text{O}_3$ ($x = 0.1, 0.3$ and 0.5) using the magnetization and Mössbauer spectroscopic studies.

Magnetic Susceptibility Measurements

The magnetic susceptibility (χ_g) of the $\text{LaCo}_{1-x}\text{Zr}_x\text{O}_3$ ($x = 0.1, 0.3$ and 0.5) samples was measured in the temperature range 300-800 K. The $1/\chi_g - T$ plots of $\text{LaCo}_{1-x}\text{Zr}_x\text{O}_3$ for $x = 0.1, 0.3$ and 0.5 are shown in Fig. 4.1a. It is observed that the $1/\chi_g - T$ curve for $x = 0.1$ shows a kink and its shape is different from the curves for $x = 0.3$ and 0.5 . The plot for $x = 0.1$ shows two linear parts (on either side of the kink) which have different slopes. The linear part in the lower (300-400 K) temperature interval has a larger slope which indicates a lower μ_{eff} relative to the higher (575-800 K) temperature interval. This behaviour is consistent with the observed in the case of LaCoO_3 [2-5]. In the case of $x = 0.3$ and 0.5 samples, the presence of a plateau in the $1/\chi_g - T$ curve is more clearly seen, with the plateau occurring in the temperature intervals 425-500 K (for $x = 0.3$) and 450-550 K (for $x = 0.5$). Similar existence of a plateau separating the two linear parts has been observed in the $1/\chi_g - T$ plots for the $\text{MnAs}_{1-x}\text{P}_x$ [2] and LaCoO_3 [3-5] systems. In our case the slopes of the two linear parts are different (Fig. 4.1a) and the slope of the linear part for $x = 0.3$ and 0.5 is lower in the low temperature range. This behaviour suggests a higher value of μ_{eff} at lower temperature for $x = 0.3$ and 0.5 .

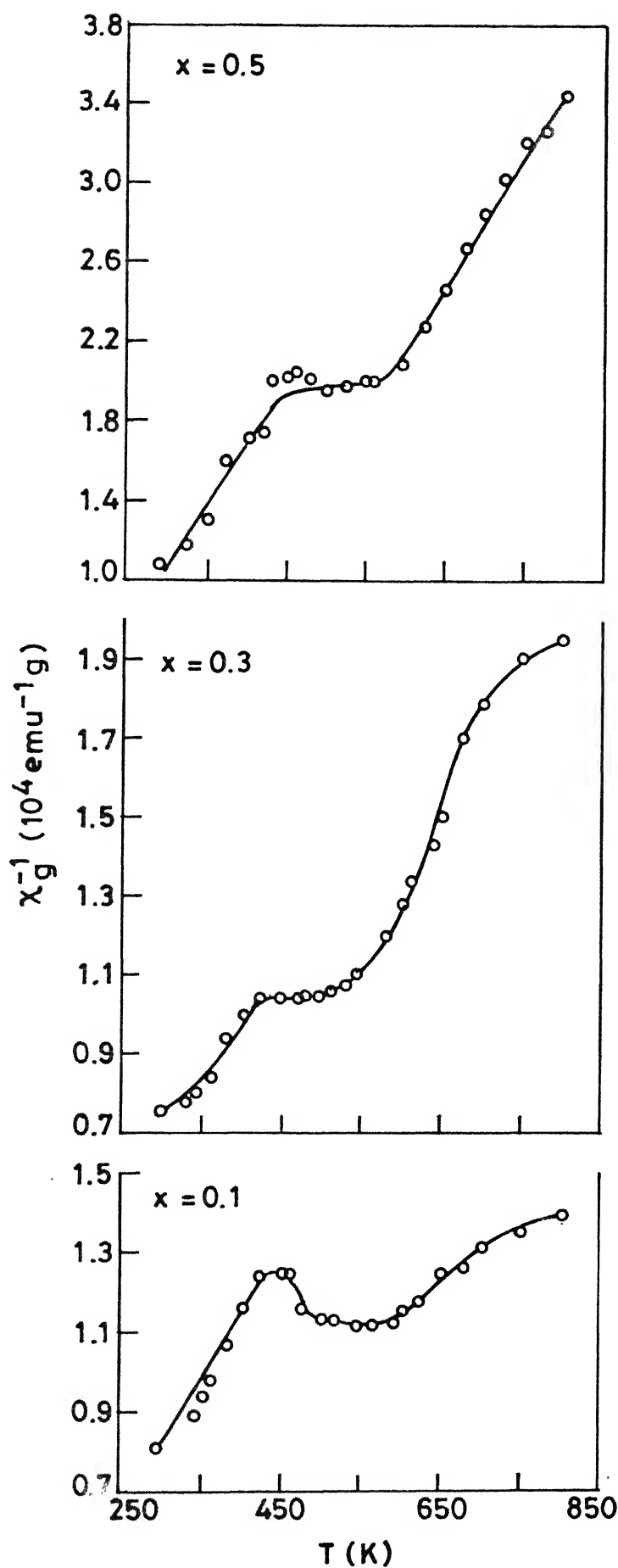
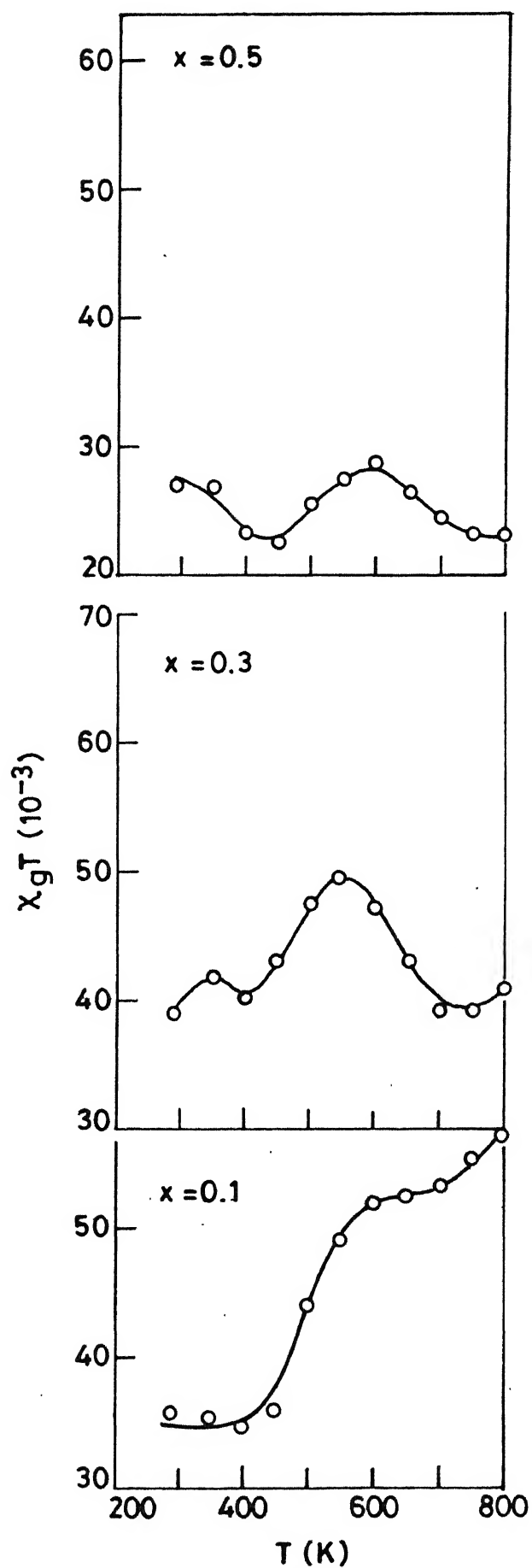


Fig.1(a) Inverse magnetic susceptibility per gram against temp. for $\text{LaCo}_{1-x}\text{Zr}_x\text{O}_3$.



(b) Plot of $\chi_g T$ against temp. for $\text{LaCo}_{1-x}\text{Zr}_x\text{O}_3$

We therefore propose that in $\text{LaCo}_{1-x}\text{Zr}_x\text{O}_3$ having $x = 0.3$ and 0.5 , Co^{2+} ions are produced at higher temperatures and that these ions having a lower value of μ_{eff} relative to Co^{3+} and Co^{4+} cause the above behaviour. Later we shall show that the Mössbauer spectroscopic data support this proposal.

Following Bhide et al. [5-6] we have examined the variation of $\chi_g T$ versus T (Fig. 4.1b) for $x = 0.1, 0.3$ and 0.5 with an aim to get a better insight into the variation of low : high spin ions. Generally, for a paramagnetic substance $\chi_g T$ does not vary with temperature because

$$\chi_g T = \frac{N \mu^2}{3R} = \text{constant} \quad (4.1)$$

where N is the Avogadro number and μ is the effective spin-only magnetic moment of the paramagnetic ions.

For the case when the population of paramagnetic ions varies with temperature, the product $\chi_g T$ will change with temperature depending on the ratio of the population of paramagnetic and diamagnetic ions and

$$\chi_g T = \frac{N \mu^2}{3R} \cdot \frac{n}{n + m} \quad (4.2)$$

where n and m represent the population of paramagnetic and diamagnetic ions respectively. Equation (4.2) can be written as

$$\frac{n}{m} = -1 / \left(\frac{N^2 \mu^2}{3R \chi_g T} - 1 \right) \quad (4.3)$$

It is thus clear that the variation of $\chi_g T$ with T provides information about the transformation of the spin-states. When studied in this light, the results for $x = 0.1$ as shown in Fig. 4.1b, show that the ratio n/m remains constant in the temperature range 300-400 K. The relative population of the paramagnetic ions increases rapidly between 400 and 550 K but it increases slowly beyond 550 K. The observed behaviour of the $\chi_g T$ versus T curve for $x = 0.3$ and 0.5 (Fig. 4.2b) is much different from that for $x = 0.1$. This difference is ascribed to the effect of the substitution of the more Zr^{4+} ions occurring at the higher x -values.

Mössbauer spectroscopic studies

Before we discuss our results for $LaCo_{1-x}Zr_xO_3$ using Mössbauer spectroscopy we wish to point out an important aspect of the mechanism involved in the change of spin-state ordering. In our measurement the system $LaCo_{1-x}Zr_xO_3$ contains radioactive ^{57}Co nuclei with β -decay, by K-capture of electrons, to ^{57}Fe nuclei. As explained by Bhide et al. [5] it is safe to assume that low-spin Co will give, on electron capture, low-spin Fe and that high-spin Co will lead to high-spin Fe. In other words, Co^{3+} and Co^{III} on

electron capture gives Fe^{3+} and Fe^{III} ions respectively. In this way the ratio $\text{Fe}^{3+}:\text{Fe}^{\text{III}}$ deduced from our Mossbauer spectroscopic studies should lead us to the ratio $\text{Co}^{3+}:\text{Co}^{\text{III}}$ in the $\text{LaCo}_{1-x}\text{Zr}_x\text{O}_3$ system. The schematic energy-level diagram of various spin states of cobalt and the consequent iron states is shown in Fig. 4.2.

The Mössbauer spectra of the compound $\text{LaCo}_{1-x}\text{Zr}_x\text{O}_3$ ($x = 0.1, 0.3$ and 0.5) recorded at 80 K are shown in Fig. 4.3. It is observed that the Mössbauer spectrum of the compound with $x = 0.1$ and $x = 0.3$ at 80 K consist of two lines while that for $x = 0.5$ consists of three lines. The Mössbauer parameters for these spectral lines are given in Table 4.2. These Mössbauer data, when combined with the data of Table 1.4, allow us to make an assignment for various observed lines. Thus the lower energy lines observed in the Mössbauer spectra for $x = 0.1$ and 0.3 at 80 K are ascribed to the Co^{III} state and the higher energy lines in these spectra are assigned to the Co^{3+} state in the $\text{LaCo}_{1-x}\text{Zr}_x\text{O}_3$ system. It is pointed out that this result is consistent with the previous observations of the LaCoO_3 system [5-6]. It may be argued that the substitution of Zr^{4+} in our system can produce divalent Co ions (Co^{II} or Co^{2+}). However, the isomer shift (IS) values for Co^{III} and Co^{II} (i.e. for Fe^{III} and Fe^{II}) overlap (Table 1.4) and hence it is not possible to resolve the presence of Co^{III} state from Co^{II} state. On the other hand the IS value

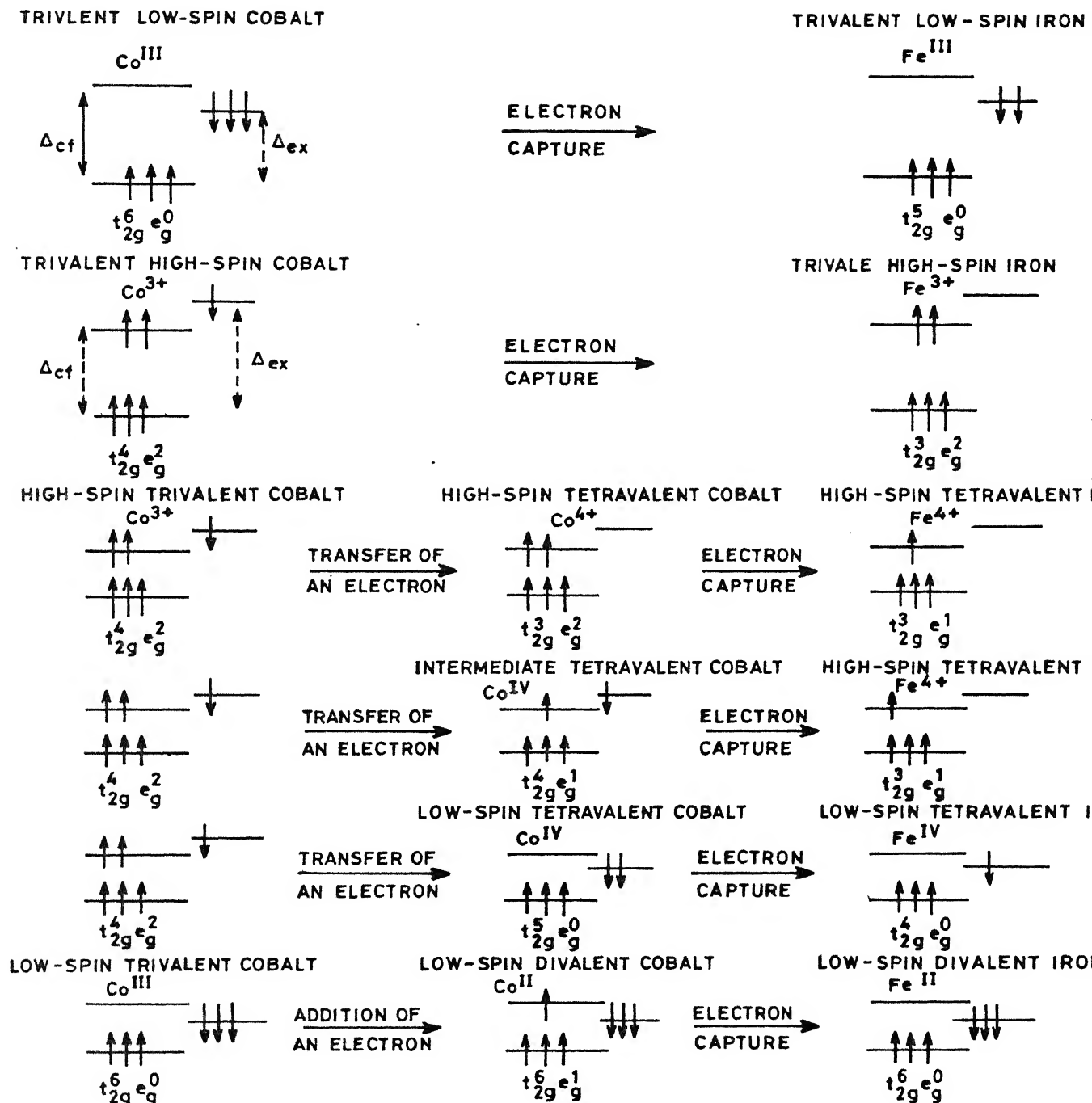


Fig.4.2 Spin states of cobalt and consequent iron.

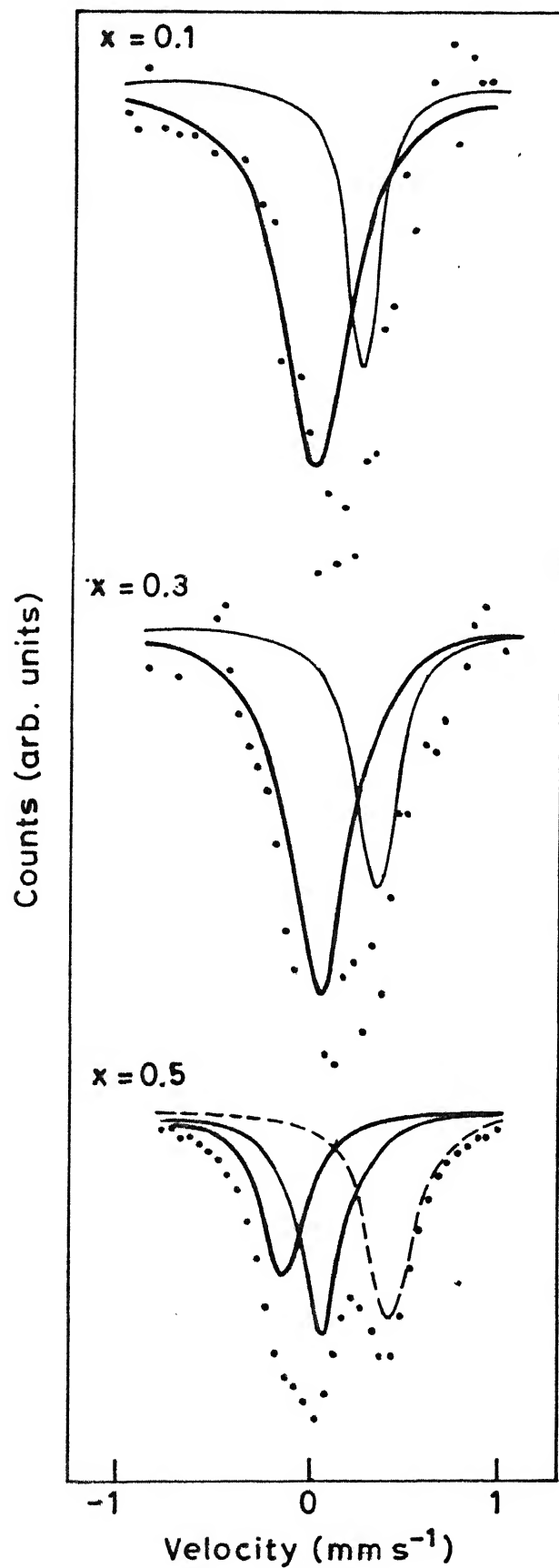
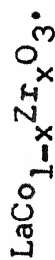


Fig. 4.3 Mössbauer spectra of $\text{LaCo}_{1-x}\text{Zr}_x\text{O}_3$ at 80 K.

Table 4.2 : Mössbauer parameters (measured at 80 K) for



Composition x	Ist resonance		IIInd resonance		IIIRD resonance	
	IS mms^{-1}	$\Gamma(\text{FWHM})$ mms^{-1}	Assignment	IS mms^{-1}	$\Gamma(\text{FWHM})$ mms^{-1}	Assignment
0.1	0.03	0.44	$\text{Co}^{\text{II}}, \text{Co}^{\text{III}}$	0.29	0.22	Co^{3+}
0.3	0.04	0.39	$\text{Co}^{\text{II}}, \text{Co}^{\text{III}}$	0.35	0.28	Co^{3+}
0.5	-0.17	0.28	Co^{II}	0.03	0.30	$\text{Co}^{\text{II}}, \text{Co}^{\text{III}}$
				0.42	0.30	Co^{3+}

IS = Isomer shift measured with respect to $\alpha\text{-Fe}$: Typical error $\pm 0.01 \text{ mm s}^{-1}$.

$\Gamma(\text{FWHM})$ = Line width : Typical error $\pm 0.01 \text{ mm s}^{-1}$.

IS at room temperature

IS is corrected for second order Doppler shift.

corresponding to Co^{2+} is too high (and is separable from Co^{3+}) but no line with such high IS is observed in our spectra at 80 K. We, therefore, conclude that the substitution of Zr^{4+} does not yield a Co^{2+} state in our system for $x = 0.1$ and 0.3 , while the Co^{II} state may be produced. The Mössbauer spectrum for $x = 0.5$ show three lines out of which the two lines on the lower energy side lie close together to give the composite line observed by us. We propose that this composite line is due to the two closely lying lines due to Co^{III} and Co^{II} present in the $\text{LaCo}_{0.5}\text{Zr}_{0.5}\text{O}_3$ system. Based on this discussion we propose that at 80 K, cobalt ions in the system $\text{LaCo}_{1-x}\text{Zr}_x\text{O}_3$ ($x=0.1, 0.3$ and 0.5) exist mainly in the three spin states low spin Co^{II} ($t_{2g}^6 e_g^1$), Co^{III} ($t_{2g}^6 e_g^0$) and high spin Co^{3+} ($t_{2g}^4 e_g^2$).

The Mössbauer spectra of the three samples ($x = 0.1, 0.3$ and 0.5) recorded at 293 K are shown in Fig. 4.4 and they can all be decomposed into two lines of equal intensities. At first sight, it appears tempting to describe these two lines as the two partners of a quadrupole split spectrum. However a closer examination rules out such a possibility because first, the electric quadrupole interaction in the ABO_3 structure is expected to be negligibly small [5-10]. Secondly the centroid of these two lines (i.e. the isomer shift of a possible quadrupole-split doublet) does not correspond to any known valence state

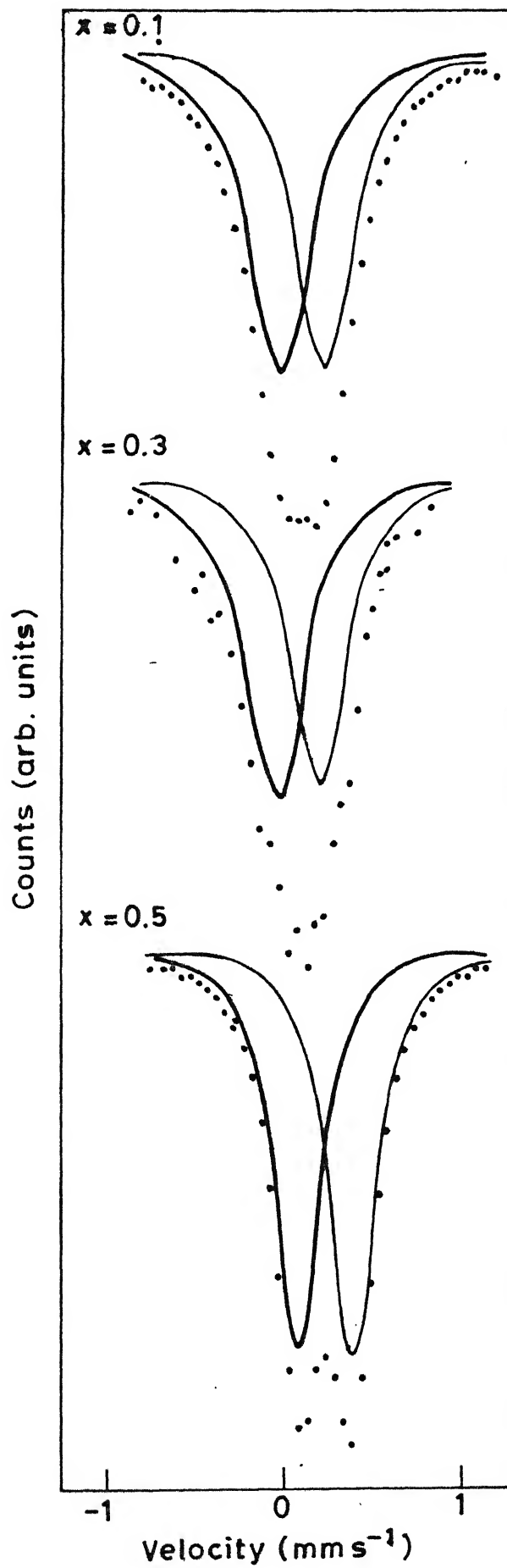


Fig. 4.4 Mössbauer spectra of $\text{LaCo}_{1-x}\text{Zr}_x\text{O}_3$ at 293 K .

of iron. On other hand, the velocity of each of these single lines (Fig. 4.4) leads us to IS-values corresponding to $(\text{Co}^{\text{III}} + \text{Co}^{\text{II}})$ and Co^{3+} . The former assignment (i.e. mixture of Co^{III} and Co^{II} states) is justified because of the larger line width and the overlapping IS values of Fe^{III} and Fe^{II} states (Table 4.3). We, therefore, suggest that at 293 K, the system $\text{LaCo}_{1-x}\text{Zr}_x\text{O}_3$ consists of the three spin states : Co^{III} , Co^{II} and Co^{3+} . Based on this assumption, as well as on the observed intensity ratio 1:1 of the two lines (Fig. 4.4), we further propose that the ratio $(\text{Co}^{\text{III}} + \text{Co}^{\text{II}}) : \text{Co}^{3+}$ in our system is close to 1 at 293 K.

We shall now examine the Mössbauer spectra of the $\text{LaCo}_{1-x}\text{Zr}_x\text{O}_3$ system recorded at higher temperatures ($700 > T > 500$ K) to identify the spin states present and to determine the ratio of their population. These results will be analyzed along with the results on magnetic susceptibility to draw definite conclusions.

The Mössbauer spectra for the $\text{LaCo}_{1-x}\text{Zr}_x\text{O}_3$ ($x = 0.1, 0.3, \text{ and } 0.5$) system recorded at 500 K are presented in Fig. 4.5. As discussed in the case of $T = 293$ K we have decomposed each of these spectra into two lines, one being ascribed to $(\text{Co}^{\text{III}} + \text{Co}^{\text{II}})$ and the other (having higher energy) to Co^{3+} state. This assignment is supported by the IS values (Table 4.4). It is observed (Fig. 4.5 and Table 4.4) that the area under the line corresponding to

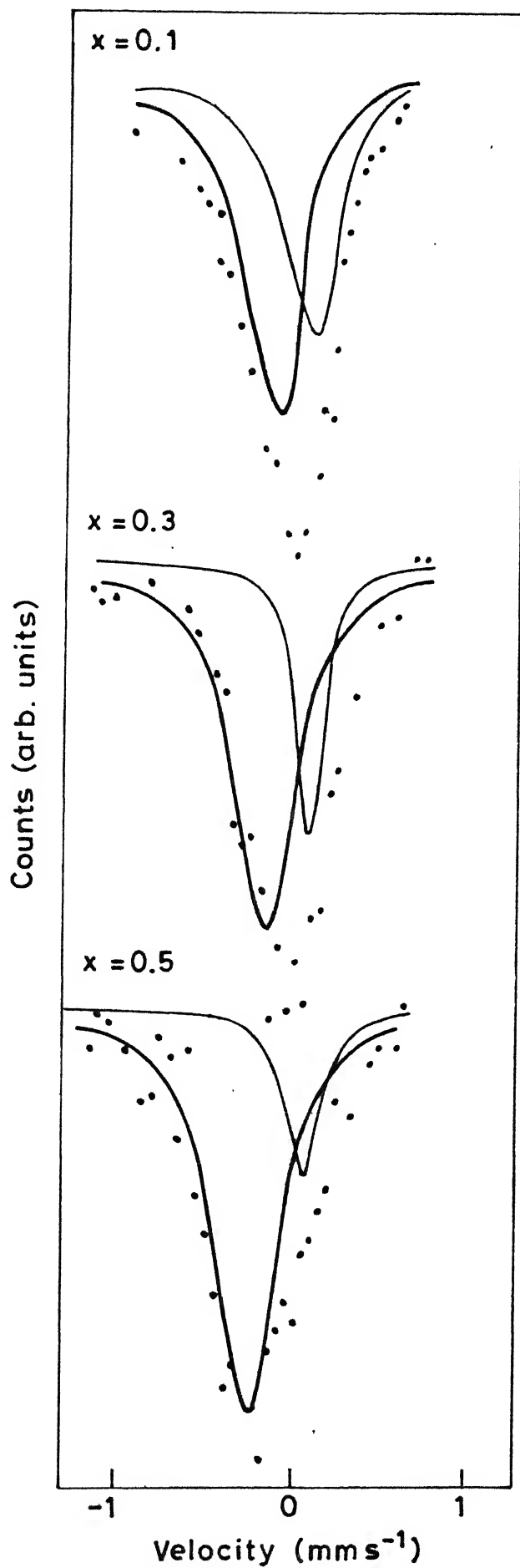
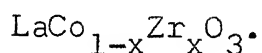


Fig. 4.5 Mössbauer spectra of $\text{LaCo}_{1-x}\text{Zr}_x\text{O}_3$ at 500 K.

Table 4.4 : Mössbauer parameters (measured at 500 K) for



Composition x	Ist resonance			IInd resonance		
	IS mms ⁻¹	$\Gamma(\text{FWHM})$ mms ⁻¹	Assignment	IS mms ⁻¹	$\Gamma(\text{FWHM})$ mms ⁻¹	Assignment
0.1	-0.08	0.40	Co ^{II} , Co ^{III}	+0.11	0.40	Co ³⁺
0.3	-0.12	0.22	Co ^{II} , Co ^{III}	0.15	0.33	Co ³⁺
0.5	-0.09	0.26	Co ^{II} , Co ^{III}	0.23	0.43	Co ³⁺

IS = Isomer shift measured with respect to $\alpha\text{-Fe}$:
 Typical error $\pm 0.01 \text{ mm s}^{-1}$. IS at room temperature

$\Gamma(\text{FWHM})$ = Line width : Typical error $\pm 0.01 \text{ mm s}^{-1}$.

IS is corrected for second order Doppler shift

Co^{3+} has now become larger than that at 293 K. In fact the ratio $\text{Co}^{3+} : (\text{Co}^{\text{III}} + \text{Co}^{\text{II}})$ has increased from 1.0 in going from 293 K to 500 K and has become equal to 1.3, 2.9 and 4.0 for $x = 0.1$, 0.3 and 0.5 respectively.

In Fig. 4.6 we have shown the Mössbauer spectra for the $\text{LaCo}_{1-x}\text{Zr}_x\text{O}_3$ ($x = 0.1, 0.3$ and 0.5) system recorded at 700 K. The spectrum for $x = 0.1$ can be decomposed into two lines which are assigned to Co^{3+} and $(\text{Co}^{\text{III}} + \text{Co}^{\text{II}})$ states (Table 4.5). The spectra for $x = 0.3$ and 0.5 can, however, be decomposed into three lines which are assigned to Co^{3+} , $(\text{Co}^{\text{III}} + \text{Co}^{\text{II}})$ and Co^{2+} . In the case of the spectra for $x = 0.3$ and 0.5 , the third line is identified as due to Co^{2+} on the basis of (i) observed IS value (Table 4.5) which conforms to the value characteristic of Co^{2+} (Table 1.4) (ii) results of magnetic measurements discussed earlier. The possible mechanisms responsible for the production of these states are discussed later.

Using our Mössbauer data we have obtained the ratio y of the relative population of Co^{3+} (i.e. Fe^{3+}) with respect to other states of Co (i.e. Fe). This ratio was determined with the help of the areas under individual lines in the respective Mössbauer spectra observed for $x = 0.1, 0.3$ and 0.5 at 80, 293, 500 and 700 K. The temperature variation of this ratio y (relative population of Co^{3+}) is plotted in Fig. 4.7 and Table 4.6 for each value of x .

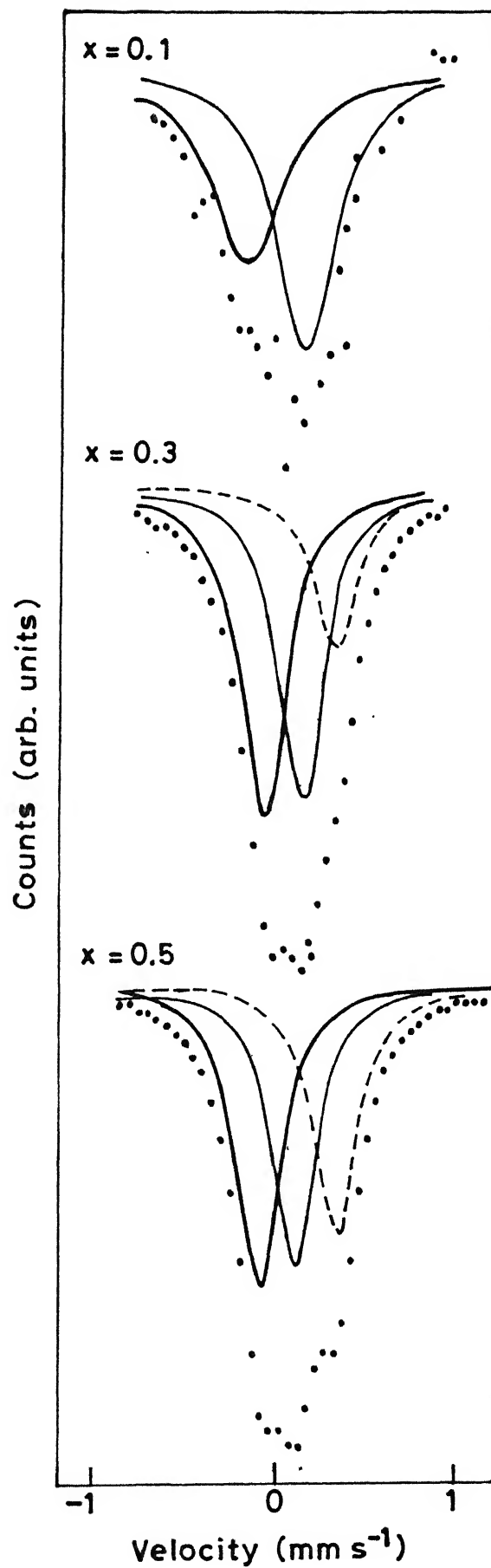


Fig. 4.6 Mössbauer spectra of $\text{LaCo}_{1-x}\text{Zr}_x\text{O}_3$ at 700K .

Table 4.5 : Mössbauer parameters (measured at 700 K) for



Composition x	1st resonance		2nd resonance		3rd resonance	
	IS mm s^{-1}	$\Gamma(\text{FWHM})$ mm s^{-1}	Assignment	IS mm s^{-1}	$\Gamma(\text{FWHM})$ mm s^{-1}	Assignment
0.01	-0.15	0.48	$\text{Co}^{\text{II}}, \text{Co}^{\text{III}}$	0.18	0.42	Co^{3+}
0.03	-0.05	0.28	$\text{Co}^{\text{II}}, \text{Co}^{\text{III}}$	0.15	0.26	Co^{3+}
0.05	-0.08	0.28	$\text{Co}^{\text{II}}, \text{Co}^{\text{III}}$	0.15	0.25	Co^{3+}
						Co^{2+}
						Co^{2+}

IS = Isomer shift measured with respect to $\alpha\text{-Fe}$: Typical error $\pm 0.01 \text{ mm s}^{-1}$.

$\Gamma(\text{FWHM})$ = Line width : Typical error $\pm 0.01 \text{ mm s}^{-1}$.

IS is corrected for second order Doppler shift.

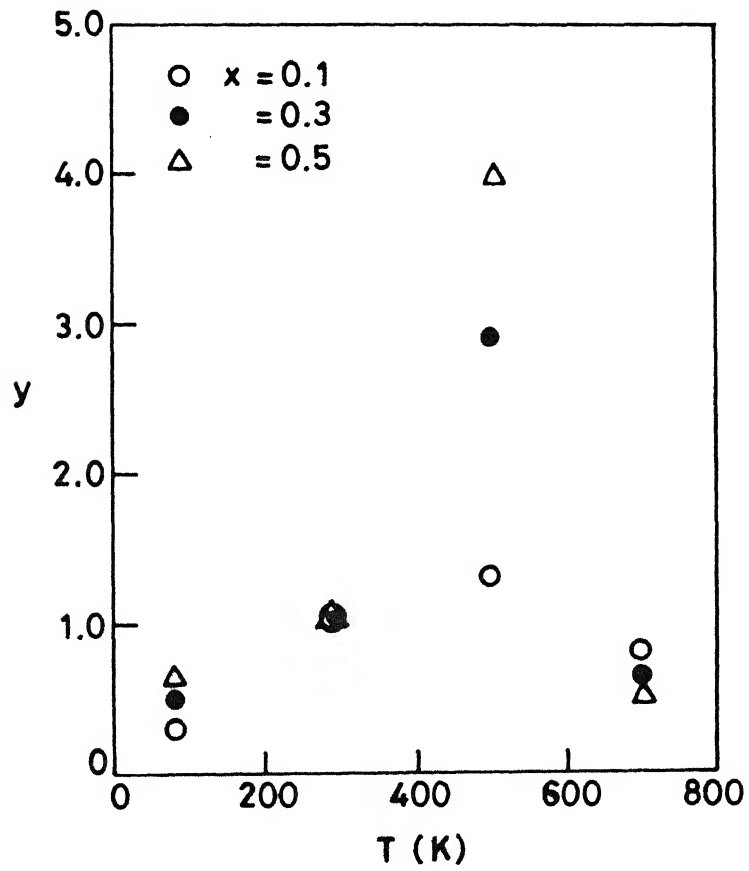


Fig. 4.7 Variation of y as a function of temperature.

Table 4.6 : The ratio y giving the relative population of Co^{3+} with respect to the other state of Co in $\text{LaCo}_{1-x}\text{Zr}_x\text{O}_3$.

Temperature K	$x = 0.1$	$x = 0.3$	$x = 0.5$
80	0.3	0.5	0.6
293	1.0	1.0	1.0
500	1.3	2.9	4.0
700	0.8	0.6	0.5

Bhide et al. [5-6] have also observed a temperature variation of the relative population (y) of Co^{3+} (with respect to other states of Co) in the LaCoO_3 system by Mössbauer spectroscopy and their curve shows that in the case of LaCoO_3 , y increases between 78 and 200 K and decreases beyond 200 K. The trend of the temperature variation of y observed by us for $\text{LaCo}_{1-x}\text{Zr}_x\text{O}_3$ (Fig. 4.7) is somewhat similar except that in the temperature range 293-500 K the rate of variation of y is different from LaCoO_3 and the temperature variation observed by us seems to depend on the value of x . If we go back to the variation of $\chi_g T$ versus T (Fig. 4.1b) observed by us we observe that the behaviour shown by the $x = 0.1$ system was markedly different from that shown by the $x = 0.3$ and 0.5 systems. Similar trend is shown by the behaviour of the temperature variation of y (Fig. 4.7). The general behaviour of the relative population of the Co^{3+} state (with respect to other states of cobalt) for each x -value and for different temperatures is similar. To understand this behaviour it will be necessary to develop a proper theoretical framework similar to that proposed by Goodenough [1,3-4] and others. We hope that our experimental results will encourage such a theoretical effort. It may be pointed out here that none of the Mössbauer spectra shows the presence of magnetic hyperfine splitting even at 80 K. This can be explained by proposing that Zr^{4+} substitution

restricts the generation of Co^{4+} ions which are responsible for ferromagnetic interaction observed in $\text{La}_{1-x}\text{Sr}_x\text{CoO}_3$ [9]. Similar behaviour has also been observed for the system $\text{LaCo}_{1-x}\text{Ti}_x\text{O}_3$ [17].

Before concluding this discussion we wish to propose a possible mechanism for explaining the decrease in γ between 500 and 700 K (Fig. 4.7). It is observed that between 500 and 700 K γ decreases by a smaller amount for $x = 0.1$ while it decreases by a larger amount for $x = 0.3$ and 0.5 . It has been suggested by Goodenough [1,3-5] that Co^{3+} can transfer an e_g electron to Co^{III} to form Co^{2+} and Co^{IV} ion pairs. We have found evidence in our Mössbauer spectra for the presence of Co^{2+} ions at 700 K for $x = 0.3$ and 0.5 . It, therefore, appears that the above conversion of Co^{3+} to other states, as suggested by Goodenough [3-5] is working efficiently for $x = 0.3$ and 0.5 between 500 and 700 K. However the reason what inhibits such a conversion for $x = 0.1$ is not clear to us. We feel that answer to this question as well as to other questions related to the behaviour observed by us has to await a proper theoretical analysis.

4.4 SUMMARY AND CONCLUSIONS

The system $\text{LaCo}_{1-x}\text{Zr}_x\text{O}_3$ ($x = 0.1, 0.3$ and 0.5) has been studied with the help of X-ray diffraction, magnetic

susceptibility measurements and Mössbauer spectroscopy. Magnetic susceptibility was measured in the temperature range 300–800 K and Mössbauer spectra were recorded at 80, 293, 500 and 700 K. These results were examined with an aim to understand the relative population of different spin states of cobalt in the $\text{LaCo}_{1-x}\text{Zr}_x\text{O}_3$ system for $x = 0.1, 0.3$ and 0.5 . It was observed that the behaviour of the system with $x = 0.1$ is quite different from that with $x = 0.3$ or $x = 0.5$. The Mössbauer data have enabled us to understand the presence of various spin states for different x at each temperature. The relative population of Co^{3+} with respect to other spin states of cobalt have been estimated for $x = 0.1, 0.3$ and 0.5 at 80, 293, 500 and 700 K. These results show a general agreement with those obtained by magnetic measurements. Some suggestions are made about the mechanism responsible for the observed changes in these relative populations. It is suggested that further theoretical work is necessary to improve our understanding about these changes in the spin states of cobalt.

REFERENCES

1. J.B. Goodenough, J. Appl. Phys. 37, 1415 (1966).
2. N. Menyuk, K. Dwight and P.M. Raccach, J. Phys. Chem. Solids 28, 549 (1967).
3. P.M. Raccach and J.B. Goodenough, Phys. Rev. 155, 932 (1967).
4. J.B. Goodenough, Czech. J. Phys. B17, 304 (1967).
5. V.G. Bhide, D.S. Rajoria, G. Rama Rao and C.N.R. Rao, Phys. Rev. B6, 1021 (1972).
6. V.G. Bhide, D.S. Rajoria, Y.S. Reddy, G. Rama Rao, G.V. Subba Rao and C.N.R. Rao, Phys. Rev. Letts. 28, 1133 (1972).
7. N. Menyuk, P.M. Raccach and K. Dwight, Phys. Rev. 166, 510 (1969).
8. V.G. Bhide, D.S. Rajoria, Y.S. Reddy, G. Rama Rao and C.N.R. Rao, Phys. Rev. B8, 5028 (1973).
9. V.G. Bhide, D.S. Rajoria, C.N.R. Rao, G. Rama Rao and V.G. Jadhao, Phys. Rev. B12, 2832 (1975).
10. V.G. Jadhao, R.M. Singru, G. Rama Rao, D. Bahadur and C.N.R. Rao, J. Chem. Soc. Faraday Trans. II 71, 1885 (1975).
11. V.G. Jadhao, R.M. Singru, G.N. Rao, D. Bahadur and C.N.R. Rao, J. Phys. Chem. Solids, 37, 113 (1976).
12. C.N.R. Rao, Om Prakash, D. Bahadur, P. Ganguly and S. Nagabhushana, J. Solid State Chem. 22, 353 (1977).

13. D. Bahadur, S. Kollali, C.N.R. Rao, M.J. Patni and C.M. Srivastava, J. Phys. Chem. Solids 40, 981 (1979).
14. D.P. Karim and A.T. Aldred, Phys. Rev. B20, 2255 (1979).
15. S.B. Patil, D.K. Chakrabarty, M.V. Babu and S.N. Shringi, Phys. Status Sol. (a) 65, 65 (1981).
16. D. Bahadur and Om Prakash, J. Solid State Chem. 46, 197 (1983).
17. V. Kumar, R.M. Singru, Om Prakash and D. Bahadur, Phys. Status Sol. (b) 128, 223 (1985).
18. P. Ganguly and N.Y. Vasanthacharya, J. Solid State Chem. 61, 164 (1986).
19. D. Bahadur (Private Communication).

CHAPTER 5

MÖSSBAUER SPECTROSCOPIC STUDIES OF THE SUPER SENDUST ALLOY

5.1 INTRODUCTION

In this chapter we shall report our Mössbauer spectroscopic and X-ray diffraction studies of the so-called 'Super Sendust' alloy of the Fe-Si-Al-Ni system. This alloy has the composition 2.96 wt % Ni, 5.0 wt % Si, 3.87 wt % Al and 88.17wt%Fe and it is a new high-permeability magnetic alloy having several possible technical applications of interesting nature. We shall provide a brief outline of the history of the development of 'Sendust' alloys before we present the results of our studies.

The search for high permeability materials started at the beginning of the present century. The idea of using powder cores to increase the inductance of the coils was reported by Heaviside [1] who used iron fillings embedded in wax without causing any appreciable dissipation of energy. This development promised newer applications in the telephone technology of that time. Cores having higher (30-60 μ_0) permeabilities were later manufactured after the introduction of high moulding pressures [2], and were produced commercially by Western Electric Company of U.S.A. In view of the important technological applications, research in this area was continued vigorously and

some important landmarks of progress in this area were the discovery of the specially suitable properties of carbonyl-iron powder in Germany [3,4] followed by the application of nickel-iron alloys in the U.S.A. In 1923, a material known as Permalloy containing 78.5% Ni and 21.5% Fe was developed by Elmen [5] and compressed powder cores of this alloy were found to be electrically and magnetically superior to the cores made from electrolytic iron because of its high permeability and low magnetic hysteresis losses.

A systematic search for a high-permeability material was started in 1929 at the Metal Materials Research Institute of Tohoku Imperial University, Japan under the supervision of H. Masumoto. These workers found that a ternary alloy of iron, silicon and aluminium was most promising and especially those alloys having the range of about 6-11% Si and 4-6% Al showed noticeably higher permeabilities and reduced hysteresis loss [6]. Since these alloys were developed in Sendai City in Japan and because they could be pulverised easily, they were named 'Sendust'.

Electrolytic iron has an initial permeability of about $140 \mu_0$. When about 8% Si is added to it, the permeability rises to $1200 \mu_0$. It is found that Sendust of composition 9.5% Si - 5.5% Al - bal. Fe has an initial permeability $\mu_i = 35,000 \mu_0$ and maximum permeability $\mu_m = 120,000 \mu_0$, hysteresis loss $W_h = 28 \text{ ergs/cm}^2/\text{cycle}$,

electrical resistivity of $81.2 \mu\Omega\text{-cm}$, thus proving itself to be superior to Permalloy ($\mu_i = 10,000 \mu_o$, $\mu_m = 120,000 \mu_o$, $\rho = 16 \mu\Omega\text{-cm}$ and $W_h = 73 \text{ ergs/cm}^3/\text{cycle}$). The coercivity of Sendust is also lower than that of Permalloy (1.75 A/m as against 4 A/m). Further, the manufacturing cost of Sendust is also much lower compared to Permalloy.

Yamamoto and Utsushikawa [7] developed an alloy with a composition of 3.15% Ni - 5.33% Si - 4.22% Al - bal. Fe which, after annealing at 1250°C for 1 hr in the presence of magnetic field of 20 Oe showed the following magnetic properties : $\mu_i = 56,800 \mu_o$, $\mu_m = 165,000 \mu_o$, $H_c = 2.39 \text{ A/m}$ and $B_r = 0.95 \text{ T}$. This alloy was, therefore, named as 'Super Sendust' by these workers [7]. Later the name 'Super Sendust' was extended [8] to the alloys having the following three composition ranges : (i) the composition range yielding high magnetic permeability after heat treatment, (ii) the range in which the permeability is high after magnetic field cooling, and (iii) the range for which the magnetostriction $\lambda_s = 0$, can be hot-rolled to thicknesses of 0.5 mm, and can be cold-rolled to thicknesses of 0.2 mm.

In our Institute 'Super Sendust' alloy having a composition 2.96 wt % Ni, 5.0 wt % Si, 3.87 wt % Al and 88.17 wt % Fe was synthesized using thermite process and was investigated for its structural, mechanical, electrical and magnetic properties [8]. We found that very little

work on the Super Sendust alloy, using Mössbauer spectroscopy, has been reported in the literature. Thus, for example, Schneeweiss et al. [9] have studied the influence of substitution of Al by Si on the atomic order, saturation magnetic polarization and electrical resistivity in the $\text{Fe}_3\text{Al}_{1-x}\text{Si}_x$, $0 \leq x \leq 1$ alloys. These workers have examined the changes in the Mössbauer parameters of the $\text{Fe}_3\text{Al}_{1-x}\text{Si}_x$ system and have related them to an important phenomenon in the atomic structure of the alloys, viz. separation of Fe_3Al and Fe_3Si surroundings.

We therefore, thought it interesting to study Super Sendust samples having the composition 2.96 wt % Ni, 5.0 wt % Si, 3.87 wt % Al and 88.17 wt % Fe by Mössbauer spectroscopy at different temperatures. Three samples of above compositions were annealed according to a different schedule of temperature/time period. Mössbauer spectra of these samples were recorded at 80 and 293 K and at 380, 486, 600, 700, 800, 900, 913, 918 and 926 K. Resulting spectra were analyzed to obtain Mössbauer parameters, hyperfine field distributions, $P(H)$ and the average value of \bar{H}_{int} at the ^{57}Fe nucleus etc. These results were further analyzed in terms of the four sextets present in the spectra at 80, 293, 380, 486, 600, 700 and 800 K. The possible assignment for each of the 4 sextets observed at 293 K is suggested. Similarly the temperature dependence of the spectra and their Mössbauer parameters

is discussed. The distribution, $P(H)$ of the hyperfine magnetic field is also discussed.

5.2 EXPERIMENTAL METHOD

5.2.1 Sample Preparation

In this section we shall briefly outline the procedure adopted by Uniyal [8] (who provided us with these samples) in our Institute for synthesizing Super Sendust alloy by aluminothermic process. More details of the thermite process describing the thermite charge, ignitors and thermite crucibles used are given elsewhere [8]. The raw materials used in the preparation of the present alloys were obtained as follows. Fe_3O_4 was obtained in the form of flakes 'Al' powder - 325 mesh supplied by SISCO Research Laboratory, Bombay while Ni (110 mesh) was also obtained from the same supplier. Ferro-silicon was obtained in the form of solid mass which was ground to fine powder so that it could be mixed properly with the charge. Proper amount of CaO was obtained from Glaxo Laboratories, Bombay in the form of lumps and it was added as fluxing agent to control the fluidity and to lower the temperature. This addition to the charge was made in the ratio $\text{CaO}:2\text{Al}_2\text{O}_3$ as 1:2. The ignitor consisted of 99.5% pure KMnO_4 crystals supplied by British Drug House (India), Bombay, and glycerine obtained from

I.D.P.L. Hyderabad. Appropriate weights of these components were properly mixed in a pestle and mortar to ensure a higher reaction rate and better yield. A specially designed reactor was used to carry out the thermite reaction. The solid alloy ingots obtained after the reaction were hammered to small pieces of about mm in size in a steel mortar. Permanent magnet was used to sort out these pieces and to remove any slag material that could have been trapped inside the solid alloy. These pieces were again subjected to hammering to reduce them to still smaller pieces and were again separated out by the magnet. This process yielded somewhat coarse powder which was put in a planetary ball mill (tungsten-carbide lined drum) with tungsten carbide balls in a 2:1 proportion by weight. Acetone was used as a non-aqueous medium to avoid corrosion of balls, rotating drum and also for preventing oxidation of raw materials. After wet-milling for 24 hours, the slurry of the fine powder was transferred into a large beaker and put in an oven at around 100°C for drying. The whole process yielded fine powder which was sintered at 800°C , 900°C and 1000°C for 6 hr, 8 hr and 8 hr respectively, and these formed the material for the three samples labeled as SD1 ($1000^{\circ}\text{C}/6\text{ hr}$), SD2 ($900^{\circ}\text{C}/8\text{ hr}$) and SD3 ($800^{\circ}\text{C}/8\text{ hr}$). The weight percent composition of each element present in the synthesized alloy was determined by a chemical analysis using conventional wet method and

it showed the following result : Fe (wt %) 88.19, Ni (wt %) 2.958, Si (wt %) 4.987 and Al (wt %) 3.865.

5.2.2 Mössbauer Spectroscopic Studies

Mössbauer absorbers were prepared from these powdered material of Super Sendust following the procedure described in Chapter 2. Transmission Mössbauer spectra of different sample absorbers were recorded with the help of Mössbauer spectrometer (already described in Chapter 2) operated in constant acceleration mode. The spectra were recorded at room temperature (293 K), liquid nitrogen temperature (80 K) and higher (380 - 921 K) temperatures. A special oven (already described in Chapter 2) was used to record the spectra at higher (> 293 K) temperatures. The Mössbauer spectrometer was calibrated using α -Fe foil and the isomer shift (IS) was measured and reported with respect to α -Fe. Other details of the Mössbauer spectrometer, measurements and data analysis have been already described in Chapter 2.

5.2.3 Measurement of X-ray Diffraction Spectra

The results of Mössbauer spectroscopy were supplemented by recording X-ray powder diffraction patterns of the samples with the help of a Rich and Seifert Iso-Debyeflex 2002 diffractometer using $\text{CrK}\alpha$ target.

5.3 RESULTS AND DISCUSSION

The Mössbauer spectra of samples SD1, SD2 and SD3 recorded at 80 and 293 K are shown in Figs. 5.1 and 5.2 respectively. It is observed that the Mössbauer spectra of all the three samples recorded at 80 and 293 K are almost similar. In order to study the high temperature effects as well as to determine the magnetic ordering temperature (T_c) of the Super Sendust sample, the Mössbauer spectra of sample SD1 were recorded at 380, 486, 600, 700, 800, 900, 913, 918 and 921 K and they are shown in Fig. 5.3 and 5.4. Above 900 K the Mössbauer spectra of the SD1 samples were measured at small intervals of temperature with an aim of closely examining the changes and precisely determining the magnetic ordering temperature. The measured Mössbauer spectra were analyzed to determine Mössbauer parameters, hyperfine field distribution, $P(H)$, and the average value of H_{int} at the ^{57}Fe nucleus.

The Mössbauer spectra of the three samples SD1, SD2 and SD3 recorded at 293 K consist of four sextets which are attributed to four different ^{57}Fe sites present in Super Sendust and they seem to arise out of the presence of Si, Ni and Al in α -Fe bcc lattice. The typical X-ray diffraction spectra of sample SD1 are shown in Fig. 5.5. It has been reported [10] that Sendust has two crystalline structures, the so-called ordered and

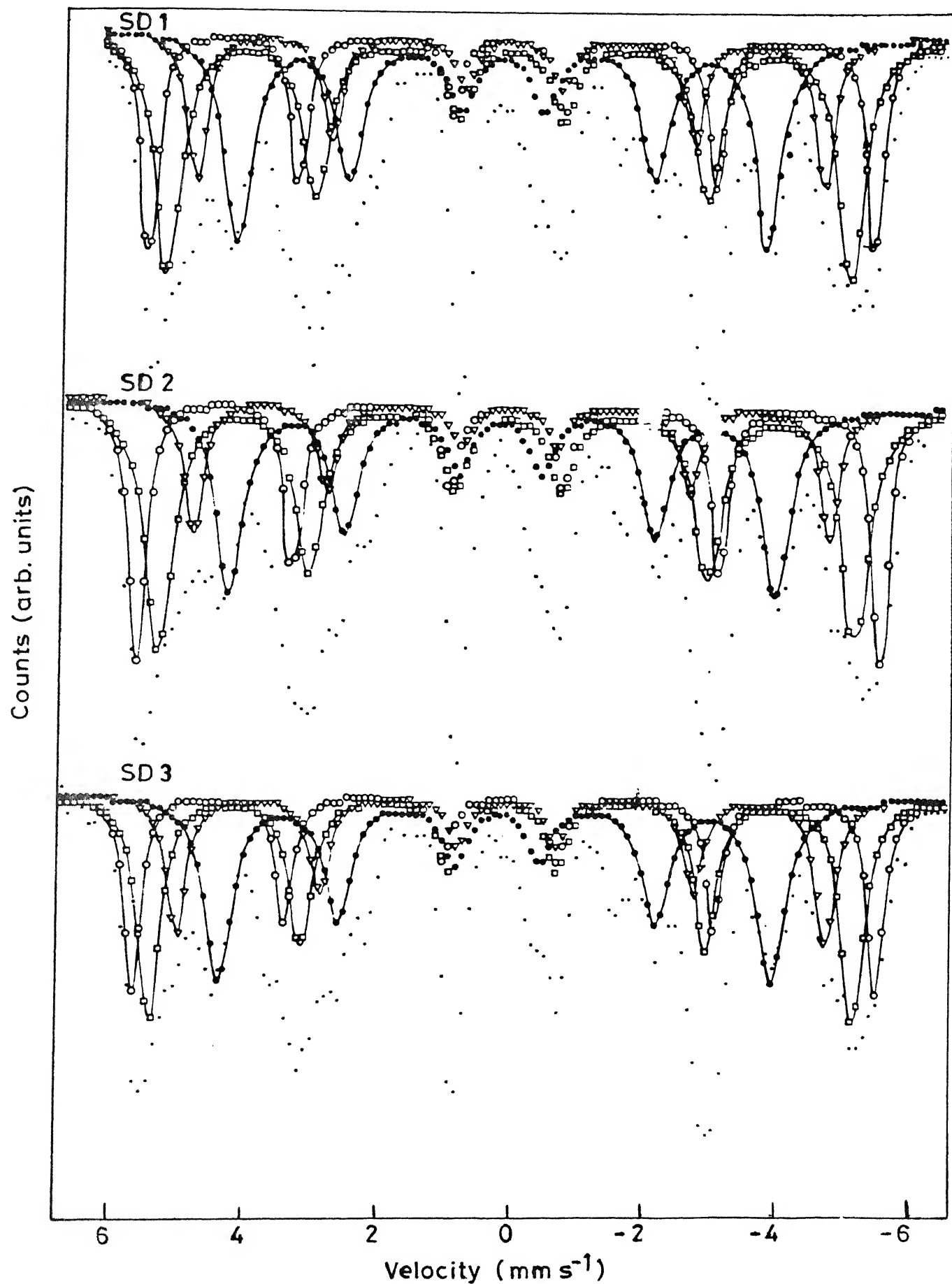


Fig. 5.1 Mössbauer spectra of SD1, SD2 and SD3 at 80K.

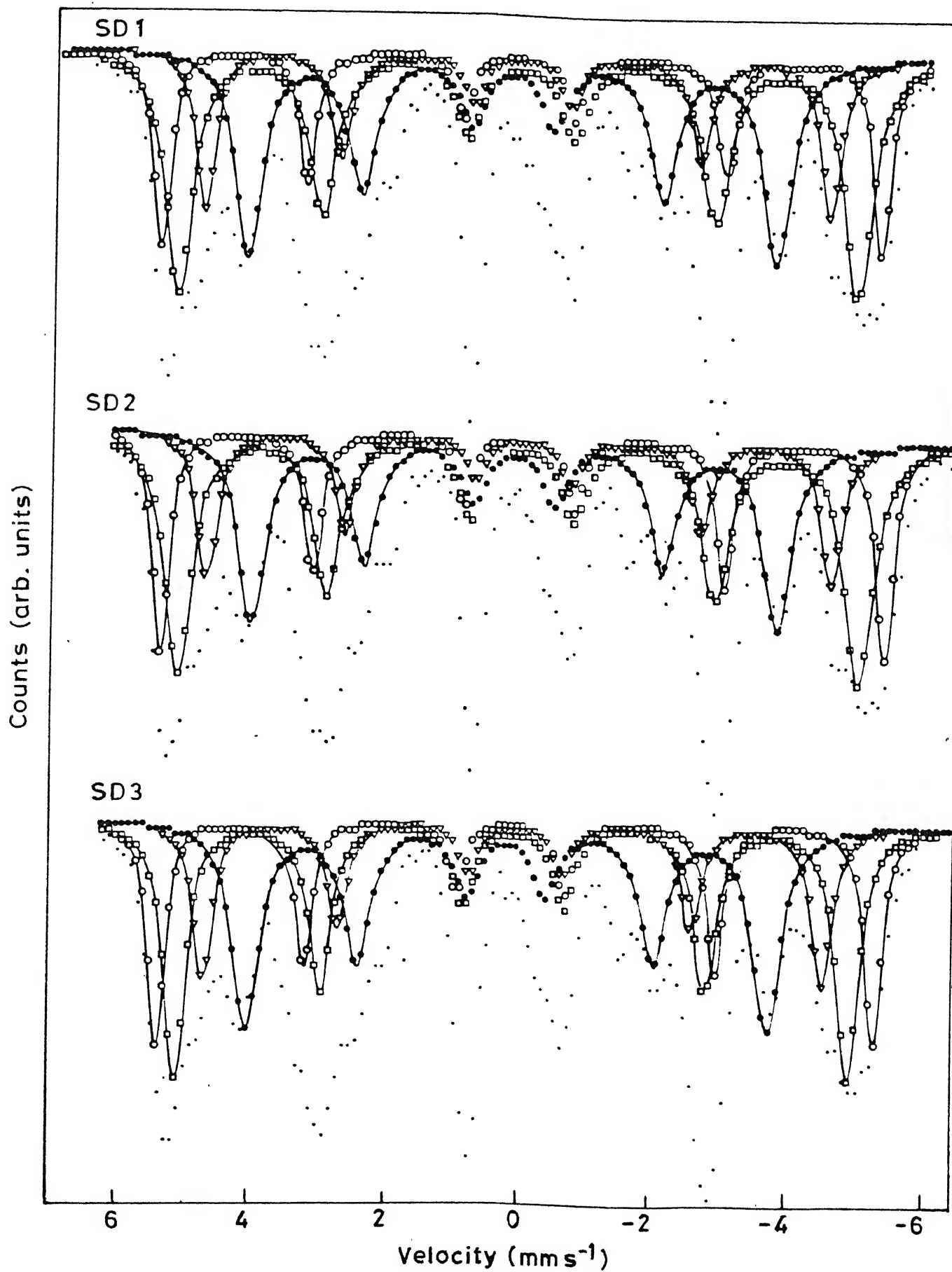


Fig. 5.2 Mössbauer spectra of SD1, SD2 and SD3 at 293K.

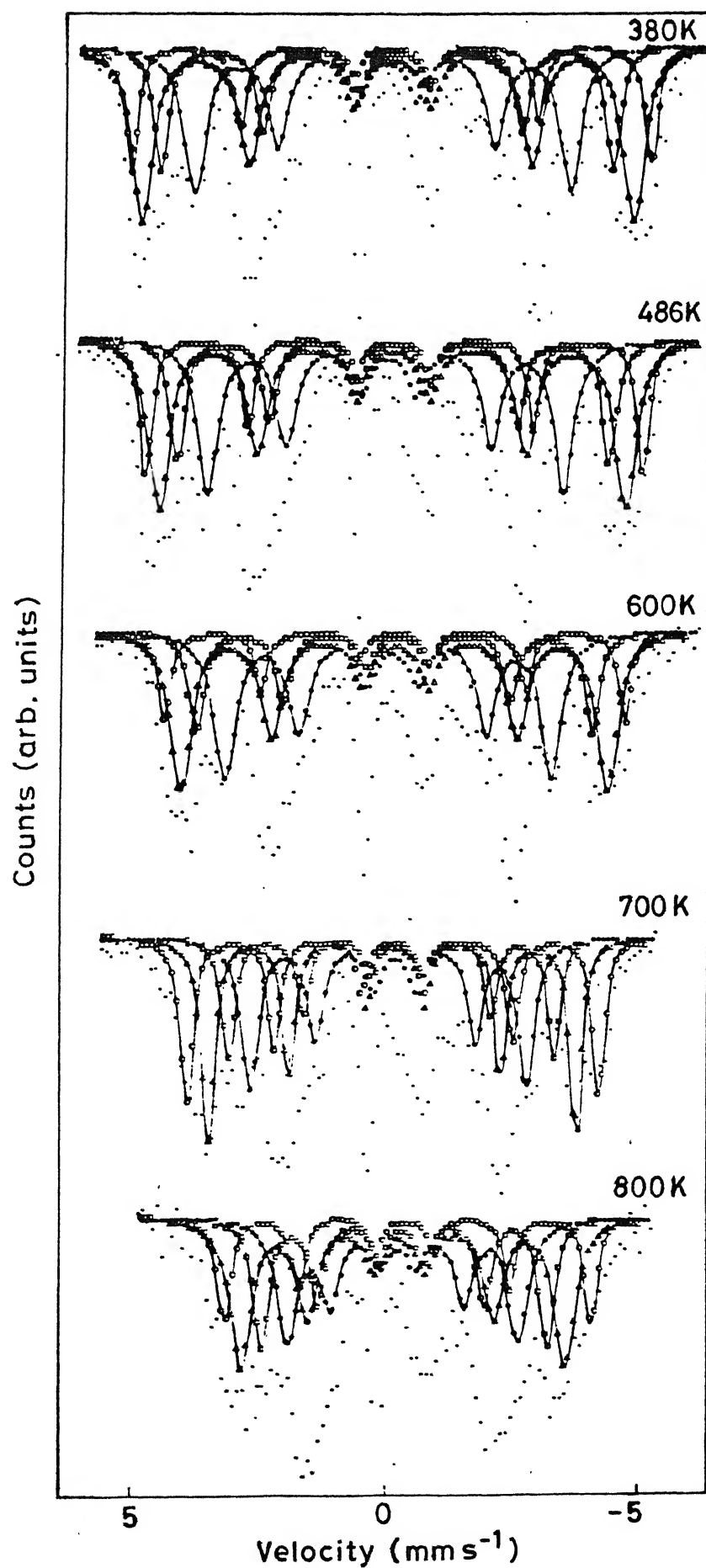


Fig.5.3 Mössbauer spectra of SD 1 in the temperature range 380 - 800K.

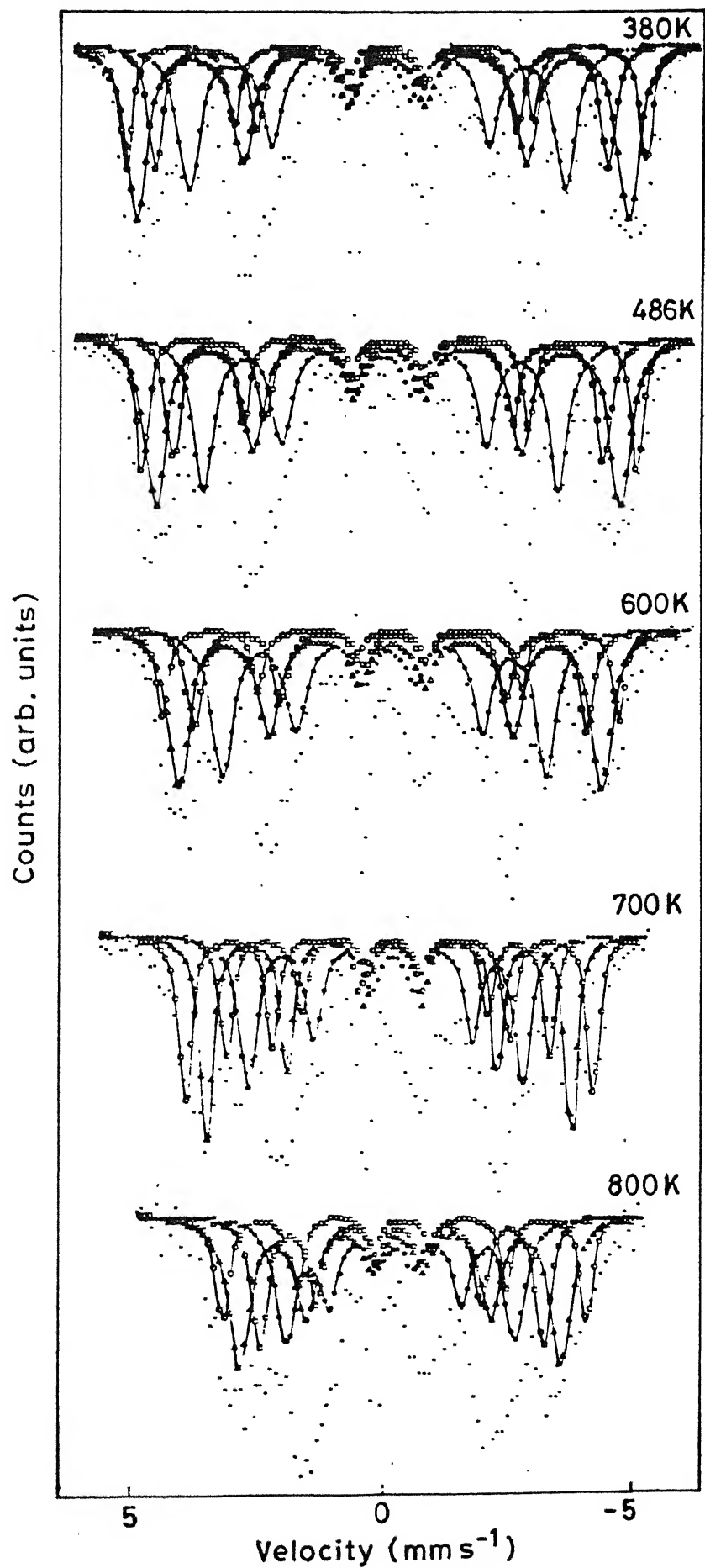


Fig.5.3 Mössbauer spectra of SD1 in the temperature range 380-800K

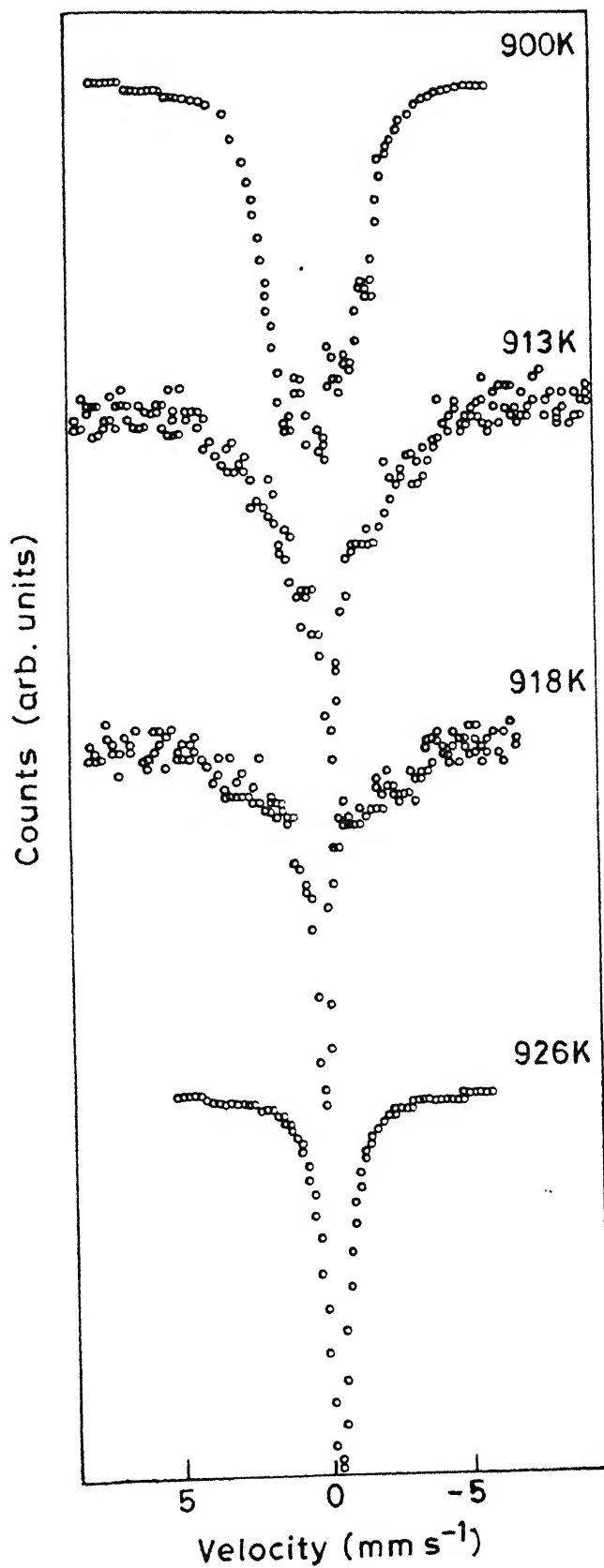


Fig. 5.4 Mössbauer spectra of SD1 in the temperature range 900 - 926 K.

disordered states. In the disordered state its crystalline structure is bcc and Si, Al and Ni occupy the sites randomly. However, in the ordered state Si and Al occupy the body-centered D sites (Fig. 5.6) giving rise to a superlattice structure. This superlattice structure has eight bcc unit cells as its unit cell has DO_3 type superlattice structure $[\text{Fe}_3(\text{Si},\text{Al})]$. Our X-ray diffraction studies have confirmed this superlattice structure. The degree of superlattice formation (the long-range order) is evaluated with the help of the intensity ratio of the superlattice diffraction line to the fundamental diffraction line. The Mössbauer spectra of the sample SD1 recorded at the temperatures ranging from 80 to 800 K indicated some kind of ordering. The analysis of these Mössbauer spectra suggests that Super Sendust is a partially ordered alloy having α -Fe rich region (i.e. clustering of iron). The Mössbauer parameters of the four sextets observed in the spectrum of the SD1 sample at 293 K are presented in Table 5.1 and are also summarised below for convenience of the discussion that follows.

- (1) First (I) sextet : $IS = + 0.01 \pm 0.01 \text{ mm s}^{-1}$,
 $H_{\text{int}} = 331 \pm 4 \text{ kOe}$, $r = 0.28 \pm 0.01 \text{ mm s}^{-1}$. This sextet exhibits almost vanishing isomer shift with respect to α -Fe and hyperfine magnetic field H_{int} which is close to the value characteristic of α -Fe.

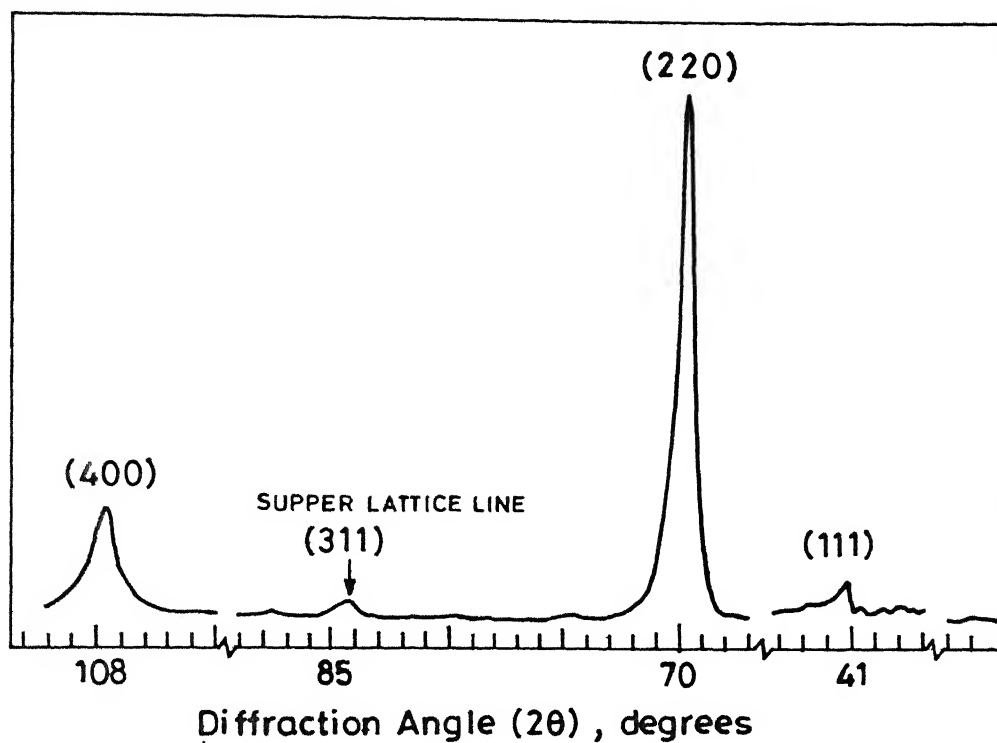
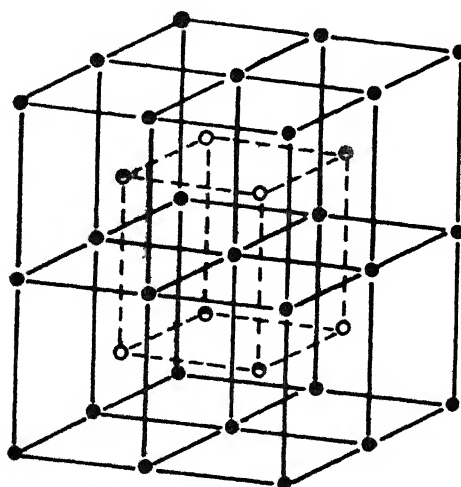


Fig. 5.5 X-ray diffraction spectrum of SD 1 at 293 K.



- Fe atoms - A sites
- Fe atoms - D sites
- Si atoms

Fig. 5.6 Unit cell of the ordered Fe_3Si or Fe_3Al structure.

It is, therefore, attributed to the ^{57}Fe nuclei present in the iron-rich region. Table 5.2 shows the sites and the hyperfine fields (H_{int}) observed for ordered alloys [11, 12] including the A'-site (pure iron) and those found in the present work for partially ordered iron-rich cluster alloy. The A'-site has 8 nearest neighbours (nn) Fe ion and 6 nearest next-neighbours (nnn) Fe ions.

- (2) Second (II) sextet : $IS = +0.06 \pm 0.01 \text{ mm s}^{-1}$,
 $H_{\text{int}} = 311 \pm 4 \text{ kOe}$, $\Gamma = 0.48 \pm 0.01 \text{ mm s}^{-1}$. Using the Mössbauer spectroscopy results of Stearns [11] and Perez-Alcazar and Galvao da Silva [12] we have attributed this sextet to ^{57}Fe nuclei having 8 nn Fe and 6 nnn Al or Ni or Si. The Al, Ni and Si have equal probability of occupying any D site. Ono et al. [13] have reported that in Fe_3Al structure, the ^{57}Fe nucleus at the D-site experiences $H_{\text{int}} = 300 \text{ kOe}$ if 8 nn Fe atoms are at the A-sites and the 6 nnn Al atoms are at the D-sites. The value of H_{int} observed by us for this sextet is close to $H_{\text{int}} = 300 \text{ kOe}$, the slight deviation observed being attributed to Ni atoms which have equal probability of occupying the D-site. According to the atomic weight percentages present in the SDI sample, these probabilities are 0.050, 0.0296 and 0.0387.

Table 5.1

Mossbauer parameters (measured at 293 K) for samples SD1, SD2, SD3.

Sam- ple	Site	IS(a)	H _{int} (b)	Γ(c)	Area ratio (e)	Assignment (d)
SD1	I	0.01	331.0	0.28	1.0	(8 nn + 6 nnn) Fe
	II	0.06	311.0	0.48	2.14	8 nn Fe + 6 nnn S or (Ni,Al)
	III	0.15	242.0	0.48	1.76	and [4Fe and 4 Si or (Ni,Al)] nn
	IV	0.07	286.0	0.35	0.98	+ 6 nnn Fe [6Fe and 2Si or (Ni,Al)] nn + 6 nnn Fe
SD2	I	0.02	330.8	0.28	1.0	Same as for SD1
	II	0.07	311.2	0.48	1.9	
	III	0.16	242.0	0.48	1.40	
	IV	0.07	286.5	0.35	0.78	
SD3	I	0.02	330.6	0.28	1.0	Same as for SD1
	II	0.08	310.7	0.48	1.97	
	III	0.14	240.6	0.48	1.59	
	IV	0.06	285.6	0.35	0.87	

(a) IS = Isomer shift, values in mm s⁻¹ with respect to α -Fe ^{IS of room temperature}
typical error is ± 0.01 mm s⁻¹.

(b) H_{int} = Internal magnetic field at ⁵⁷Fe nucleus : in units
of kOe. Typical error is ± 4 kOe.

(c) Γ (FWHM) = width of the spectral line, values in mm s⁻¹ :
Typical error is ± 0.01 mm s⁻¹.

(d) nn = nearest neighbour, nnn = next nearest neighbour.

(e) The area ratio values are given with respect to the
area (1.0) under sextet I.

IS is corrected for second order Doppler shift.

Table 5.2

Magnetic field (H_{int}) observed for different Fe sites in Fe-Al alloys found in literature and configurations obtained in the present Fe-Si(Ni,Al) alloy.

Site	Configuration	H_{int} (kOe)	Reference
A' or I	(8 nn+ 6 nnn)Fe	330	Present work
B	8 nn Fe + 6 nnn Al	300	[12,13]
C	(5Fe + 3Al) nn + 6 nnn Fe	261	[12,13]
D	(4Fe + 4 Al)nn + 6 nnn Fe	230	[12,13]
F	(7Fe + 1 Al)nn + 6 nnn Fe	306	[12,13]
G	(6Fe + 2Al)nn + 6 nnn Fe	282	[12,13]
II	8nn Fe + 6 nnn Si or (Ni,Al)	311	Present work
III	[4Fe+4Si or (Ni,Al)]nn+6nnnFe	242	Present work
IV	[6Fe+2Si(Ni,Al)]nn + 6 nnn Fe	286	Present work
B'	8 nn Fe + 4 or 2 or 0 Si (Ni,Al)nnn + 2 or 4,6nnn Fe		Possible in present work
C'	[5Fe+3Si(Ni,Al)]nn+6 nnn Fe		Possible in present work
F'	[7Fe+Si(Ni,Al)]nn + 6 nnn Fe		Possible in present work

for Si, Ni and Al respectively.

Neutron diffraction measurements have shown that different magnetic moments exist at the D and A sites in both Fe_3Al and Fe_3Si [14-15] with values of 2.4 and 1.2 μ_B per site respectively for the D and A sites in Fe_3Si and 1.13 and 1.5 μ_B per site respectively in Fe_3Al . Earlier Mössbauer spectroscopic measurements [16] on Fe_3Si and Fe_3Al have indicated that H_{int} at the A sites in Fe_3Al is larger than that at the A sites in Fe_3Si . Ni atom, which already has a magnetic moment, is expected to yield higher H_{int} when it is substituted for Si or Al. As a net result, when Ni, Si and Al are present at the D-site in superconducting dust, the sextets II and III are expected to show more broadening. This explains the value $\Gamma = 0.48 \text{ mm s}^{-1}$ observed by us.

(3) Third (III) sextet : $IS = +0.15 \pm 0.01 \text{ mm s}^{-1}$, $H_{\text{int}} = 242 \pm 4 \text{ kOe}$, $\Gamma = 0.48 \pm 0.01 \text{ mm s}^{-1}$. Using the previously reported results [11,12], this sextet is attributed to the ^{57}Fe nuclei at the A-sites having (4Fe + 4Si or Ni or Al) at the nn (D-) sites and 6 nnn Fe at the A-sites. It has been reported by Ono et al. [13] that in Fe_3Al alloy $H_{\text{int}} = 230 \text{ kOe}$ for the nn configuration. Our observed value $H_{\text{int}} = 242 \pm 4 \text{ kOe}$ is close to this value, the difference being explained in the same manner as in the case of II sextet (discussed above).

(4) Fourth (IV) sextet : $IS = +0.07 \pm 0.01 \text{ mm s}^{-1}$, $H_{\text{int}} = 286 \pm 4 \text{ kOe}$, $\Gamma = 0.35 \pm 0.01 \text{ mm s}^{-1}$. Once again using the previously reported results [11,12] this sextet is attributed to ^{57}Fe occupying the A-sites with (6Fe + 2Si or Ni or Al) nn at the D-sites and 6 nnn Fe at the A sites. Our observed value of $H_{\text{int}} = 286 \pm 4 \text{ kOe}$ is fairly close to the value $H_{\text{int}} = 282 \text{ kOe}$ reported earlier [12] and this slight difference can be explained as before.

The line-broadening as well as the deviation of the ratio of the areas under sextets II and III from the expected value 1:2 is explained as follows. The Super Sendust sample of the present composition is not stoichiometric. This non-stoichiometry in $\text{Fe}_3\text{Si}(\text{Al},\text{Ni})$ will lead to more Fe-atoms at the D site. It has been suggested [17] that there is a finite probability that the ^{57}Fe at the A-site will have the configuration $[\text{5Fe}+\text{3Si}(\text{Al},\text{Ni})]\text{nn}$ or $[\text{6Fe}+\text{2Si}(\text{Al},\text{Ni})]\text{nn}$ or $[\text{7Fe}+\text{1Si}(\text{Al},\text{Ni})]\text{nn}$ and $[\text{6Fe}]\text{nnn}$.

The configuration $[\text{5Fe}+\text{3Si}(\text{Al},\text{Ni})]\text{nn}$ and $[\text{6Fe}]\text{nnn}$ will cause the broadening of the sextet IV and it will also increase the area under this sextet (IV). However the configuration $[\text{6Fe} + \text{2Si}(\text{Al},\text{Ni})]\text{nn}$ and $[\text{6Fe}]\text{nnn}$ gives rise to sextet IV. The configuration $[\text{7Fe}+\text{1Si}(\text{Al},\text{Ni})]\text{nn}$ and 6Fe nnn forms the sextet II thus broadening it and increasing area under it. The presence of $[\text{7Fe}+\text{1Si}(\text{Al},\text{Ni})]\text{nn}$ will thus change the ratio of areas under the sextets II and III from the expected value 1:2. The ^{57}Fe at the D-sites

will have $[8\text{Fe}] \text{nn}$ and $[4 \text{ or } 2 \text{ or } 0 \text{ Si(Al,Ni)}] \text{nnn}$ and this will also cause the broadening of the sextet II.

The Mössbauer spectra as for the samples SD1, SD2 and SD3 recorded at 80 K are presented in Fig. 5.3 and they are all similar in their appearance. Each of these spectra can be analyzed into 4 sextets as in the case of spectra measured at 293 K. Mössbauer parameters obtained from such an analysis are given in Table 5.3 for the four sextets. In the case of the I sextet, the observed Mössbauer parameters are : $\text{IS} = +0.07 \pm 0.01 \text{ mm s}^{-1}$, $H_{\text{int}} = 337 \pm 4 \text{ kOe}$ and $\Gamma = 0.28 \pm 0.01 \text{ mm s}^{-1}$. Mössbauer spectrum of the α -Fe sample was measured by us at 80 K and this measurement yielded $\text{IS} = +0.08 \pm 0.01 \text{ mm s}^{-1}$, $H_{\text{int}} = 337 \pm 4 \text{ kOe}$ and $\Gamma = 0.28 \pm 0.01 \text{ mm s}^{-1}$. Comparison of these results confirms our earlier assignment that the I sextet is due to ^{57}Fe nuclei present in the iron-rich region. As far as the other three sextets are concerned, there are no other measurements reported at 80 K and we are unable to compare the results of Table 5.3 with any other data. We, however, feel that the assignments made on the basis of the Mössbauer parameters measured at 293 K (Table 5.1) are the most likely.

Mössbauer spectra of the sample SD1 recorded in the temperature range 380-926 K are shown in Figs. 5.3 and 5.4. It is observed that each of the Mössbauer spectrum recorded in the temperature range 380-800 K consists of

Table 5.3

Mossbauer parameters (measured at 80 K) for sample SD1, SD2 and SD3.

Sam- ple	Site	IS (a)	H _{int} (b)	Γ (c)	Area ratio (d)	Assignment (e)
SD1	I	0.07	337.6	0.28	1.0	(8 nn + 6 nnn) Fe
	II	0.11	317.3	0.48	1.9	8 nn Fe + 6 nnn Si or (Ni, Al)
	III	0.20	247.0	0.48	1.5	[4Fe and 4Si or (Ni,Al)] nn + 6 nnn Fe
	IV	0.10	292.0	0.34	0.80	[6Fe and 2Si (Ni,Al)] nn + 6 nnn Fe
SD2	I	0.08	338.0	0.28	1.0	Same as for SD1
	II	0.13	319.0	0.48	1.79	
	III	0.24	251.9	0.48	0.61	
	IV	0.11	293.7	0.34	1.29	
SD3	I	0.07	337.8	0.28	1.0	Same as for SD1
	II	0.11	319.0	0.48	1.97	
	III	0.22	249.5	0.48	1.64	
	IV	0.11	293.0	0.34	0.90	

(a) IS = Isomer shift, values in mm s^{-1} with respect to $\alpha\text{-Fe}$ ^{TS of room temperature}
Typical error is $\pm 0.01 \text{ mm s}^{-1}$.

(b) H_{int} = Internal magnetic field at ^{57}Fe nucleus: in units of kOe. Typical error is $\pm 4 \text{ kOe}$.

(c) (FWHM) = Width of the spectral line, values in mm s^{-1} .
Typical error is $\pm 0.01 \text{ mm s}^{-1}$.

(d) The area ratio value are given with respect to the area (1.0) under sextet I.

(e) nn = nearest neighbour, nnn = next nearest neighbour.

IS is corrected for second order Doppler shift.

a set of four sextets corresponding to four distinct sites of ^{57}Fe . These four sites observed at the higher temperatures appear to correspond to the same four sites observed at 80 and 293 K and have been discussed earlier. Our results further indicate that there is no change in the lattice ordering of the SD1 sample as the temperature is raised upto 800 K. The lines of the Mössbauer spectra recorded at 700 and 800 K show smaller line-broadening and this behaviour could be caused by the effect of conduction electron polarization. The temperature dependence of the hyperfine magnetic field, H_{int} , for the four sites (Table 5.4) is shown in Fig. 5.7 and it shows that the value of H_{int} decreases with temperature for all four sites. It is further observed that the decrease in H_{int} is smooth in the case of sites I and III but a small discontinuity at about 700 K is observed in the case of sites II and III. The reason for this behaviour at 700 K is not clearly understood.

It is further noted that in the temperature range 80-800 K no quadrupole splitting is observed in any of the four sextets. This behaviour is understood in the light of observation made by Lesoille and Gielen [18] who have reported that the DO_3 type structure does not show any quadrupole splitting because of the special relationship between the direction of effective magnetic

Table 5.4

Mossbauer parameters (measured in the temperature range 380-926 K) for sample SD1.

Temperature T(K)	Site	I.S. (a)	H _{int} (b)	Γ (c)	Area ratio (d)	Assignment (e)
380	I	-0.05	319.0	0.28	1.0	(8 nn + 6 nnn) Fe
	II	0.01	301.7	0.48	2.40	8 nn Fe + 6 nnn Si or (Ni, Al)
	III	0.12	231.0	0.48	1.90	[4Fe and 4Si or (Ni,Al)] nn + 6 nnn Fe
	IV	0.01	277.1	0.35	1.23	[6Fe and 2Si or (Ni,Al)] nn + 6 nnn Fe
486	I	-0.12	302.6	0.28	1.0	Same as for 380 K.
	II	-0.07	284.0	0.48	2.11	
	III	+0.05	217.7	0.48	1.94	
	IV	-0.08	262.9	0.35	1.12	
600	I	-0.15	280.2	0.28	1.0	Same as for 380 K
	II	-0.12	259.2	0.48	2.90	
	III	-0.01	198.5	0.48	2.60	
	IV	-0.12	240.3	0.34	1.40	
700	I	-0.20	249.1	0.28	1.0	Same as for 380 K.
	II	-0.18	222.4	0.32	1.44	
	III	-0.07	167.8	0.38	1.20	
	IV	-0.14	196.8	0.30	0.78	
800	I	-0.41	223.0	0.28	1.0	Same as for 380 K
	II	-0.33	197.7	0.34	1.65	
	III	-0.32	142.2	0.39	1.55	
	IV	-0.33	174.4	0.32	1.20	
926 \pm 1K		-0.30	-	0.92	-	Single paramagnetic line

(a) IS = Isomer shift, values in mm s⁻¹ with respect to α -Fe:
Typical error is ± 0.01 mm s⁻¹. IS of room temperature

(b) H_{int} = Internal magnetic field at ⁵⁷Fe nucleus : in units
of kOe. Typical error is ± 5 kOe.

(c) Γ (FWHM) = Width of the spectral line, values in mm s⁻¹;
Typical error is ± 0.01 mm s⁻¹.

(d) and (e) as in Table 5.3.

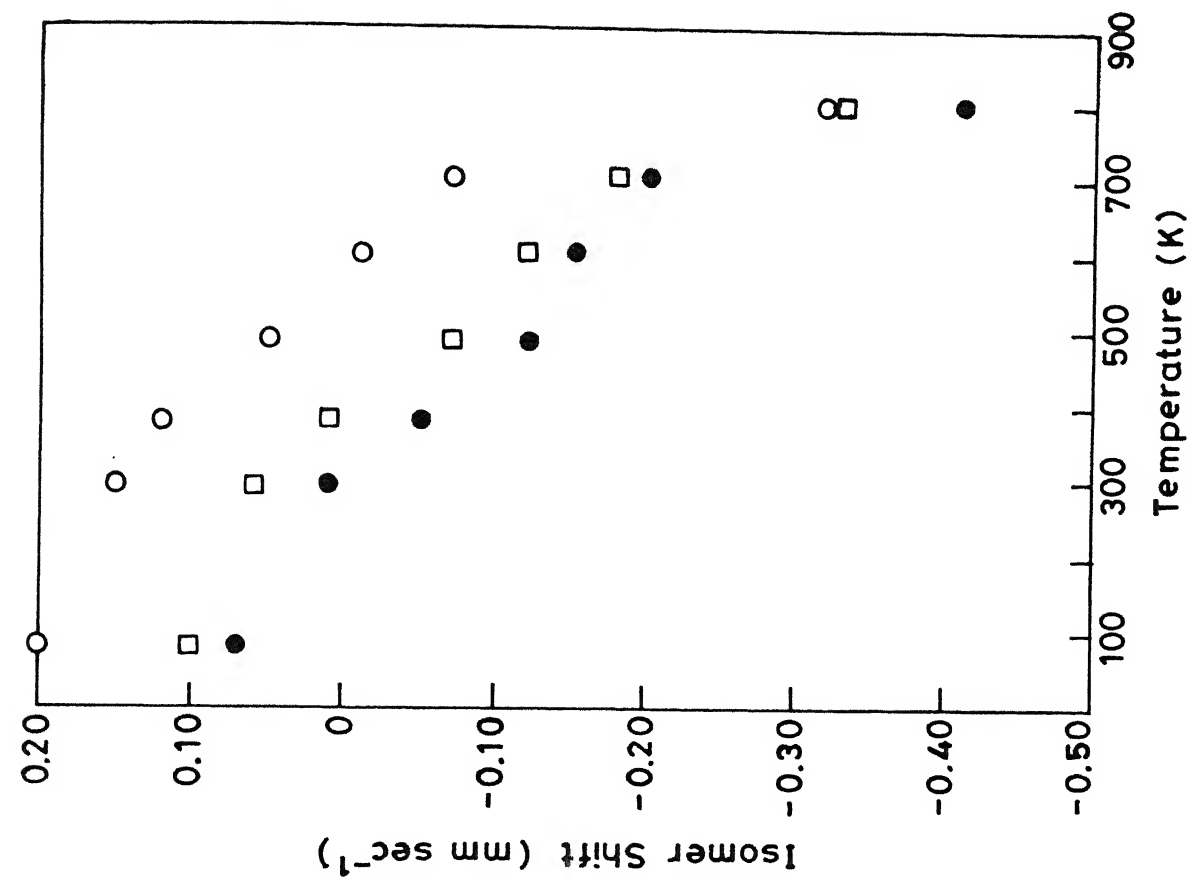


Fig. 5.8 The IS as a function of temperature for sites I, II and III.

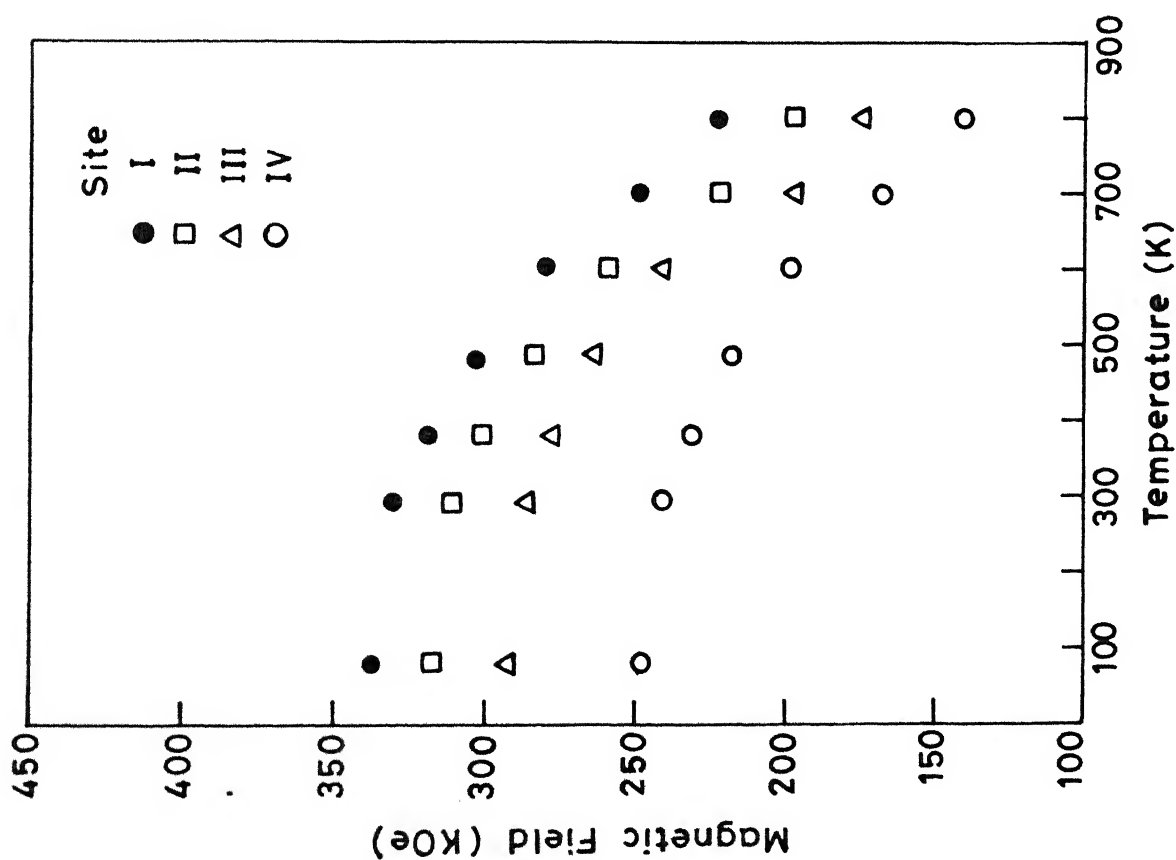


Fig. 5.7 Magnetic field (Hint) at ^{57}Fe as a function of temperature for sites I, II, III and IV.

look at Fig. 5.8 shows that the value of IS for each site decreases much faster between 700 and 800 K than the previous rate between the range 300-700 K. This behaviour appears preliminary to the changes in the conduction electrons and electronic structure occurring at 926 K.

Based on the least-squares-fitting (using the computer program) we had proposed above the existence of four distinct sites in the Super Sendust sample. To confirm this point, we determined the magnetic field distribution, $P(H)$, using Window's method discussed in Chapter 2. These distributions for the sample SD1 in the temperature range 80-900 K are shown in Fig. 5.9. It is seen that each of these distribution curves consist of four peaks which confirm the existence of four sites. The distribution corresponding to 900 K shows three peaks but we feel that one of them is a composite peak. The average value of the magnetic field, \bar{H} , corresponding to each site was calculated using the expression

$$\bar{H} = \frac{1}{N} \sum_{i=1}^N P_i(H_i) H_i \quad (5.1)$$

where N denotes the number of points used in the range $H_{\min} \leq H_i \leq H_{\max}$. The value of H_{\min} and H_{\max} for each site was determined with the help of Mössbauer parameters obtained by least-squares-curve fitting. In our computations N ranged from 20 to 25.

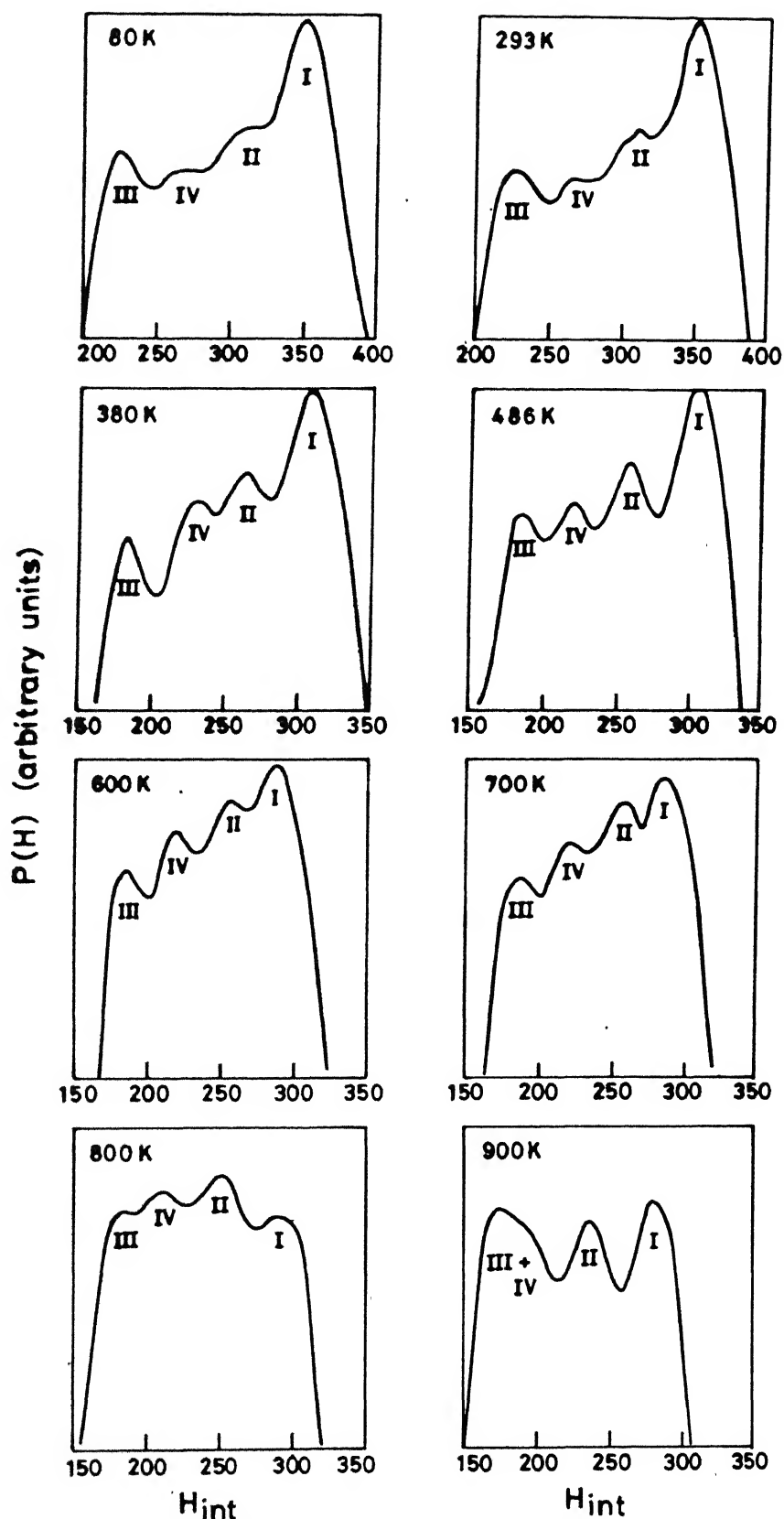


Fig.5.9 Hyperfine field (H_{int}) distribution for SD 1 in the temperature range 80 - 900 K.

Table 5.5 : Various parameters related to the P(H) distribution obtained for SD1 in the temperature range 80-900 K.

Temperature K	Site	Average value of H_{int} \bar{H} in kOe	$H_{min} - H_{max}$ in kOe	χ^2
80	I	335.0	300 - 400	4.16
	II	270.0		
	III	145.0		
	IV	218.0		
293	I	326.0	Same as 80 K	5.12
	II	259.0		
	III	132.0		
	IV	202.0		
380	I	316.0	250 - 350	6.71
	II	241.0		
	III	126.0		
	IV	192.0		
486	I	301.0	Same as 380 K	5.17
	II	231.0		
	III	126.0		
	IV	168.0		
600	I	274.0	Same as 380 K	4.82
	II	232.0		
	III	120.0		
	IV	168.0		
700	I	268.0	Same as 380 K	3.42
	II	221.0		
	III	113.0		
	IV	167.0		
800	I	283.0	250 - 325	7.18
	II	216.0		
	III	107.0		
	IV	159.0		
900	I	183.0	225 - 325	6.58
	II	116.0		
	III+IV	83.0		

The shape of the magnetic field distribution curve, $P(H)$, corresponding to spectra measured at 80 and 293 K appear similar (Fig. 5.9) with peak corresponding to $\bar{H} \approx 326$ kOe showing maximum probability. This peak is attributed to the site I while the assignments of other peak to the remaining sites is indicated in the figure. As the temperature is raised, the relative intensities of different peaks change, with the peaks having lower \bar{H} occurring with greater probability than before. At 800 K the relative probability is maximum for the peak corresponding to site II (characterized by $\bar{H} = 216$ kOe). The change in the shape of $P(H)$ as a function of temperature is attributed to the changes in the strength of the magnetic interaction which, in turn, is caused by the fast spin fluctuations occurring at higher temperatures. The value of the average magnetic field \bar{H} , the limits H_{\min} and H_{\max} for each site in the temperature range 80-900 K are listed in Table 5.5. At 900 K, the Mössbauer spectrum collapses into fewer spectral lines and the $P(H)$ curve shows three peaks. Out of these three peaks, the peak corresponding to $\bar{H} = 83$ kOe appears broader and we have considered it to be a composite peak due to site III and IV.

5.4 SUMMARY AND CONCLUSIONS

Super Sendust alloy having a composition 2.96 wt% Ni,

5.0 wt % Si, 3.87 wt % Al and 88.17 wt % Fe was investigated by X-ray diffraction and Mössbauer spectroscopy. The X-ray diffraction spectrum reveals that the quaternary alloy has DO_3 type structure with a lattice constant of 5.6740 Å. Mössbauer spectroscopic studies carried out over the temperature range 80–296 K shows four clear sextets in the range 80–800 K. These four sextets arise out of ^{57}Fe at four different sites and the possible assignment of these four sites is suggested. Further the Mössbauer spectra measured in the range 80–800 K suggest that the Super Sendust alloy maintains DO_3 -type structure from 80 K to 800 K. Beyond 800 K the Mössbauer spectrum changes and shows a paramagnetic line at 926 K, thus indicating that the magnetic ordering temperature $T_c = 926$ K. Line broadening of the sextets in the temperature range 80–800 K can be understood in terms of possible configuration of atoms. The work reported by us on the Super Sendust alloy is by no means conclusive. However it has indicated the interesting properties of this high permeability material. We feel that further studies of this material (e.g. Mössbauer spectroscopic studies for other composition, neutron diffraction NMR and other studies etc.) should be carried out to understand the electronic properties of Super Sendust alloy system.

REFERENCES

1. O. Heaviside, ''Notes on the theory of the telephone and on hysteresis'', Electrician 1907, pp23.
2. B. Speed and G.W. Elmen, Trans. AIEE, 40, 596 (1921).
3. W.J. Shackleton and I.G. Barber, Trans. A.I.E.E., 47, 429 (1928).
4. D.F.W. Champion and E.G. Wilkins, Wireless World 1953, pp147.
5. H.D. Arnold and G.W. Elmen, J. Franklin Inst. 195, 621 (1923).
6. H. Masumoto and T. Yamamoto, Journal of the Japan Inst. of Metals 1, 127 (1937).
7. T. Yamamoto and Y. Ulsushikawa, Trans. of the Japan Inst. of Metals, 19, 326 (1978).
8. G.C. Uniyal, M.Tech. Thesis, Indian Institute of Technology, Kanpur, India (Unpublished) 1986;
G.C. Uniyal and K.N. Rai (Private Communication).
9. O. Schneeweiss, T. Zemcik, T. Zak and S. Mager, Phys. Stat. Sol. (a) 79, 125 (1983).
10. M. Miura, K. Tanaka and Y. Noro, Jap. J. Appl. Phys. 25, 1192 (1986).
11. M.B. Stearns, Phys. Rev. 129, 1136 (1963).
12. G.A. Perez Alcazar and E. Galvao da Silva, J. Phys. F (Met. Phys.) 17, 2323 (1987).
13. K. Ono, Y. Ishikawa and A. Ito, J. Phys. Soc. Japan 17, 1747 (1962).

14. J. Pickart and R. Nathans, Phys. Rev. 123, 1163 (1961).
15. A. Paolette and L. Passari, Nuovo Cimento 32, 25 (1964).
16. M.B. Stearns, Phys. Rev., 168, 588 (1968).
17. M.B. Stearns, Phys. Rev. B 4, 4069 (1971).
18. M.R. Lesoille and P.M. Fielen, Phys. Stat. Sol. 37, 127 (1970).
19. M.B. Stearns, J. Appl. Phys. 35, 1095 (1964).

106279

PHY - 1988-70 JOHN - MDC